TAMPERE UNIVERSITY OF TECHNOLOGY

KAROLIINA KOSKI

MODELLING OF THE HUMAN ARM FOR WEARABLE PASSIVE UHF RFID TAG APPLICATIONS

Master of Science Thesis

Examiners: Adjunct Professor Leena Ukkonen
and Professor Lauri Sydänheimo
Examiners and topic approved by the Faculty
Council of the Faculty of Computing and
Electrical Engineering on 6 June 2012.

ABSTRACT

TAMPERE UNIVERSITY OF TECHNOLOGY
Master's Degree Programme in Electrical Engineering
KOSKI, KAROLIINA: Modelling of the human arm for wearable passive UHF RFID tag applications
Master of Science Thesis, 81 pages
November 2012
Major: RF Engineering
Examiners: Adjunct Professor Leena Ukkonen and Professor Lauri Sydänheimo
Keywords: Embroidered antenna, human body, UHF RFID, wearable antenna

Radio frequency identification (RFID) technology is rapidly emerging within bio-medical engineering applications. Particularly in harsh and challenging environments, RFID provide fast and reliable item identification and tracking solution. In a typical RFID system objects to be identified are marked with tags, consisting of an antenna and an integrated circuit. The tags are wirelessly read by a stationary reader unit. In the future, wearable RFID tags integrated into daily clothing could provide multi-functional garments for real-time remote bio-monitoring of humans without any human involvement. At ultra-high frequencies (UHF) the human body is electrically a challenging application environment for the tag due to its high permittivity and high losses. Modelling of the human body for UHF is not a straightforward task. The body in close proximity tends to interact with the tag in a disadvantageous manner, resulting in severe overall tag performance degradation. However, an accurate human model is of paramount importance for future design and optimisation of wearable antennas.

In this project, a novel wireless approach is used to develop a UHF human arm model for wearable antenna applications. A reference tag is designed and its response is practically measured when the tag is directly attached to the human arm. The response serves as a reference response. A simple homogenous cylinder is used in electromagnetic simulations to represent the human arm. The cylinder material is defined with the electrical parameter variables effective relative permittivity, $\varepsilon_{r,eff}$, and loss tangent, tan δ. The reference tag is simulated on the cylinder. By adjusting the variables $\varepsilon_{r,eff}$ and tan δ properly, agreement is found between the reference response and the simulated tag response on the cylinder. The approach eliminates the need for any information about the electrical parameters of a particular tissue type. Further, the wireless approach removes the need for baluns or fixture required in wired tag antenna input impedance measurements.

It is verified that the developed UHF human arm model is able to predict the wearable tag performance on the human arm with ±3 dB accuracy over the frequency band 800–1000 MHz. The simple human arm simulation model can hereby be used as a powerful tool for future wearable antenna design and optimisation.

TIIVISTELMÄ

TAMPEREEN TEKNILLINEN YLIOPISTO
Sähkötekniikan koulutusohjelma
KOSKI, KAROLIINA: Ihmiskäsivarren mallintaminen puettaville passiivisille UHF RFID tunniste -sovelluksille
Diplomityö, 81 sivua
Marraskuu 2012
Pääaine: Suurtaajuustekniikka
Tarkastajat: Apulaisprofessori Leena Ukkonen ja professori Lauri Sydänheimo
Avainsanat: Ihmiskeho, ommeltu antenni, UHF RFID, puettava antenni

Radiotaajuinen tunnistustekniikka (engl. Radio Frequency Identification, RFID) löytää yhä enemmän ja enemmän sovelluskohteita lääketieteellisessä tekniikassa. Erityisesti vaikeissa sekä haastavissa ympäristöissä RFID mahdollistaa kohteen nopean ja luotettavan tunnistus- sekä seuranata-ratkaisun. Tyypillisessä RFID järjestelmässä tunnistettavat kohteet merkitään tunnisteilla, jotka koostuvat tunnisteantennista sekä mikropiiristä. Tunnisteita luetaan langattomasti stationaarisella lukijalaitteella. Tulevaisuudessa, vaatteisiin integroidut puettavat RFID tunnisteet mahdollistavat monitoimi-vaatekappaleita ihmisten langatonta ja reaaliaikaista biomonitorointia varten. UHF taajuuksilla (0.3–3 GHz) ihmiskehon korkea permittiivisyys sekä korkeat häviöt muodostavat sähköisesti haastavan sovelluskohteen tunnisteelle. Ihmiskehon mallintaminen UHF taajuuksille ei ole suoraviivainen tehtävä. Ihmiskeho vaikuttaa tämän lähistössä olevaan tunnisteeseen epäedullisesti, johtaen tunnisteen suorituskyvyn vakavaan heikkenemiseen. Tulevaisuudessa, ihmiskehon mallintaminen on kuitenkin erittäin tärkeä osa puettavien antennien suunnittelussa ja optimoinnissa.

Tässä työssä esitetään uudenlainen langaton lähestymistapa ihmiskäsivarren mallintamiseen puettaville UHF sovelluksille. Tarkoituksena on mitata referenssitunnisteen vaste tunnisteen ollessa kiinni käsivarressa ja hyödyntää mitattua referenssivastetta mallin rakentamiseen. Käsivarsi mallinnetaan kenttäsimulaattorissa yksinkertaisella homogeenisella lieriöllä. Lieriölle annetaan sähköiset parametrimuuttujat suhteellinen permittiivisyys, $\varepsilon_{r,eff}$, sekä häviökerroin, tan δ, kuvamaan lieriön materiaalisisältöä. Asettamalla sähköisten parametrimuuttujien arvot oikein, referenssitunnisteen simuloitu vaste saadaan yhteensopivaksi mitatun referenssivasteen kanssa. Käytetty lähestymistapa ei vaadi tietämystä yksittäisten kudoksien sähköisistä ominaisuuksista tai kudoksien suuruuksista. Lisäksi esitetyssä langattomassa menetelmässä ei tarvita baluunia tai erillistä kiinnityskappaletta, toisin kuin tunnisteantennin sisäänmenoimpedanssin mittauksissa.

Työssä vahvistetaan, että suunniteltu ihmiskäsivarren malli UHF taajuuksille kykenee ennustamaan puettavan tunnisteen suorituskyvyn ihmiskäsivarressa ±3 dB:n tarkkuudella taajuuskaistalla 800–1000 MHz. Suunniteltua yksinkertaista ihmiskäsivarren simulointimallia voidaan näin ollen jatkossa hyödyntää tehokkaana työkaluna puettavien antennien suunnittelussa sekä optimoinnissa.

PREFACE

This Master of Science Thesis is conducted at the Tampere University of Technology (TUT) in the Department of Electronics in 2012. Research work of this Master of Science Thesis has been funded by Finnish Funding Agency for Technology and Innovation (TEKES, KÄKI-project) and Centennial Foundation of Finnish Technology Industries. All measurements and development are carried out in the Wireless Identification and Sensing Systems (WISE) Research Group of Rauma Research Unit. The objective of this Master of Science Thesis is to develop a model of the human arm in the High Frequency Structure Simulator (HFSS) software for the microwave region. This model is an important and essential step for the development of wearable radio frequency identification (RFID) tags.

The examiners of this Master of Science Thesis are Adjunct Professor Leena Ukkonen and Professor Lauri Sydänheimo. I would like to thank the examiners for guidance throughout the whole thesis process, flexibility and encouragement. Moreover, I would like thank the examiners for my research assistant position and for an interesting and instructive project. I am also grateful to my instructor Toni Björninen for his great assistance.

In addition, I would like to give my compliments to the research group researchers Eveliina Koski, Elham Moradi, A. Ali Babar, and Juha Virtanen and for their support and advice. Last but not least, I would like to thank my partner Tuomas Messo for his incessant support, encouragement and patience.

Tampere, 3 October 2012

_____

Karoliina Koski

CONTENTS

ABBREVIATIONS

AIDC	Automatic Identification and Data Capture
AR	Axial Ratio
ASIC	Application Specific Circuit
ASK	Amplitude-Shift Keying
BAN	Body Area Network
CEPT	European Conference of Postal and Telecommunications
DSB-ASK	Double-Sideband Amplitude Shift Keying
EBG	Electromagnetic Band-Gap
EIRP	Equivalent Isotropic Radiated Power
EPC	Electronic Product Code
ERP	Equivalent Radiated Power
ETSI	European Telecommunications Standards Institute
FCC	Federal Communications Commission
HF	High-Frequency
HPBW	Half-power beamwidth
ITU	The International Telecommunication Union
LF	Low-Frequency
MPT	Ministry of Posts and Telecommunications
OCR	Optical Character Recognition
PAN	Personal Area Network
PIE	Pulse Interval Encoding
PR-ASK	Phase-Reverse Amplitude Shift Keying
PSK	Phase Shift Modulation
RCS	Radar Cross Section
RFID	Radio Frequency Identification
TEM	Transverse Electromagnetic Wave
UHF	Ultra-High Frequency

SYMBOLS

A_e	Effective aperture [m^2]
λ	Wavelength [m]
α	Attenuation constant [Np/m]
β	Phase constant [rad/m]
c	Speed of light [m/s]
D	Directivity [dBi]
e	Radiation efficiency
ε	Permittivity [F/m]
f	Frequency [1/s]
G	Antenna gain [dBi]
Γ	Voltage reflection coefficient
δ_s	Skin depth [m]
γ	Complex propagation constant [1/m]
k	Wave number [rad/m]
η	Wave impedance [Ω]
Ω_A	Beam solid angle [sr]
P	Power [W]
R	Resistance [Ω]
S	Power flux density [W/m^2]
σ	Conductivity [S/m]
σ	Radar cross section [m^2]
τ	Power transfer coefficient
U	Radiation intensity [W/sr]
v	Velocity [m/s]
ω	Angular frequency [rad/s]
X	Reactance [Ω]
μ	Permeability [H/m]
Z	Impedance [Ω]

1 INTRODUCTION

Automatic Identification and Data Capture (AIDC) refers to the group of various technologies employed to automatically identify items, collecting data about them and the ability to enter that data electronically into computer systems. Typically, these systems operate without any human involvement. Examples of AIDC include barcodes, Radio Frequency Identification (RFID), biometrics, Optical Character Recognition (OCR), smart cards and voice recognition. Much of the item data can be carried electronically and attached to the item itself as barcodes or RFID tags. These tagged items can then be tracked everywhere and every time. Such benefits are maximised when large volumes of items, for example in a manufactory line, need to be identified in a short time. Moreover, financial benefits are also gained through reduced errors and handling time.

Particularly RFID systems are gaining increased popularity due to their low cost, reliability, long identifying ranges, and operation without the human involvement. RFID finds applications in inventory control, container tracking, access control, ID badges, equipment and personnel tracking in hospitals, parking lot control and product tracking through manufacturing and assembly. More recently, much attention has been paid to real-time bio-monitoring and medical monitoring applications. In the future, wearable RFID tags integrated into daily garments could work as a body-centric RFID system providing real-time bio-monitoring. It could for example remotely monitor people's location. When the tag also comprises various kinds of sensors, monitoring of human body movement, temperature, blood pressure et cetera becomes possible.

Usually, the human body itself forms the tag application environment. In electromagnetic point of view, the human body constitutes a challenging environment for RFID tag design. The tag plays a key role in the quality of the overall RFID system performance. Tag modelling and simulations in its intended application environment are necessary and critical steps in design and optimisation processes to predict the tag performance. This requires accurate electromagnetic modelling of the environment. Several approaches have been used to model the human body for wearable RFID tag applications. Mostly, these approaches include the use of available tissue databases and the human body model verification is done either using phantoms filled with tissue-equivalent liquids or practical measurements with volunteer subjects. In this project, the aim is to develop a novel human arm model for passive ultra-high frequency (UHF) wearable tag applications. The electrical properties of single tissue layers within the human arm are not determined, but rather the electrical properties of the effective human arm including the summarised effect of all involved tissues. This is done by

comparing measured response of a test tag on a volunteer subject to simulation results of the tag on a cylindrical arm model with adjustable effective electrical parameters. By adjusting these parameters, agreement between the measured and simulated responses is found.

This Master of Science Thesis is structures as follows. Chapter 2 provides in-depth description of required theoretical background including electromagnetism and electromagnetic wave propagation, basic antenna theory, and a detailed description of the passive UHF RFID system operating principle. In Chapter 3 attention is paid to earlier research and publications within this Master of Science Thesis topic. The actual topic is processed is Chapters 4 and 5. The research method, measurements and simulations, together with the proposed human arm model, are explained in Chapter 4. The model verification is conducted in Chapter 5. Finally, conclusions are drawn in Chapter 6.

2 BACKGROUND THEORY

This Section provides necessary background theory for this project. The Section serves to present a literature review needed to build the theoretical framework for the conducted project and to introduce essential concept definitions.

2.1 Electromagnetism

According to [1], the term microwaves refers to alternating current wave with frequencies f between 300 MHz and 300 GHz, corresponding to wavelengths $\lambda = c/f$ between 1 m and 1 mm, respectively, where c is the speed of light. More specifically, microwaves identify a methodology, that is, certain electromagnetic phenomena studies approach [2]. This approach is described by Maxwell's equations and is the intermediate methodology between the other two derived from Maxwell's equations; circuit theory and optics. To be precise, it is not the frequency range that determines the proper methodology, but rather the ratio between the wavelength and the dimensions of the circuits or objects where the electromagnetic field manifests itself [2]. At low frequencies, for which the wavelength is much larger than the dimensions of the circuits and the phase variation across the dimensions of a circuit element is insignificant, standard circuit theory can be applied which represents a simplification of Maxwell's equations. In the opposite case, in which the wavelength is much shorter than the dimensions of the circuit elements, Maxwell's equations can be simplified to the geometrical optics regime, and optical laws can be applied in optical systems design. At microwave frequencies, the wavelengths are of the same order as the circuit dimensions. Therefore, neither approximation is permissible and as a result, Maxwell's equations have to be solved in their entirety. [1] Nowadays wireless data transfer and all antenna and wave guide applications rest heavily on Maxwell's model for electromagnetic interaction.

2.1.1 Maxwell's equations

Maxwell's equations in differential, integral and phasor form are collected in Table 2.1, followed by the electromagnetic quantities and their units. The differential form of Maxwell's equations describes the electric and magnetic fields as a real function of spatial coordinates (x,y,z) and the time coordinate t. The integral form represents how the field integrals over a closed surface S or along a closed contour ∂S around the surface are dependent of the sources or the time-varying fields. Both the differential and integral form is valid for arbitrary time dependence. However, the majority of

electromagnetic applications involve fields having a sinusoidal (harmonic) time dependence of angular frequency $\omega = 2\pi f$. The time-harmonic real electric field can be given as:

$$\overline{E}(x, y, z, t) = \mathrm{Re}\left[\boldsymbol{E}(x, y, z)e^{j\omega t}\right] \tag{2.1}$$

Hence, at a certain point (x,y,z), the field can be thought to be a rotating vector in the complex plane having a constant amplitude. The real physical fields are attained as the real part of the complex vector fields. Assuming a $e^{j\omega t}$ time dependence, the time derivatives in the differential form can be replaced by $j\omega$ to get the phasor form. [1]

Table 2.1. Maxwell's equations, their quantities and units.

Differential form	Integral form	Phasor form	Designation
$\nabla\times\overline{E}=-\frac{\partial\overline{B}}{\partial t}$	$\int_{\partial S}\overline{E}\cdot d\bar{l}=-\frac{\partial}{\partial t}\int_{S}\overline{B}\cdot d\bar{s}\;\forall S$	$\nabla\times\boldsymbol{E}=-j\omega\boldsymbol{B}$	Faraday's law
$\nabla\times\overline{H}=\overline{J}+\frac{\partial\overline{D}}{\partial t}$	$\int_{\partial S}\overline{H}\cdot d\bar{l}=\int_{S}\overline{J}\cdot d\bar{s}+\frac{\partial}{\partial t}\int_{S}\overline{D}\cdot d\bar{s}\;\forall S$	$\nabla\times\boldsymbol{H}=\boldsymbol{J}+j\omega\boldsymbol{D}$	Ampère-Maxwell's law
$\nabla\cdot\overline{D}=\rho$	$\int_{\partial V}\overline{D}\cdot d\bar{s}=\int_{V}\rho\,dv=Q\;\forall V$	$\nabla\cdot\boldsymbol{D}=\rho$	Gauss' law for electricity
$\nabla\cdot\overline{B}=0$	$\int_{\partial V}\overline{B}\cdot d\bar{s}=0\;\forall V$	$\nabla\cdot\boldsymbol{B}=0$	Gauss' law for magnetism

Quantity	Symbol	Unit
Electric field intensity	$\overline{E}$	V/m
Magnetic field intensity	$\overline{H}$	A/m
Electric flux density	$\overline{D}$	Coul/m^2
Magnetic flux density	$\overline{B}$	Wb/m^2
Electric current density	$\overline{J}$	A/m^2
Electric charge density	ρ	Coul/m^3
Permittivity	ε	F/m
Relative permittivity	$\varepsilon_r=\varepsilon/\varepsilon_0$	–
Permeability	μ	H/m
Relative permeability	$\mu_r=\mu/\mu_0$	–
Conductivity	σ	S/m

In free-space, the electric and magnetic field intensities and flux densities are related through the following relations [1]:

$$\begin{aligned}\overline{B}&=\mu_0\overline{H},\\ \overline{D}&=\varepsilon_0\overline{E},\\ \overline{J}&=0,\end{aligned} \tag{2.2}$$

where $\mu_0 = 4\pi \cdot 10^{-7}$ H/m is the permeability of free-space and $\varepsilon_0 = 8.854 \cdot 10^{-12}$ F/m is the permittivity of free-space.

Faraday's law verifies that a time varying magnetic flux through an arbitrary surface *S* causes an electromotive force at the surface peripheral. Ampère-Maxwell's law states that the magnetic field contour integral over an arbitrary surface *S* gives the total current through that surface.

The surface integral in Gauss' law for magnetism gives the total magnetic flux through a volume *V*. Since ∂S is defined to have the same direction as the outer surface normal, all magnetic flux going outward from the volume is positive and all magnetic flux going inwards the volume is negative. Hence, Gauss' law for magnetism states that the outward and inward going magnetic fluxes are equal for an arbitrary volume. From this results that the magnetic field doesn't have sources or drains, that is, the field lines form closed loops that do not have a beginning or end. Gauss law for electricity states that the electric field may have sources and drains. The sources and drains are the free charges inside the volume *V*. The surface integral gives the total net charge inside an arbitrary volume *V*.

The continuity equation can be derived directly from Ampère-Maxwell's law, giving in differential and integral form [1]:

$$\nabla \cdot \bar{J} = -\frac{\partial \rho}{\partial t} \qquad \text{and} \qquad \int_{\partial V} \bar{J} \cdot d\bar{s} = -\int_{V} \frac{\partial \rho}{\partial t} dv. \tag{2.3}$$

The equation states that charge is conserved. The integral form tells that the outflow of current density through a volume *V* causes a negative charge build-up with time inside that volume. The displacement current $\partial \bar{D} / \partial t$ is necessary in Ampère-Maxwell's law to ensure the charge conservation law in a time-varying case.

2.1.2 Constitutive relations and boundary conditions

In the previous section, electric and magnetic fields are assumed to be in free-space. In practise, material media are always present. When electromagnetic fields manifest themselves in material media, the field vectors are related to each other by the constitutive relations.

In an electromagnetic field, the total electromagnetic force on a charge *q* is given by the Lorentz's force equation [3]:

$$\bar{F} = q(\bar{E} + \bar{u} \times \bar{B}), \tag{2.4}$$

where $\bar{u}$ is the charge velocity vector. In materials having free charges ($\sigma \neq 0$), part of the power carried by the electromagnetic field is used to accelerate the charges, causing currents in the material. The Maxwell's equations, together with the Lorentz's force

equation, can be used to explain and predict all macroscopic electromagnetic phenomena [3].

Lossless dielectrics are insulators that ideally do not contain any free charges. Instead, the charges in atoms are bound negative and positive charges that macroscopically form neutral atoms. However, an external electric field forces the bound charges to slightly move from their equilibrium positions, causing electric dipoles or dielectric polarisation. The electric dipoles interact with the external field, providing the material the ability to store electric energy. Energy is stored in the electric dipoles by the restraining forces on the electric dipoles when they are subjected to external applied electric field. The relative permittivity ε_r is a measure of the relative charge or energy storage capability of a dielectric material. In practise, dielectric materials are always lossy, containing free charge carriers that cause ohmic losses. The lossy dielectrics have a finite conductivity, which is allowed for in their complex permittivity as [1]:

$$\varepsilon = \varepsilon^{'} - j\varepsilon^{''}, \tag{2.5}$$

where the imaginary part represents the heat loss in the material and the real part determines the actual permittivity $\varepsilon^{'} = \varepsilon_r^{'}\varepsilon_0$. The heat losses are mainly caused by the electrical dipoles, which cannot vary with the same frequency as that of the applied electric field, leading to frictional damping that causes power loss. If the material has an appreciable amount of free charge carriers, the imaginary part will also include ohmic losses. Microwave materials are usually characterised by the real permittivity and the frequency dependent loss tangent. The loss tangent is defined as the ratio of the imaginary to the real part of the complex permittivity and is a measure of the power loss in the material [4]:

$$\tan\delta = \frac{\varepsilon^{''}}{\varepsilon^{'}}. \tag{2.6}$$

The larger the value of the loss tangent, the more the material converts energy from electric field into heat. The loss tangent does not separate the dielectric polarisation losses from the conduction losses, but discloses only the total power loss in the material.

Permeability is a measure of the ability of a material to magnetise in response to a magnetic field. The effect of a magnetic field on a material can be regarded analogous to that of the effects of an electric field: an applied magnetic field may align magnetic dipole moments in a magnetic material to produce magnetic polarisation or magnetisation. The permeability is also complex [1]:

$$\mu = \mu^{'} - j\mu^{''}, \tag{2.7}$$

where $\mu' = \mu_r' \mu_0$ is the actual permeability and again, the imaginary part accounts for frictional damping. Most materials are not affected by the magnetic field and their permeability is close to that of free-space zero.

In isotropic and linear (ε and μ not dependent on the strength of electric and magnetic fields) the constitutive relations can finally be written as [1]:

$$\begin{aligned} \boldsymbol{D} &= \varepsilon \boldsymbol{E}, \\ \boldsymbol{B} &= \mu \boldsymbol{H}, \\ \boldsymbol{J} &= \sigma \boldsymbol{E}. \end{aligned} \tag{2.8}$$

In practise electromagnetic problems involve contiguous regions of materials with different electrical properties (constitutive parameters). Therefore, it is necessary to know the boundary conditions that the field vectors ***E***, ***D***, ***B*** and ***H*** must satisfy at the interfaces. The integral form of Maxwell's equations hold for regions containing discontinuous material and are applied to a small region at an interface of two materials to derive the boundary conditions. [3] The following boundary conditions hold at an arbitrary interface of material and/or surface currents.

In general, the tangential component of the electric field is continuous across an interface:

$$\boldsymbol{n} \times (\boldsymbol{E}_2 - \boldsymbol{E}_1) = \boldsymbol{0}, \tag{2.9}$$

where the direction of the normal vector ***n*** is from medium 1 to medium 2. However, the possible electric surface current density $\boldsymbol{J}_s$ (A/m) at the interface causes discontinuity in the tangential component of a magnetic field across the interface:

$$\boldsymbol{n} \times (\boldsymbol{H}_2 - \boldsymbol{H}_1) = \boldsymbol{J}_s. \tag{2.10}$$

Similarly, the normal component of electric flux density field is discontinuous across an interface where a surface charge ρ_s exists:

$$\boldsymbol{n} \cdot (\boldsymbol{D}_2 - \boldsymbol{D}_1) = \rho_s. \tag{2.11}$$

The normal component of magnetic flux density field is continuous across an interface:

$$\boldsymbol{n} \cdot (\boldsymbol{B}_2 - \boldsymbol{B}_1) = 0. \tag{2.12}$$

Maxwell's equations are a set of partial differential equations describing the electromagnetic phenomena. The boundary conditions are required to guarantee that the solutions to these equations are single-valued.

The wave equation

From wireless data transfer perspective, the most important outgrowth of Maxwell's equations is that energy can be transferred as electromagnetic radiation without galvanic connection. This prediction is found in the wave equations, which are directly derived from Maxwell's equations and state that electromagnetic radiation may exist in the environment in wave form. These electromagnetic waves can propagate independently of their sources. Typically, wave propagation problems concern electromagnetic waves in a source-free region where ρ and $\boldsymbol{J}$ are both zero. In a simple (source-free, linear, isotropic and homogeneous) medium, the wave equations become [3]:

$$\begin{aligned} \nabla^2 \boldsymbol{E} - \mu\varepsilon \frac{\partial^2 \boldsymbol{E}}{\partial t^2} = 0, \\ \nabla^2 \boldsymbol{H} - \mu\varepsilon \frac{\partial^2 \boldsymbol{H}}{\partial t^2} = 0. \end{aligned} \tag{2.13}$$

These are the ideal wave equations since they describe the undisturbed electric and magnetic field propagations. All propagating waves in simple medium fulfil Eq. (2.13). For the time-harmonic case, the wave equations are derived from the phasor form of Maxwell's equations. In a source-free and simple medium, the wave equations become [1]:

$$\begin{aligned} \nabla^2 \boldsymbol{E} + k^2 \boldsymbol{E} = 0, \\ \nabla^2 \boldsymbol{H} + k^2 \boldsymbol{H} = 0, \end{aligned} \tag{2.14}$$

where $k = \omega\sqrt{\mu\varepsilon}$ is the propagation constant or wave number in the medium. These equations are called the homogeneous vector Helmholtz equations.

2.1.3 Wave propagation

Plane electromagnetic waves

The solution of the wave equation provides information about how the electromagnetic wave propagates in the medium. The wave equation may have several different solutions depending on the wave propagation form. Here, the solution for a uniform plane wave is considered. A uniform plane wave propagates along some fixed direction (say *z*-direction) and its electric and magnetic fields have no dependence on the transverse coordinates *x* and *y*, but are only functions of *z* and time *t*. With other words, the plane wave has a one-dimensional spatial dependence. A uniform plane wave is a transverse electromagnetic (TEM) wave, meaning that the electric and magnetic fields are perpendicular to the direction of propagation and to each other. [3] The plane wave equation is determined using the homogeneous vector Helmholtz equations. A uniform

plane wave does not exist in practise, because it would require a source infinite in extent to create it. However, far enough from the source, the plane wave provides a good approximation of the electromagnetic wave. This is because the wave front is spherical and far enough from the source a very small portion of the surface of the large sphere is nearly a plane.

Plane waves in lossless media

In a lossless medium the wave number k is real since ε and μ are real numbers. A plane wave solution to the homogeneous vector Helmholtz equations is found by assuming an electric field with only a $\bar{x}$ component and no variations in the x and y directions and the only variation occurs in the z direction. These assumptions reduce Eq. (2.14) to [1]:

$$\frac{\partial^2 E_x}{\partial z^2} + k^2 E_x = 0. \tag{2.15}$$

The solution to this equation is:

$$E_x(z) = E^+ e^{-jkz} + E^- e^{jkz}, \tag{2.16}$$

where E^+ and E^- are arbitrary amplitude constants that may be complex. Assuming that these amplitude constants are real, the above solution can for the time harmonic case be written as:

$$E_x(z,t) = E^+ \cos(\omega t - kz) + E^- \cos(\omega t + kz). \tag{2.17}$$

The first term of Eq. (2.17) represents a plane wave of amplitude E^+ propagating in the $+z$ direction and the second term a plane wave of amplitude E^- propagation in the $-z$ direction. To maintain a fixed point on the wave, the phase should be constant, that is ($\omega t - kz$) = constant. The velocity of a fixed phase point on the wave is called the phase velocity and is given by [1]:

$$v_p = \frac{\omega}{k} = \frac{1}{\sqrt{\mu' \varepsilon'}}. \tag{2.18}$$

In free-space $v_p = c = 2.998 \cdot 10^8$ m/s, which is the speed of light. The wavelength λ is defined as the distance between consecutive points of the same phase and can be written as:

$$\lambda = \frac{2\pi}{k} = \frac{v_p}{f}. \tag{2.19}$$

The magnetic field vector is attained using the same assumptions as for the electric field vector and by using one of Maxwell's curl equations. The result is a magnetic field having only a $\bar{y}$ component that is perpendicular to the electric field [1]:

$$H_y(z) = \frac{1}{\eta} E_x(z,t), \tag{2.20}$$

where $\eta = \sqrt{\mu' / \varepsilon'}$ is the wave impedance for the plane wave and the ratio of the electric and magnetic fields.

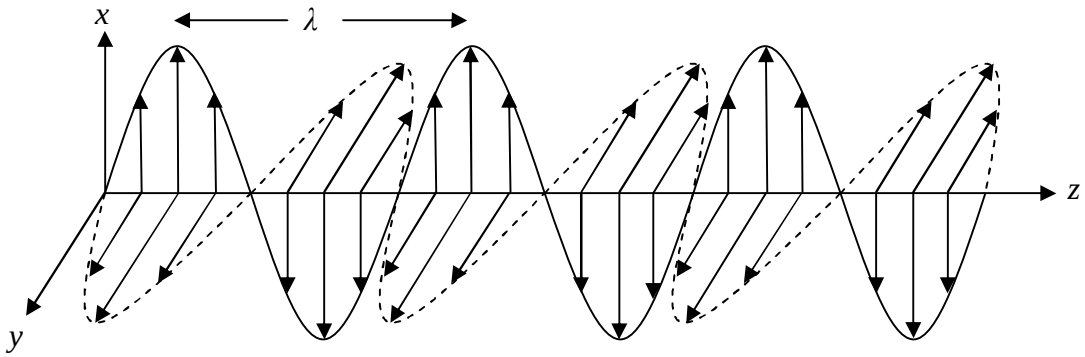

Fig. 2.1. Electric (solid line) and magnetic (dashed line) fields of a uniform electromagnetic plane wave propagation in the +*z* direction at time *t*.

Both the electric and magnetic field vectors are orthogonal to the direction of propagation. A plane wave propagating in the +*z* direction is depicted in Fig. 2.1.

Plane waves in dielectric lossy media

In practise, the electric and magnetic fields need to be solved in a lossy material, which has a conductivity deviating from zero. As remembered, the permittivity for a lossy dielectric material is complex. In a source-free lossy dielectric medium the wave number in the homogeneous Helmholtz's equation is hence a complex number. Assuming again an electric field with only a $\bar{x}$ component and no variations in the *x* and *y* directions, the homogeneous vector Helmholtz equation reduces to [1]:

$$\frac{\partial^2 E_x}{\partial z^2} - \gamma^2 E_x = 0, \tag{2.21}$$

where the complex propagation constant γ for the medium is defined as [3]:

$$\gamma = \alpha + j\beta = j\omega\sqrt{\mu'\varepsilon'}\left(1+\frac{\sigma}{j\omega\varepsilon'}\right)^{1/2}. \tag{2.22}$$

The solution for Eq. (2.21) is:

$$E_x(z) = E^+e^{-\gamma z} + E^-e^{\gamma z} = E^+e^{-\alpha z}e^{-j\beta z} + E^-e^{\alpha z}e^{j\beta z}. \tag{2.23}$$

The propagation factor in time domain for the positive propagation wave is of the form:

$$e^{-\gamma z} = e^{-\alpha z}\cos(\omega t - \beta z), \tag{2.24}$$

which represents a wave with a phase velocity of $v_p = \omega/\beta$ (β is the phase constant), a wave length of $\lambda = 2\pi/\beta$, and an exponential damping factor. The rate of decay with distance is given by the attenuation constant α. The SI unit for α is neper per meter (Np/m). For a lossless medium $\sigma = 0$ ($\varepsilon = \varepsilon'$), $\alpha = 0$ and $\beta = k = \omega\sqrt{\mu'\varepsilon'}$. The associated magnetic field vector is calculated as [1]:

$$H_y(z) = \frac{1}{\eta}(E^+e^{-\gamma z} - E^-e^{\gamma z}), \tag{2.25}$$

where $\eta = j\omega\mu'/\gamma$ is the wave impedance for the lossy case. As seen, the electric and magnetic fields are perpendicular to each other and to the propagation direction, as for the lossless case. This time, however, the fields attenuate exponentially as the electromagnetic wave propagates in the lossy dielectric medium.

Plane waves in good conductors

For a good conductor the approximation $\sigma >> \omega\varepsilon'$ is valid [3]. The complex propagation constant may consequently be written as [3]:

$$\begin{aligned}\gamma &= \alpha + j\beta \cong (1+j)\sqrt{\pi f\mu'\sigma},\\ \alpha &= \beta = \sqrt{\pi f\mu'\sigma}.\end{aligned} \tag{2.26}$$

The skin depth is defined as [3]:

$$\delta_s = \frac{1}{\alpha} = \sqrt{\frac{2}{\omega\mu'\sigma}}. \tag{2.27}$$

This is the depth below the surface of a conductor at which the amplitude of an incident electric field has decreased by a factor $e^{-\alpha z} = 1/e$. At microwave frequencies the

electromagnetic wave is attenuated very rapidly as it propagates in a good conductor. In fact, the skin depth is so small that fields and currents can be considered confined in a very thin layer (in the skin) of the conductor surface. Therefore, at UHF, the conductive antenna pattern can be made to have a thickness of the same order of magnitude as the skin depth.

Polarisation of plane waves

By definition the polarisation of an antenna is the polarisation of the electromagnetic wave radiated in a given direction by the antenna when transmitting [5]. When the direction is not stated, the polarisation is taken to be the polarisation in the direction of maximum antenna gain [4]. Usually, the polarisation characteristics of an antenna remain relatively constant over its main beam. However, the polarisation characteristics of the minor lobes can differ greatly from that of the main beam [5].

Polarisation of a uniform plane wave refers to the time-dependent orientation of the electric field vector at a given point in space. For TEM waves, the polarisation is perpendicular to the direction of propagation. In general, the figure traced out of the instantaneous electric field is an ellipse. Linear and circular polarisations are both important special cases of elliptical polarisation. The electric field in Fig. 2.1 is linearly polarised; the electric filed moves back and forth along a line. If the electric field remains constant in amplitude but rotates around in a circular path it is defined as circularly polarised. Rotation direction at radian frequency ω defines if the circular polarisation is right- or left-hand polarised. A wave propagating towards the observer with the electric field rotating clockwise is left-hand polarised. If the rotation is counter-clockwise, the wave is right-hand polarised.

A general polarisation ellipse is illustrated in Fig. 2.2. The instantaneous electric field $\boldsymbol{E}$ has components E_x and E_y along the x and y directions. The amplitudes of these components are E_1 and E_2, respectively. The angle γ describes the relative values of E_1 and E_2 from [5]:

$$\gamma = \tan^{-1}\frac{E_2}{E_1}. \qquad 0° \le \gamma \le 90° \tag{2.28}$$

The polarisation ellipse is characterised by the axial ratio (AR). The axial ratio is defined as the ratio of the major axis electric field E_{max} component to that of the minor axis E_{min}. It is often expressed in dB. At $z = 0$ the instantaneous electric field of Fig. 2.2 can in time domain be written as [5]:

$$\overline{E}(z,t) = E_x\overline{x} + E_y\overline{y} = E_1\cos(\omega t)\overline{x} + E_2\cos(\omega t + \delta)\overline{y}, \tag{2.29}$$

where δ is the phase difference from the y component to the x component.

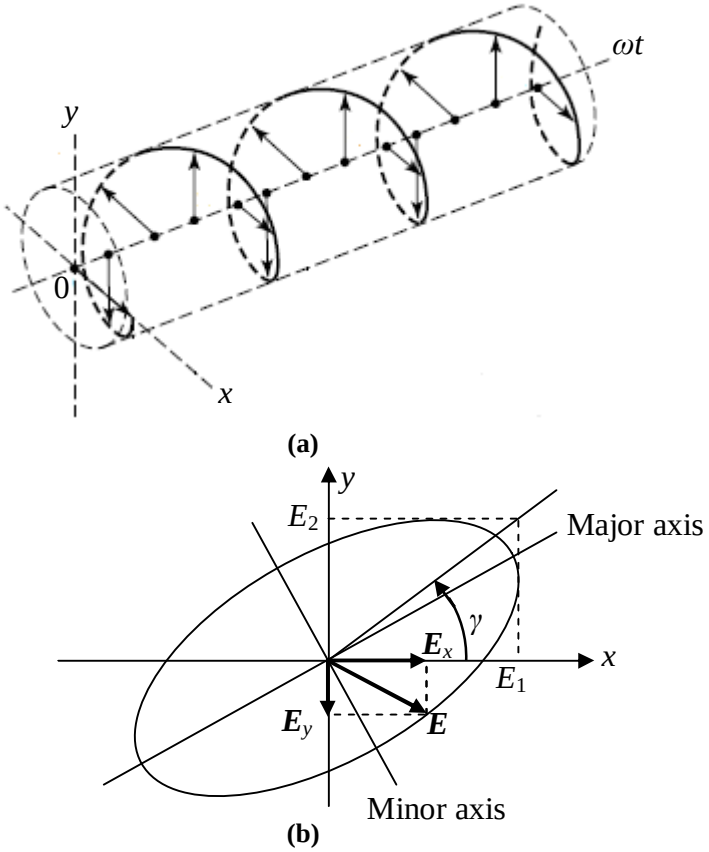

Fig. 2.2. **(a)** Rotation of a plane electromagnetic wave at a fixed instant of time and **(b)** polarisation ellipse at $z = 0$ as a function of time. Picture edited from [4].

The net electric field vector is linearly polarised if the components are in phase, that is, $\delta = 0$. The orientation of linear polarisation is determined by the relative values of E_1 and E_2. Vertical linear polarisation is resulted if $E_1 = 0$, and if $E_2 = 0$ horizontal linear polarisation is resulted. If $E_1 = E_2$ are both nonzero, there is a linearly polarised plane wave at the angle γ. For linear polarisation the value of E_{min} is zero and hence, the ellipse has infinite axial ratio. If the components are out-of-phase, that is $\delta \neq 0$, both E_{min} and E_{max} are present and the axial ratio is finite. When $\overline{E}_y$ leads $\overline{E}_x$ in phase, $\delta > 0$ and the sense of polarisation is left-hand. The sense of polarisation is right-hand if $\delta < 0$. Circular polarisation results if $E_1 = E_2$ and $\delta = \pm 90°$. In this case, E_{max} equals E_{min} and the axial ratio is unity.

2.1.4 Electromagnetic energy and power

Electromagnetic waves carry electromagnetic power. Poynting's theorem is often used to describe the power transfer. The theorem states the energy conservation for electromagnetic fields and relates the power and energy of the fields.

The energy conservation for electromagnetic fields can be considered for a volume V inside a closed surface S with the parameters ε_r, μ_r and σ [6]. Inside the volume, an electromagnetic source $\boldsymbol{J}$ generates electromagnetic fields that deliver complex power:

$$P_s = -\frac{1}{2}\int_V \left(\boldsymbol{E}\cdot\boldsymbol{J}^*\right)dV. \tag{2.30}$$

The time-averaged stored electric W_e and magnetic W_m energies in the volume are given by:

$$\begin{aligned} W_e &= \frac{\varepsilon_0}{4}\int_V \varepsilon_r^{'}\left|\boldsymbol{E}\right|^2 dV, \\ W_m &= \frac{\mu_0}{4}\int_V \mu_r^{'}\left|\boldsymbol{H}\right|^2 dV. \end{aligned} \tag{2.31}$$

Poynting's vector $\boldsymbol{P}$ gives the complex power flow through the closed surface S as:

$$\boldsymbol{P} = \boldsymbol{E}\times\boldsymbol{H}^*. \tag{2.32}$$

Poynting's vector gives the instantaneous field intensity at a point in space per surface unit. Thus the unit is W/m^2. Poynting's vector also gives the direction of the power flow. For time-harmonic fields the time-average power flow through the closed surface S is given by:

$$P_0 = \frac{1}{2}\mathrm{Re}\int_{\partial V} \boldsymbol{E}\times\boldsymbol{H}^*\cdot d\boldsymbol{S}. \tag{2.33}$$

The time-averaged power dissipated by the medium due to ohmic, dielectric and magnetic losses can be derived as:

$$P_l = \frac{1}{2}\int_V \sigma\left|\boldsymbol{E}\right|^2 dV + \frac{\omega}{2}\int_V \left(\varepsilon_0\varepsilon_r^{''}\left|\boldsymbol{E}\right|^2 + \mu_0\mu_r^{''}\left|\boldsymbol{H}\right|^2\right)dV. \tag{2.34}$$

The energy conservation equation (Poynting's theorem) in frequency domain can now be written as:

$$P_s = P_0 + P_l + 2j\omega(W_m - W_e). \tag{2.35}$$

The theorem states that the source power P_s inside the volume is the sum of the transmitted power P_0 through the closed surface, material losses P_l and 2ω times the net reactive energy stored in the volume ($W_m - W_e$).

2.2 Antenna theory

An antenna is a conducting device that can receive or transmit electromagnetic waves. For wireless communication system, the antenna is one of most critical components [4]. In addition to the capability of receiving and transmitting energy, an antenna is usually required to optimise and emphasise the radiating energy in some direction and suppress it in others: the antenna must serve as a directional device. Reciprocity is a fundamental property of antennas, implying that the electrical characteristics of an antenna are the same whether the antenna is transmitting or receiving. The application determines if the antenna is acting as a transmitting or receiving device. In transmission, a time-varying current on the antenna generates free-space electromagnetic waves. In reception, the free-space electromagnetic waves incident on the antenna structure induces time-varying currents.

2.2.1 Radiation mechanism

Maxell's equations state that when charges accelerate or decelerate radiation is generated. These charges cause electromagnetic fields that are guided within the transmission line and the antenna and detached from the antenna as free-space electromagnetic waves. The fundamental relation of electromagnetic radiation can be derived by considering a wire as a source and the generation of free-space electromagnetic waves can be understood through illustration.

The current density over the cross section A of a circular conducting wire with volume V is [4]:

$$J_z = q_v v_z, \tag{2.36}$$

where q_v is the volume charge density distributed uniformly in the wire and v_z is uniform velocity of the total charge Q in the z direction. For an ideal electric conductor the current density is restricted to the surface of the wire and it is given by:

$$J_s = q_s v_z, \tag{2.37}$$

where q_s is the surface charge density. For a very thin wire, ideally with zero diameter, the current in the wire is simply:

$$I_z = q_l v_z, \tag{2.38}$$

where q_l is the charge per unit length. For a time-varying current in a very thin wire, the time derivative of the current in the wire of length l is:

$$l\frac{dI_z}{dt} = lq_l\frac{dv_z}{dt} = lq_l a_z. \tag{2.39}$$

Eq. (2.39) is the fundamental relation of electromagnetic radiation: to create radiation, there must be a time-varying current or an acceleration of charge. If current is not moving, acceleration is not created and there is no radiation. If charge is moving with a uniform velocity there is no radiation if the wire is straight and infinite in extent. However, if charge is oscillating in time-motion radiation is created even if the wire is straight. Additionally, there is radiation if the wire is curved, bent, discontinuous, terminated or truncated because the direction of the charges is changing. [4]

The creation of free-space electromagnetic waves is illustrated in Fig. 2.3. A voltage source is connected to a two-conductor transmission line which is connected to a small dipole antenna. The applied voltage across the transmission line creates an electric field between the conductors. The electric lines of force act on the free electrons associated with each conductor and force them to be displaced. The movement of the charges generates a current that creates magnetic field intensity. When the voltage source is sinusoidal, also the electric field between the conductors is sinusoidal with a period equal to that of the applied source. This time-varying electric and magnetic fields creates electromagnetic waves that propagate along the transmission line and enter the antenna to finally form free-space waves by connecting the open ends of the electric lines as shown in dashed.

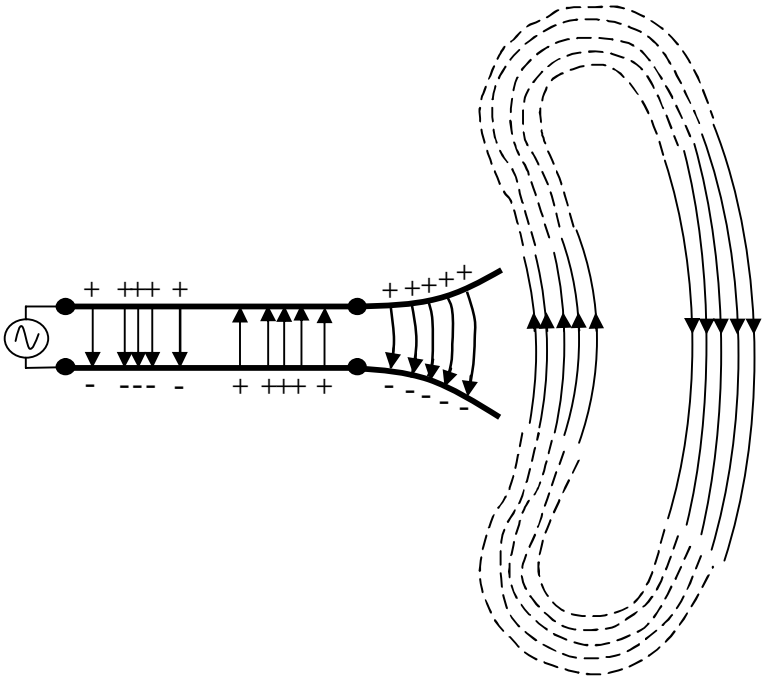

Fig. 2.3. Creation of free-space electromagnetic waves from an antenna. Picture edited from [4].

After one-half of a period there is no net charge on the antenna conductors because it can be thought that applied opposite charges have neutralised the charges on the conductors. This results in that the electric lines of force are detached from the

conductors to form closed loops. During the second half on the period the procedure is repeated in the opposite direction. It should be noted that electric charges are required to excite the fields but are not needed to sustain them. The electromagnetic waves do exist even if the electric charges are removed after the excitation. [4]

2.2.2 Fundamental antenna parameters

Some important antenna parameters are described here. Due to the reciprocity theorem, all antenna parameters apply to both antenna transmitting and receiving mode.

Radiation pattern

An antenna radiation pattern is defined as a mathematical function or graphical representation of the radiation properties of the antenna as a function of space coordinates [4]. Typically, the radiation pattern is a far-field property. A convenient coordinate system for antenna radiation pattern analysis is shown in Fig. 2.4.

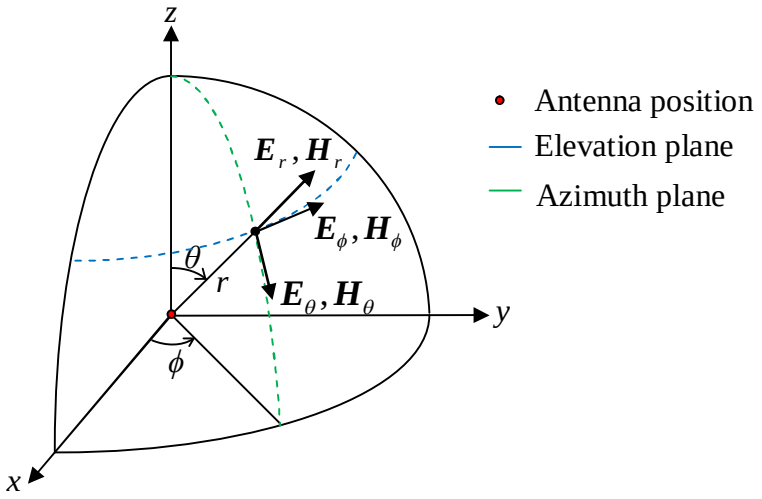

Fig. 2.4. Typical coordinate system used for antenna radiation pattern analysis. The field pattern in linear scale represents a plot of the magnitude of the electric or magnetic field as a function of angular space. The power pattern in linear scale represents a plot of the square of the magnitude of the electric or magnetic field as a function of the angular space. The power pattern in decibels represents the magnitude of the electric or magnetic field as a function of the angular space. Picture edited from [4].

For most applications, a series of two-dimensional patterns provide the most useful and needed information about the antenna radiation pattern, for example the *E*- and *H*-plane patterns as described later. In general, at each observation point on the surface of a sphere of constant radius there are three electric field components $\boldsymbol{E}_r$, $\boldsymbol{E}_\theta$ and $\boldsymbol{E}_\phi$, and the magnitude of the total electric field is:

$$\left|\boldsymbol{E}\right| = \sqrt{\left|E_r\right|^2 + \left|E_\theta\right|^2 + \left|E_\phi\right|^2}. \tag{2.40}$$

However, in the far-field, the radial component E_r is zero or vanishingly small compared to one or both of the two other components [4].

Parts of the radiation pattern are referred to as lobes, which are classified into main, minor, side and back lobes as shown in Fig. 2.5.

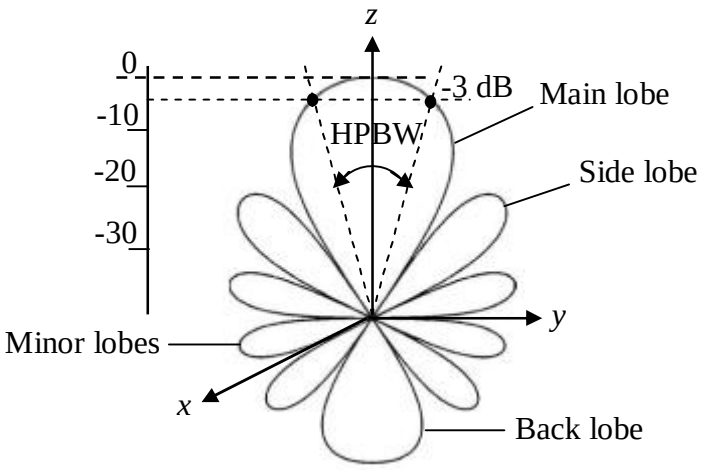

Fig. 2.5. Radiation lobes of an antenna. Picture edited from [4].

The main lobe is the radiation lobe containing the direction of maximum radiation, while a minor lobe is any other lobe except the main lobe. A side lobe is a radiation lobe in any direction other than the intended lobe. Usually, the side lobe is adjacent to the main lobe. A back lobe usually refers to a minor lobe that makes an angle in a direction opposite to that of the main lobe. Minor lobes are usually undesired because they represent radiation in undesired directions. The ratio of power density in the minor lobe in question to that of the main lobe is defined as the minor lobe level. In radar systems, low minor lobe levels are required to minimise false target indications.

The beamwidth of a radiation pattern is an important figure of merit used to describe the resolution capabilities of the antenna to distinguish between two adjacent radiating sources or radar targets. It is defined as the angular separation between two identical points on opposite side of the pattern maximum. The half-power beamwidth (HPBW) is one of the most widely used beamwidths and is defined as: In a plane containing the direction of the maximum of a beam, the angle between two directions in which the radiation intensity is one-half value of the beam, refer to Fig. 2.5. There is always a trade-off between the beamwidth and the side lobe level. As the beamwidth decreases, the side lobe level increases and vice versa. [4]

The radiation pattern can be isotropic, directional or omnidirectional. An isotropic radiator is an ideal antenna having equal radiation in all directions. A directional antenna directs the radiation more effectively in some direction than in others. Antennas having maximum directivity greater than that of a half-wave dipole are usually classified as directional antennas [4]. An omnidirectional radiation pattern is a special type of directional pattern. An omnidirectional radiator has an essentially non-directional pattern in a given direction and a directional pattern in any orthogonal plane.

For a linearly polarised antenna, the radiation patterns are often given for its principal *E*- and *H*-plane patterns. The *E*-plane contains the electric field vector and the direction of maximum radiation, whereas the *H*-plane contains the magnetic field vector and the direction of maximum radiation. A usual practise is to orient the antenna so that at least one of the principal planes coincides with one of the geometrical principal patterns. The dipole antenna is linearly polarised and has an omnidirectional radiation pattern as illustrated in Fig. 2.6. The pattern has infinite number of principal *E*-planes (*xz*-planes, ϕ is constant) and one principal *H*-plane (*xy*-plane, $\theta = 90°$).

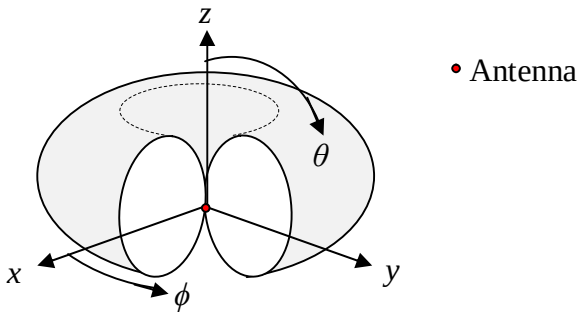

Fig. 2.6. Far-field omnidirectional radiation pattern of a dipole antenna.

The field structure varies at different distances from the antenna in the surrounding space. The space near the antenna is therefore divided into three regions [4]: reactive near-field, radiating near-field (Fresnel) and far-field (Fraunhofer). The boundaries separating these regions are not unique and there are no radical changes in the field structure at the boundaries. However, there are distinct differences between the regions and various established criteria are used to identify them as follows [4].

The reactive near-field region surrounds immediately the antenna and within this region the reactive field predominates. The region is commonly defined to reach to a distance of $r < 0.62\sqrt{D^3/\lambda}$ from the antenna surface, where *D* is the largest dimension of the antenna. For a short dipole the distance is typically defined as $\lambda/2\pi$.

The radiating near-field is the region between the reactive near-field and the far-field region. In this region the radiation field predominate and the field pattern is dependent upon the distance from the antenna and the radial field component may be notable. For antennas with maximum dimension that is comparable to the wavelength, this region may not exist. This region is taken to extend from the reactive near filed region boundary to the distance $r < 2D^2/\lambda$ from the antenna surface where $D > \lambda$.

In the far-field region the field pattern is independent of the distance from the antenna. The far-field exists at distances greater than the radiating near-field.

Directivity

Directivity is in addition to the beamwidth a measure of the focusing capability of the antenna. It describes how well the antenna concentrates energy in one direction in space

relative to radiation in other directions. It is defined as the ratio of the radiation intensity in a certain direction to the average radiation intensity [5]:

$$D(\theta,\phi) = \frac{U(\theta,\phi)}{U_{ave}}, \tag{2.41}$$

where the average radiation intensity $U_{ave} = P/(4\pi)$ equals the radiation intensity that an isotropic source with the same input power P would radiate. Directivity is also the ratio of the power density in a certain direction at a given range r to the average power density at that range. The directivity can thus be written as [5]:

$$D(\theta,\phi) = \frac{4\pi}{\Omega_A}\left|F(\theta,\phi)\right|^2, \tag{2.42}$$

where $F(\theta,\phi)$ is the normalised field pattern and Ω_A is the beam solid angle:

$$\Omega_A = \iint \left|F(\theta,\phi)\right|^2 d\Omega, \tag{2.43}$$

where $d\Omega = \sin\theta d\theta d\phi$ is element of solid angle. Eq. (2.43) shows that the directivity is entirely determined by the pattern shape. The beam solid angle is illustrated in Fig. 2.7.

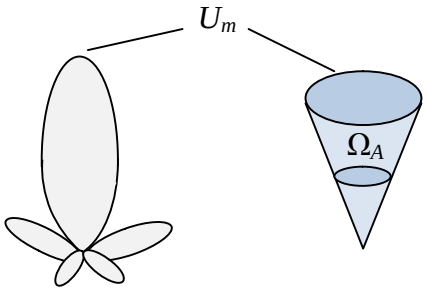

Fig. 2.7. Beam solid angle Ω_A through which all the power would be radiated if the power per unit solid angle equalled the maximum value U_m over the beam area. With other words, the cone of solid angle Ω_A concentrates all radiation from the actual antenna. The constant radiation intensity of the cone equals the maximum of the actual pattern.

The maximum directivity D follows from Eq. (2.41) as $D = U_m/U_{ave}$. It can be shown that the maxim directivity is given by [5]:

$$D = \frac{4\pi}{\Omega_A}. \tag{2.44}$$

Since the radiation intensity can be expressed as $U(\theta,\phi) = U_m\left|F(\theta,\phi)\right|^2$, the directivity of Eq. (2.41) can be written as:

$$D(\theta,\phi) = \frac{U_m \left|F(\theta,\phi)\right|^2}{U_{ave}} = D\left|F(\theta,\phi)\right|^2. \tag{2.45}$$

Since the normalised field pattern has a maximum value of unity, the maximum value of directivity is *D*. For an ideal isotropic antenna $U_m = U_{ave}$ and the directivity is unitary. For an actual radiator the maximum radiation intensity is $U_m = DU_{ave}$ in the direction $(\theta_{\max},\phi_{\max})$ and the average radiation intensity is $P/4\pi$. The directivity *D* of an ideal dipole can be calculated to be 1.5 [5].

Gain

The (power) gain is used to quantify how efficiently the antenna transforms available power at its input to radiated power together with its directive properties. The gain is expressed as [5]:

$$G(\theta,\phi) = \frac{4\pi U(\theta,\phi)}{P_{in}}, \tag{2.46}$$

where the radiation intensity includes the inherent antenna losses but not mismatches of impedance or polarisation, and P_{in} is the accepted antenna input power. The maximum gain is attained for $U(\theta,\phi) = U_m$.

Input impedance

Input impedance is defined as the impedance presented by an antenna at its terminals or the ratio of the voltage to current at a pair of terminals or the ratio of the appropriate components of the electric to magnetic fields at a point [4]. The ratio of the voltage to current at antenna input terminals with no load attached defines the input impedance as:

$$Z_A = R_A + jX_A, \tag{2.47}$$

where the dissipative part R_A consists of antenna radiation resistance R_r and antenna loss resistance R_{ohmic}. The reactive part represents the storage capability of the antenna near-field. It can be shown that the power transfer from the antenna terminals to the antenna load $Z_L = R_L + jX_L$ at the terminals is maximised when the antenna input impedance and the load impedance are conjugate-matched [7]:

$$Z_A = Z_L^*. \tag{2.48}$$

When conjugate matching occurs, half of the power provided by the generator is dissipated as heat in the internal resistance and the other half is delivered to the antenna. Part of the power delivered to the antenna is radiated through the radiation resistance

and the other part is dissipated as heat. Similarly, in the antenna transmitting mode, half of the power captured is delivered to the load and the other half is scattered or re-radiated through R_r and dissipated as heat through R_{ohmic}. [4] Conjugate matching is only achieved within a limited bandwidth since the antenna input impedance is a function of frequency. The antenna input impedance depends on the antenna geometry, excitation method and surrounding objects.

Efficiency

The directivity can be understood as the gain an antenna would have if all input power would be transferred into radiated power so that $P_{in} = P$. Gain represents the real case where some of the input power is lost as ohmic losses including conduction and dielectric losses on the antenna. The radiation efficiency e_r is defined as [5]:

$$e_r = \frac{P}{P_{in}}, \qquad 0 \le e_r \le 1. \tag{2.49}$$

The maximum directivity and gain are hence related through e_r as follows [5]:

$$G = e_r D. \tag{2.50}$$

The radiation efficiency can also be defined as the ratio of the power delivered to the radiation resistance R_r to the power delivered to R_r and R_{ohmic}:

$$e_r = \frac{R_r}{R_r + R_{ohmic}}. \tag{2.51}$$

The total antenna efficiency e_{tot} is used to take into account losses at the input terminals and within the antenna structure [4]:

$$e_{tot} = e_r e_{ref} = e_r (1 - |\Gamma|^2), \tag{2.52}$$

where e_{ref} is the reflection mismatch efficiency at the antenna input terminals. The voltage reflection coefficient Γ is defined as:

$$\Gamma = \frac{Z_A - Z_0}{Z_A + Z_0}, \tag{2.53}$$

where Z_0 is the characteristic impedance of the transmission line.

Equivalent isotropic radiated and equivalent radiated power

In communication systems and power regulations the powers are typically referred to as equivalent isotropic radiated power (P_{EIRP}) and equivalent radiated power (P_{ERP}). P_{EIRP} is the amount of power that has to be supplied in a theoretical isotropic antenna in order to produce the same peak radiation power as in the main beam of the actual directional antenna with gain G_t observed at a distance r [7]:

$$P_{EIRP} = P_t\,(\text{dBm}) + G_t\,(\text{dBi}). \tag{2.54}$$

P_{ERP} is the amount of power that has to be supplied in half-wave dipole antenna in order to produce the same peak radiation power as in the main beam of the actual directional antenna observed at a distance r [7]:

$$P_{ERP} = P_t\,(\text{dBm}) + G_t\,(\text{dBd}). \tag{2.55}$$

The gain of an ideal isotropic antenna and half-wave dipole are 1 (0 dB) and 1.64 (2.15 dB), respectively. The relationship between P_{EIRP} and P_{ERP} becomes:

$$\begin{aligned} &P_{EIRP} = 1.64 P_{ERP}, \\ &P_{EIRP}\,(\text{dBm}) = 2.15\,\text{dB} + P_{ERP}\,(\text{dBm}). \end{aligned} \tag{2.56}$$

2.2.3 Effective aperture and radar cross section

Antennas are used in communication, radar, and radiometer systems. A simple communication link is depicted in Fig. 2.8 showing the transmitter with transmitting antenna and the receiver with receiving antenna.

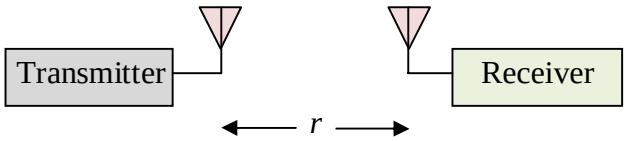

Fig. 2.8. Communication link between the transmitter and receiver at distance r from each other.

When the transmitting and receiving antennas are matched to their loads (transmission line or, in the case of a tag antenna, tag IC), co-polarised, aligned to each other's main beam direction, and the transmitted electromagnetic wave electric field attenuates proportionally to $1/r^2$, that is the wave propagating medium is free-space, the power received P_r by an antenna at a distance of r from the transmitting antenna is given by Friis transmission formula [5]:

$$P_r = P_t G_t G_r \left(\frac{\lambda}{4\pi r} \right)^2, \tag{2.57}$$

where λ is the transmitted wavelength, P_t is the power sent by the transmitter antenna, G_t and G_r are the power gains of the transmitter and receiver antenna, respectively. Friis formula estimates the maximum power transfer between the transmitting and receiving antennas. When any of the Friis formula conditions are not met, the received power will be different than the estimated by Eq. (2.57).

The total power incident on the receiving antenna is found by summing up the incident power density over the so-called effective aperture of the receiving antenna. The effective aperture A_e (m^2) is in a given direction defined as the ratio of the available power P_A at the terminals of a receiving antenna to the power flux density S of a plane wave incident on the antenna from that direction, and with the wave being co-polarised with the antenna [4]. The maximum power available from the antenna is realised when the antenna is matched to its load impedance, directed for maximum response and polarisation-matched. Additionally, it is assumed that there are no ohmic losses on the antenna. The maximum available power $P_{a,max}$ can be given with use of the maximum effective aperture $A_{e,max}$ [5]:

$$P_{a,\max} = SA_{e,\max}. \tag{2.58}$$

In practise, however, antennas are not completely lossless. The power received by a receiving antenna is reduced to the radiation efficiency e_r fraction of what it would be if the antenna was lossless. The available power P_A including the antenna losses can thus be written as [5]:

$$P_A = e_r SA_{e,\max} = SA_e. \tag{2.59}$$

With other words, Eq. (2.59) states that a receiving antenna is able to convert incident flux power density to power delivered to the load. Only inherent antenna losses are included in A_e, whereas polarisation and impedance mismatch losses are not included since these losses are dependent on how the antenna is used in the application system. The maximum aperture can be given as a function of the receiving antenna maximum gain G_r as:

$$A_{e,\max} = G_r \frac{\lambda^2}{4\pi}. \tag{2.60}$$

The antenna losses are included in the G_r term. The mismatch term can be expressed with the aid of a reflection coefficient, known as the Kurokawa power reflection coefficient [8]:

$$\Gamma^* = \frac{Z_L - Z_A^*}{Z_L + Z_A}, \tag{2.61}$$

where Γ^* is the conjugate-matched power reflection coefficient, Z_A is the receiving antenna input impedance and Z_L is the load impedance. Now, the effective aperture can be written to include the antenna losses and the effect of impedance mismatch loss such that:

$$A_e = A_{e,\max}\left(1 - \left|\Gamma^*\right|^2\right). \tag{2.62}$$

In some cases, it is interesting to know how an antenna scatters energy into surrounding space. The radar cross section σ (RCS) is a far-field parameter, which is used to characterise the scattering properties of a radar target [9]. In general, the RCS of a target is a function of the polarisation of the incident wave, the angle of incident, the angle of observation, the target geometry, the target electrical properties and the frequency of operation [4]. There are several ways to analyse the fields scattered by an antenna. Here, the scattered field by the antenna terminated with a load Z_L is separated into the structural and the antenna mode scattering terms. The antenna mode component of the scattered field is completely determined by the radiation characteristics of the antenna. The component is related to the energy absorbed in the load of a lossless antenna and the energy radiated by the antenna due to load mismatch. The antenna radiation pattern is identical to that of the pattern of the energy scattered in the antenna mode. When the antenna is conjugate-matched, the antenna mode vanishes and the power delivered to the load is half of the captured power by the antenna, and the other half is re-radiated through radiation resistance R_r as the power $P_{re\text{-}rad}$. The structural scattering component arises from the currents induced on the antenna surface by the incident wave even when the antenna is conjugate-matched. [5] For RFID tag antennas it is convenient to assume that the antenna mode is large compared to the structural mode [10]. It is possible to derive the following expression for the antenna mode component of the radar cross section as [5]:

$$\sigma_{ant} = \frac{P_{re-rad}}{S} = \Gamma^2 G_r^2 \frac{\lambda^2}{4\pi} = \Gamma^2 G_r A_{e,\max}, \tag{2.63}$$

where Γ is the reflection coefficient between the antenna input impedance and the antenna load impedance. If an incident power flux density S is observed at the tag antenna location, the tag antenna backscatters a power equal to $P_{re\text{-}rad} = S\sigma_{ant}$. An antenna loaded with a conjugate impedance load re-radiates the same amount of power as the load absorbs.

2.3 The passive UHF RFID system

The wireless communication system concerned in this project is the passive UHF RFID system. Here, basic antenna theory from previous subsection is applied to describe the basic principles and concepts of the system.

2.3.1 System review

Ultra-high frequency (UHF) radio frequency identification (RFID) is a wireless identification technology used to track and identify different objects. Today, the technology finds applications for example in access control, security, inventory management and bio-medical applications. The identification is established by the wireless communication between the on-object attached tag and the in the surrounding located reader antenna. The tag is comprised of an antenna and an application specific circuit (ASIC). The information about the tagged object is located in the ASIC memory as electronic product code (EPC), which is read by the reader unit connected to the reader antenna. RFID provides several advantages over traditional barcode systems. At UHF, the wireless communication ranges between the tag and the reader are significantly longer than the ranges provided by the barcode system. Moreover, the communication does not require direct line of sight; tags can even be read through some obstacles. Further, multiple RFID tags can be read in shorter time and their large memory storage enables conveyance of more information than a typical barcode.

The wireless communication at UHF takes typically place as electromagnetic coupling in the far-field. The tag antennas are of the same order of magnitude in size as the wave length. The electric field attenuates proportionally to $1/r^2$, where r is the distance from the reader antenna. Data transfer between the tag and the reader is established by modulation of backscattered radiation from the tag antenna using load modulation. Passive tags are dependent on the energy-carrying electromagnetic wave from the reader antenna. Active tags include also an internal energy source, for example a battery, to increase the power supply to the IC. The sensitivity of active RFID systems is thus better than for passive systems, and as a consequence, the communication range for passive system is more limited. However, the additional energy source increases the tag prise. For passive UHF systems, the read range is several metres, whereas for active systems it can even be 100 metres. Since the operation of RFID system involves propagation of electromagnetic waves, nearby objects of various electromagnetic properties will influence the communication between the tag and the reader. As remembered, materials such as metals and liquids bring challenges because they attenuate and reflect the electromagnetic wave from the reader antenna. It is therefore of paramount importance to take the application environment into consideration early in the tag design. Typically, the tag is optimised to operate in its application environment, which to large extent determines the achievable tag performance characteristics. [7]

The RFID system operating frequency determines the electromagnetic coupling and data transfer mechanism. Systems operating at the low-frequency (LF) band

125/134 kHz, and the high-frequency (HF) band 13.56 MHz, usually utilise inductive coupling in the near-field for data transfer and communication. The reader-to-tag system acts as a magnetic transformer providing coupling between current flowing in the reader antenna and the voltage across the tag. The antennas are often large loop antennas. All available energy is thus in the reader antenna close proximity and proportional to the reader antenna size. The electric field attenuates proportionally to $1/r^3$. In these applications the read range exceeds hardly one metre. However, at LF and HF the system operation is less affected by nearby objects and materials. Systems operating at 860–960 MHz and 2.4–2.45 GHz are both within the UHF RFID band. The read range for UHF applications mostly exceeds one metre. LF RFID is particularly appropriate for animal and human ID, and access control. People and animals are often inspected with short-range handheld reader. HF RFID is widely used for non-contact smart cards, asset tracking and supply management. [7]

RFID systems generate and radiate electromagnetic waves, whereby they are classified as radio systems. The function of other radio services must under no circumstances be disrupted or impaired by the operation of RFID systems. The International Telecommunication Union (ITU) is the United Nations specialised agency for information and communication technologies, that globally standardises and regulates the frequency bands and power limits. ITU has three regional organisations. In Europe, the radio communication is regulated by European Conference of Postal and Telecommunications (CEPT), and its sub-organisation European Telecommunications Standards Institute (ETSI). In North America the regulation is controlled by the Federal Communications Commission (FCC). In Asia and Australia the radio communication is controlled by the Ministry of Posts and Telecommunications (MPT). The allocated UHF RFID bands for Europe, United States, and Japan are 865–868 MHz, 902–928 MHz, and 952–954 MHz, respectively. In Europe ETSI restricts the EIRP to 3.28 W, whereas in United States and Japan the power is regulated to 4 W. [7]

2.3.2 System block diagram and operation

All RFID systems include the same basic components between which the wireless communication takes place. A typical RFID system consists of three basic components: a transponder (tag), an interrogator (reader) and a reader antenna to send and receive energy and data to and from the tag. The reader antenna or antennas may be integrated with the reader or physically separated and connected via a cable. In the radio link, the forward link (RX to TX) is referred to the communication channel carrying information and power from the reader to the tag, whereas the communication from tag to reader is referred as the reverse link (TX to RX). The reader is usually connected to a computer to provide a user interface. The computer is used to control the data transfer and to display and store data. The RFID system block diagram is illustrated in Fig. 2.9.

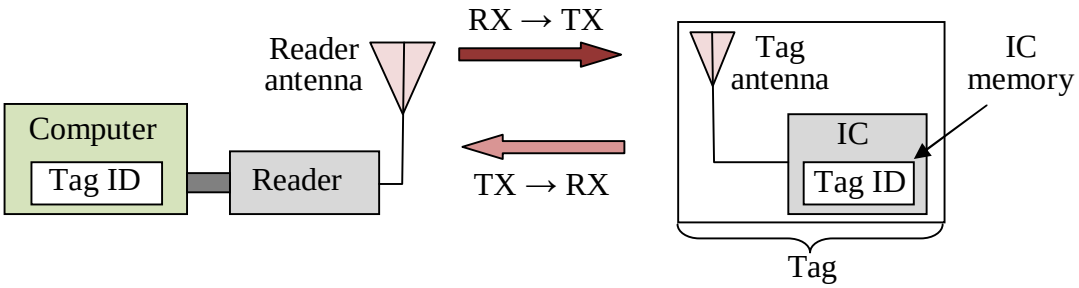

Fig. 2.9. UHF RFID system block diagram showing the basic components. Picture edited from [7].

An RFID reader is a radio transmitter and receiver. When a single antenna is used for both transmission and reception the reader is said to be monostatic. In such case, the receiving and transmitting ports need to be isolated. The main task of the reader is to wirelessly read and write data in the ASIC memory, and simultaneously convey enough energy to the passive or semi-passive tag. Additionally, the reader communicates with different application systems. The received backscattered signal from the tag is considerably smaller than the transmitted signal. The reader should therefore have good sensitivity to be able to correctly detect and demodulate the weak signal. However, for time being, the sensitivity of tags is typically poorer than for the reader, and therefore the read range is limited by the forward link. Today, the sensitivities of the IC and the reader are around -18 dBm and -80 dBm, respectively. [7]

The transmitted electromagnetic wave by the reader antenna at the operating frequency is a periodic signal with constant amplitude, frequency and phase. This so-called carrier wave carries no information other than the fact that it is present. In order to convey data, the signal must change. Therefore, the high-frequency carrier wave is modulated with a low-frequency baseband signal. Generally, RFID signals are digitally modulated where the signal power is kept large to indicate a binary 1 and small or zero to represent a binary 0. The binary data is coded prior to modulation, that is, the baseband signal changes between two stages according to a certain code. This is extremely important for passive tags that are dependent on the power obtained from the reader to run their circuits. If the carrier wave is only digitally modulated, the power level delivered to the tag is strongly data dependent since the tag will receive no power as long as the data remains 0. Data encoding ensures that the tag gets enough power even when the data being transmitted contains long strings of zeros. According to the telecommunication protocol ISO 18000-6c (EPC Class1 Gen2 UHF RFID) [11] passive UHF RFID systems shall use pulse-interval encoding (PIE) format. A binary 1 is coded as a short power-off pulse following a long full-power interval, and a binary 0 is codes as shorter full-power interval with the same power-off pulse. The resulting encoded baseband signal is then used to modulate the carrier wave, as depicted in Fig. 2.10. PIE using equal low and high pulses for binary 0 ensures that at least 50% of the maximum power is delivered to the tag even though the transmitted data contains long string of zeros.

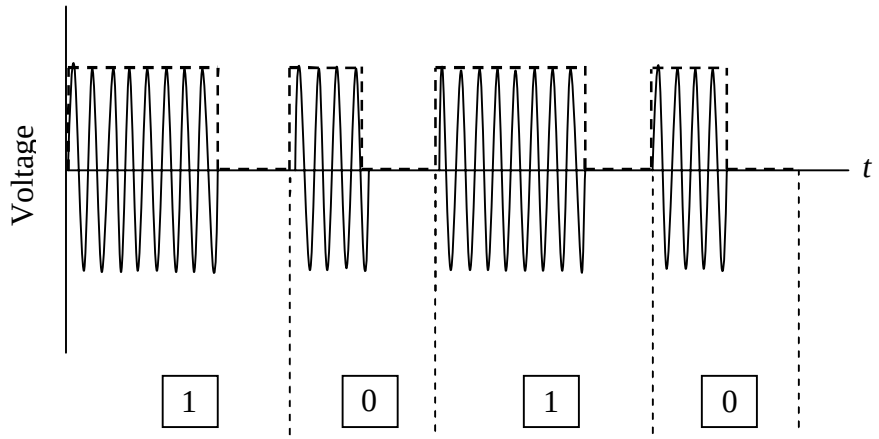

Fig. 2.10. Pulse-interval encoding of a carrier wave. The coded binary 0 ensures that the tag gets at least 50% of the maximum power even when the data consists of long strings of zeros. [7]

Modulation is the process of altering the signal parameters of a high-frequency carrier wave, that is, its amplitude, frequency or phase in relation to the baseband signal. The ISO 18000-6c protocol commands that the reader shall communicate using double-sideband amplitude shift keying (DSB-ASK), single-sideband amplitude shift keying (SSB-ASK), or phase-reverse amplitude shift keying (PR-ASK) as modulation technique. The reader used in this project communicates using DSB-ASK. In ASK the amplitude of the carrier oscillation is switched between two states according to the encoded baseband signal, so that the carrier wave envelope alters according to the amplitude of the baseband signal. The baseband signal is generally relatively low-frequency signal. If the data transfer would be realised at the baseband frequency, the consequence would be large-sized antennas. When the baseband signal is modulated in the carrier wave the frequency is increased to the desired UHF, which enables small-sized antenna implementation.

A commercial passive UHF RFID tag from Alien Technology is shown in Fig. 2.11. If direct chip attachment is not used, the tag IC may first be attached onto a strap, after which the strap is attached to the tag antenna.

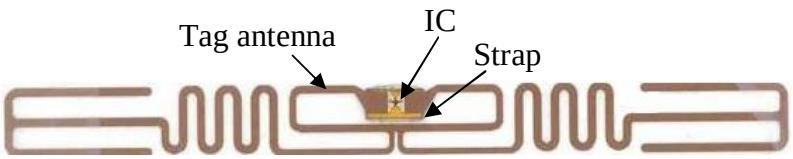

Fig. 2.11. A passive UHF RFID tag from Alien Technology (Model 9238 Squiggle).

The 96-bit long tag EPC is locates in the IC memory. Typically only the EPC is saved in the memory and all other relevant tag information is stored in external data system from where they can be read based on the EPC. To operate, the tag IC requires direct-current power (DC) of magnitude from one to three volts depending on the internal

circuit and is capable of supplying a few tens of microamperes of current [7]. This DC current is attained from the incoming carrier wave. The IC requires hence a rectifier circuit, which in the simplest form can be a diode whose output voltage is filtered using an RC-circuit. The rectified voltage is not enough to run the IC, but a charge pump used as a voltage multiplier is needed to higher the voltage up to the IC operating voltage. The carrier wave from the reader is ASK modulated, so the IC needs a demodulator to extract the data from the modulated carrier wave. The demodulator circuit is typically an envelope detector consisting of a diode connected in series with a small capacitor. [7] The tag IC operation is strongly non-linear due to its internal structure. As a consequence, the IC complex impedance is dependent on the input power and frequency. Hence, the matching between the tag antenna and the tag IC is only valid for a single point of operation [12]. The matching is usually established at the minimum power level required for the chip to operate properly [13]. It is later seen that this minimum power level maximises the read range.

Also the tag uses modulation and encoding schemes to convey information. The tag communicates with the reader using backscatter modulation, in which the tag switches the reflection coefficient of its antenna between two stages in accordance with the data being sent. According to the ISO 18000-6c protocol, the backscatter shall use ASK and/or phase shift modulation (PSK). In PSK the binary states zero and one are converted into corresponding phase states of the carrier wave in relation to a reference phase. The tag encodes the backscattered data as either FM0 baseband or Miller modulation of a subcarrier. In this project, the tags communicate using FM0 baseband encoding. In FM0 baseband encoding, the signal level changes to its inverted level at each binary symbol edge. Additionally, a binary zero changes signal level twice, whereas a binary one sustains the same signal level.

The operation of a passive UHF RFID system is shown in Fig. 2.12. Both the tag antenna impedance Z_A and tag IC impedance Z_{IC} is complex. The tag receives its operating energy from the modulated RF carrier wave transmitted by the reader antenna. The reader receives information from the tag by transmitting an un-modulated RF carrier wave and listening for a backscattered reply. The tag demodulator (in Fig. 2.12 shown as the series connection of a diode and a capacitor) interprets the received data. When the tag has obtained enough energy to run the tag IC, the induced voltage V at the antenna terminals is high enough and the tag sends data back during the reader's carrier wave transmission by switching its input impedance between two stages $Z_{IC,0}$ and $Z_{IC,1}$ according to the EPC. At each impedance stage, the RFID tag presents a certain radar cross section. Usually, one impedance stage is high and the other low to provide a significant difference in the backscattered signal. [13] This impedance difference is illustrated in Fig. 2.12 as a switch in the modulated reflection.

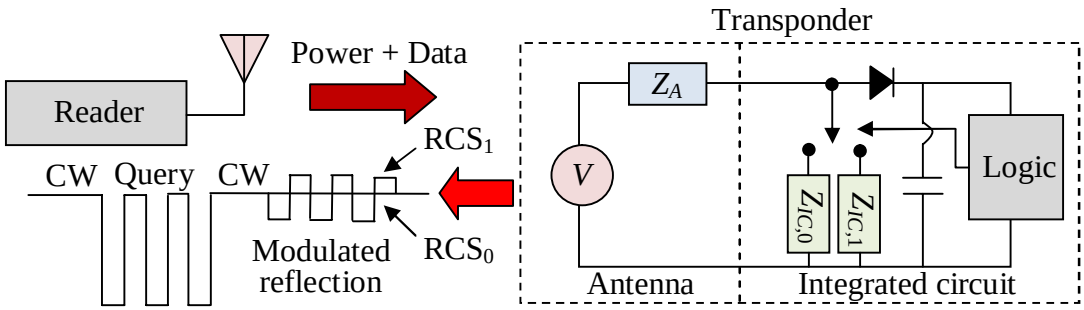

Fig. 2.12. Passive backscatter UHF RFID system. Picture edited from [13].

The two impedance states of the tag antenna are matched and mismatched. In the matched state the tag antenna is conjugated matched to the IC and the backscattered signal is weak. In the mismatched state almost all incident power to the tag antenna is backscattered back. Hence, the tag uses load modulation to modulate the backscattered signal to the reader. [7]

2.3.3 Impedance matching and power transfer

Since the transmitted power from the reader is limited and the IC sensitivity is finite, proper impedance matching between the tag antenna and the tag IC is crucial to maximise the power transfer to the IC. The received tag antenna power P_r estimated by Friis formula is only delivered to the tag IC when maximum power transfer occurs, that is, when the tag antenna impedance is conjugate-matched to the IC impedance. When perfect matching does not exist, the power delivered to the load is different than the power predicted by Friis. The ratio of the power delivered to the load to the load available power is defined as the power transfer coefficient [7]:

$$\tau = \frac{4R_A R_{IC}}{\left|Z_A + Z_{IC}\right|^2}, \qquad 0 \le \tau \le 1. \tag{2.64}$$

The quality of the impedance matching can be described by the power reflection coefficient:

$$\Gamma = 1 - \tau. \tag{2.65}$$

Ideally, all power is delivered to the IC ($\tau = 1$) and no power is reflected back ($\Gamma = 0$). In RFID systems also the polarisation mismatch between the tag antenna and the reader antenna reduces the available power transmitted from the reader. When a transmitted circularly polarised wave impinges on a linear tag antenna, only the component of the wave along the tag antenna axis has any effect. Hence, only one of the electric field components in the plane wave will interact with a linear tag antenna tilted at any angle within the plane perpendicular to the axis of propagation. Therefore, only half of the plane wave power can be received. When both the reader antenna and the tag antenna

are linearly polarised, the physical alignment error causes polarisation losses. These losses can be approximated as [7]:

$$L_{pol}\ (\text{dB}) = 20 \cdot \log(\cos\ \theta), \tag{2.66}$$

where θ is the angle between the transmitted plane wave and the tag antenna axis.

The electromagnetic research mainly concentrates the design of tag antennas having high efficiency and small size, together with conjugate matching. Several techniques for achieving conjugate impedance matching are found in publications. Most of the tag antennas operating at ultra-high frequencies are modified dipoles. The reactance of a short straight dipole is capacitive [4]. Also the load, the tag antenna IC, is inherently strongly capacitive. The aim is therefore to transfer the capacitive tag antenna input impedance into inductive with an appropriate, usually small, resistance required for the conjugate matching. Increasing the length of the dipole increases the input inductance. However, this technique usually results in far too large tag design. Folding techniques by bending the dipole arms are sometimes used to keep the tag size acceptable. Otherwise various kind of matching networks are utilised.

The T-matching network is the most commonly used matching network in tag antenna design. Fig. 2.13 shows the configuration and equivalent circuit of a typical dipole tag with T-matching geometry [14]. The tag antenna is composed of a dipole and a T-matching strip line. The T-matching circuit acts as a transformer that conjugate matches the antenna input impedance to the chip impedance through the parameter α.

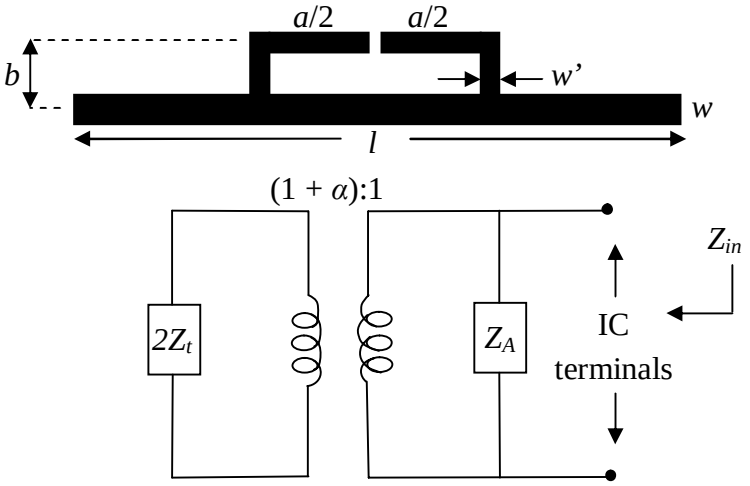

Fig. 2.13. Planar dipole T-matching configuration and equivalent circuit model. Picture taken from [14].

The tag IC is connected to a short-circuited stub of length $a \leq l$. The input impedance Z_{in} is given by [14]:

$$Z_{in} = \frac{2Z_t(1+\alpha)^2 Z_A}{2Z_t + (1+\alpha)^2 Z_A}, \tag{2.67}$$

where $Z_t = jZ_0\tan(ka/2)$ is the input impedance of the short-circuited stub, Z_0 is the characteristic impedance given by $Z_0 \cong 276\log_{10}\left(b/\sqrt{r_e r_e^{'}}\right)$, Z_A is the tag antenna input impedance without the T-matching connection, $r_e = 0.25w$ and $r_e^{'} = 8.25w^{'}$ are the equivalent radii of the dipole and the matching stub, and finally, $\alpha = \ln(b/r_e^{'})/\ln(b/r_e)$ is the current division factor between the two conductors. Now, the geometrical parameters a, b, $w^{'}$ and w can be adjusted to match the complex chip impedance. The T-matching network can also be embedded into the main radiator. Sometimes a single T-matching configuration is not completely adequate for conjugate matching. In such cases, multiple T-matching stages can be used [14].

3 BODY-CENTRIC COMMUNICATION

This Section provides a survey of body-centric communication applications and their features and challenges. The communication takes place within the sphere of personal area networks (PANs) and body area networks (BANs). The communication may be classified as off-body, on-body or in-body [15]. Off-body communication is established between body-worn and off-body located devices or systems. On-body communication takes place within on-body networks and wearable systems. In-body communication occurs between medical implants and body-worn sensor networks. Tags integrated into clothing could work as a body-centric RFID system. It could remotely monitor people's location or life parameters every time and everywhere [16]. Here, the focus is on off- and on-body communications. Implantable antennas have been suggested in [17−19]. These antennas face strict requirements and safety regulations and the designer should have in-deep knowledge about human anatomy and physiology and biological processes. Implantable antennas are out of scope in this project.

3.1 Features and challenges

A body-centric passive RFID system provides many interesting bio-engineering and healthcare application areas. Wireless monitoring of people by means of low-power and low-cost technology is nowadays considered as one of the most promising features of RFID techniques [20]. When the tag antenna comprises sensing and signal processing ability, the RFID system could provide real-time bio-monitoring for example of temperature, blood pressure, heartbeat, glucose content and human movement in hospitals [21]. Already now, it has theoretically been demonstrated that the RFID monitoring of legs in sleep diseases is feasible [22]. It is believed that in the near future the integration will concentrate on separate labels sewn onto a ready garment. Eventually, however, the integration of electronics will take place already during the sewing process [23]. This new technology will provide multifunctional daily garments integrated with wearable antennas, sensors and power harvesting devices to enable on-body wireless communication [24]. Such a garment is illustrated in Fig. 3.1.

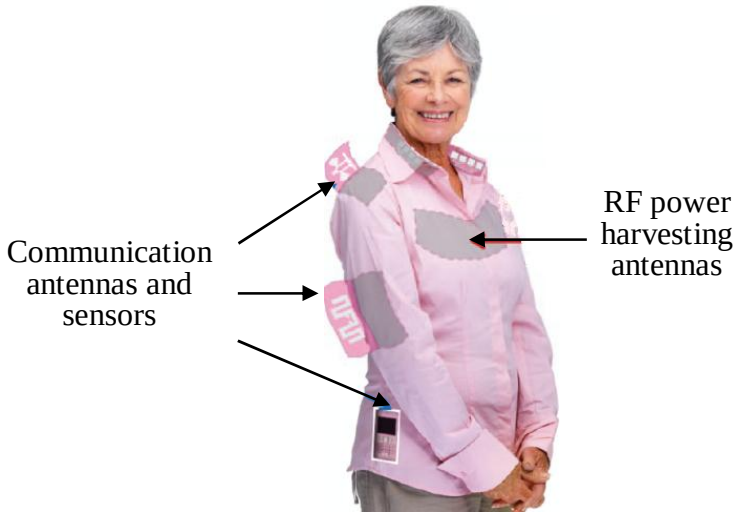

Fig. 3.1. Multifunctional intelligent shirt comprising wearable antennas and sensors for body-centric communication envisaged in [24].

Application areas for off-body communication take typically place in restricted areas using fixed readers, or wearable readers and disseminated tags in the surrounding. The on-body communication is, however, needed when a fixed communication infrastructure is missing [16]. Examples of such cases are military [25] and fire-fighter [26] applications.

The wearable tag antenna together with the IC sensitivity determine many of the passive RFID system key performance parameters, such as the read range and the compatibility with the used application environment. The tag environment is challenging due to the presence of the human body with its high permittivity and losses. This calls for wearable antennas that are low-cost, conformal, reliable, light-weight, maintenance-free, integratable, and have stable performance independent of the unpredictable antenna-to-body spacing.

The electrical properties for some human body tissues taken from database [27] are collected in Table 3.1. At higher frequencies the tissues become more lossy and their relative permittivity higher. At UHF, it is reasonable to assume that the effective electrical properties of for example a limb are determined by the interaction between the limb tissues. Superficial and bigger tissues will probably be more prominent, as well as tissues having high relative permittivity and loss tangent values. Clearly, the complex structure of the human body makes it challenging to exactly define how the body is electrically acting.

Table 3.1. Some human body tissue electrical properties taken from [27].

Electrical properties for 800–1000 MHz						
Tissue	Skin	Fat	Muscle	Bone	Blood	Body fluid
ε_r	40.9–42.0	5.4–5.5	54.8–55.3	20.6–21.0	61.1–61.7	68.9
tan δ	0.40–0.45	0.18–0.20	0.32–0.37	0.32–0.34	0.47–0.54	0.44–0.52

The presence of the high permittivity body shifts the resonant frequency towards lower frequencies. The detuning effect is more prominent if no tag-to-body isolation is used. The quality factor (*Q*-factor) describes the antenna as a resonator and is representative of the antenna losses, including radiation, conduction, and dielectric and surface wave losses [4]. The three latter are typically small for small antennas having good conductors, and therefore, small antennas usually exhibit large *Q*-factors. The *Q*-factor is interrelated with both bandwidth and efficiency, and there is always a trade-off between the quantities [4]. The bandwidth for small antennas is hence narrow, making the detuning especially harmful.

Further, the lossy body will induce strong power absorption and alter the radiation pattern dramatically with respect to free-space. Therefore, wearable antenna research has been focused on two- or multi-layered patch-like antennas with a ground plane to isolate the antenna from the body. A substrate thickness of at least 2 mm is advisable in order to design an antenna with sufficiently high radiation efficiency [26].

The antenna loss resistance increase while the radiation resistance decrease near the human body. Experiments show that the decrease in resistance and reactance may be a high as 50% [28]. Theoretically, the input impedance is affected only by objects in the reactive near-field of the antenna [29]. Patch-type antennas concentrate their reactive fields in a tight gap between the patch element and the ground plane, keeping the user to some extend from disturbing it. Dipole antennas on the other hand, spread their near-field more and consequently, the user will disturb it more. Another issue is the mutual capacitance between the antenna and body that tend to store energy and cancel out the wanted input inductance [23].

Sometimes also electromagnetic band-gap (EBG) structures have been utilised to prevent the body from affecting the antenna. These consist of periodic structures that prevent the propagation of electromagnetic wave in a specific frequency band. They provide improvement of antenna efficiency, reduction of side lobe levels and increase in antenna gain by reducing the patch surface wave propagation that causes losses [30].

In [21] a planar tag antenna geometry fed via a nested slot is presented. To electrically isolate the antenna from the skin, and to permit bio-compatibility, a lossless 4-mm thick silicone slab with permittivity of ε_r = 11.9 is utilised. The computed antenna gain on-body range from -8.5 dBi to -6.9 dBi.

In [31] a tag antenna is designed for both remote human monitoring and metallic cylinder tracking. Robust platform tolerance is established using a microstrip-type structure where the patches are shorted to the ground plane. The tag is implemented on 0.4-mm thick FR4 substrate reinforced by a 1.4-mm thick foam layer to guarantee sufficient bandwidth and radiation efficiency. The tag provides a 3.5-m maximum boresight read range when worn on torso on top of a shirt. On metallic cylinder a maximum boresight read range of 4 metres is attained.

A patch-type tag antenna for identification of sportsmen in mass races is designed in [32]. Substantial impedance detuning, poor efficiency and heavy-weight are prevented by using a 4.8-mm thick foam dielectric with permittivity of ε_r = 1.29.

Despite of a 165 x 74 mm^2-sized ground plane metallisation, the antenna weight is 20 g. The large size does not necessary represent a major problem, since the tag may be integrated into a racer number label. Compared to an original shorted dipole-type antenna, the computed gain of the patch antenna is more than 10 dB higher. In real-life applications, the foam might be subjected to compression or bending. Of course, these possible issues should be taken into consideration early in the antenna design process.

Suggested single-layer antennas are typically combined with reflector or slab. In [33] the reflector in a wristband is used to reduce the power absorbed by the body. A 5-dB improvement in tag antenna gain is reported. Even though single-layered antennas without shielding ground plane are often associated with disbelief, they have many advantages compared to two-layered structures. The manufacturing process is faster and easier as well as the possible integration into garments. Patch-type structures demand a constant thickness for proper operation, which typically call for stiffer cloth substrate. This in turn restricts the flexibility and comfort. This is not the case for single-layered antennas. In fact, single layered antennas need to be worn at a certain minimum distance from the body, but this separation need not to be constant [28−29]. Additionally, a tag-to-body separation of $\lambda/(2\pi)$ is sufficient to attain 75% radiation efficiency compared to free-space radiation efficiency [29]. A single-layer wearable meandered dipole tag antenna is presented in [28]. Even though the tag does not have a ground plane, it provides 5 to 7 metres read range at 866 MHz if it is worn at 10 mm or more from the upper arm. At 30 mm separation the operation of the tag resembles that of free-space. The suggested tag antenna of 70 x 20 mm^2 size can be integrated on any normal clothing fabric with permittivity value between 1 and 1.5.

Truly wearable antennas should only consist of textile substrate materials, conductive threads or electro-textiles, and if the application demands, flexible silicone or plastic slabs and coatings [23]. Commercially available conductive threads and electro-textile have sufficient high conductivity to provide acceptable antenna performance [24, 26, 34−38]. Electro-textiles have also successfully been used as antenna ground plane [26]. Further research work is needed to determine the effects of washing temperature and moisture, which limit the life time of the antenna. Polymer coatings or waterproof laminates are believed to protect the antenna and possible IC without affecting their electrical properties [23, 28].

The complex and asymmetric structure of the human body call for careful selection of antenna position in order to minimise shadowing and excessive body power absorption [39]. In [23] it is reported that depending on the tag position on body, a ±2 dB variation in the realised gain is expected. Attached to a human body, any antenna has a radiation pattern similar to that of a patch-antenna [29]. A single antenna is not enough to establish omnidirectional off-body link because at the UHF frequencies the body cannot be penetrated [29, 39]. The shadowing effect is strong although the amount of tissue is small behind the antenna [29]. Since the tag antenna will be worn on a moving person, there is also risk for polarisation mismatch losses. In [26] it is suggested

that circularly polarised antennas should be preferred instead of linearly polarised antennas in order to optimise the off-body communication link.

3.2 Simulations and measurements of off-body communication

The effect of human body on antenna performance has been assessed by means of simulation tools. The human body simulation models utilise electrical tissue parameters measured from human or animal tissue samples. Such parameters are available for example in [27]. Several human body models have been developed with varying level of detail. However, they all model the body in stationary state and typically only part of the body is modelled.

Measurements are usually conducted using volunteer subjects. The major advantage using this approach is that the tissue properties and proportions are correct, that is, the measurements are conducted in real application configurations. However, these tissue properties are unknown because they will most probably differ from the values found in various tissue databases. Another drawback is the measurement repeatability. It is extremely difficult to repeat the same body posture twice. Moreover, involuntary body movement due to breathing introduces inaccuracy in the measurement results, as well as an unpredictable air layer between the body and the antenna. Nevertheless, an antenna should be designed to count for all these inaccuracies.

Alternatively, measurements are conducted using phantom models filled with tissue-equivalent liquids. These liquids consist typically of a solution of sugar and salt in water. The sugar is used to lower the permittivity of water while salt is used to increase the losses in order to make a liquid that represents the average of all the tissues considered. The liquids in simple phantoms used in laboratory research work are almost always homogenous and single tissue layers cannot therefore be represented. Of course, one phantom can only represent one body shape and posture, but the measurements are significant easier to conduct compared to measurements conducted on a volunteer subject. The phantoms are usually of simple shape and represents only part of the whole body. The antenna allows to be well attached to the typically flat phantom, which eliminates the unpredictable air layer that tends to be present whenever the surface is not totally flat. When shadowing effects or accurate radiation patterns are desired, the phantom should be in correct size and all body parts should be included.

Obviously, measurements conducted on body or phantom includes major uncertainty sources that easily introduce disagreements between simulation and measurement results. However, when measurements are carefully conducted and simulation models with high enough accuracy are used, good agreement can be achieved. It should be noted that all applications do not require perfect agreement, but tolerate deviations to a certain extent.

In [21] a stratified elliptical cylinder model for the human thorax is utilised to design bio-compatible tag antennas for the UHF. Two different torso sizes are

investigated. Physical and electrical parameters are obtained from tissue database. The same model and parameters are used in a similar torso model in [31]. The validation of the power transmission coefficient for the tag antenna on body in [21] is estimated using a phantom consisting of a cubic box made of Perspex with permittivity and conductivity of 2.1 and 0 S/m, respectively. Due to the presence of the insulating Perspex layer, the silicon slab used in the simulation model is not required to isolate the antenna from the liquid, even though the slab electrical properties (ε_r = 11.9 and σ = 0 S/m) differ from the properties of the Perspex layer. The simulation model and measurement set-up are illustrated in Fig. 3.2.

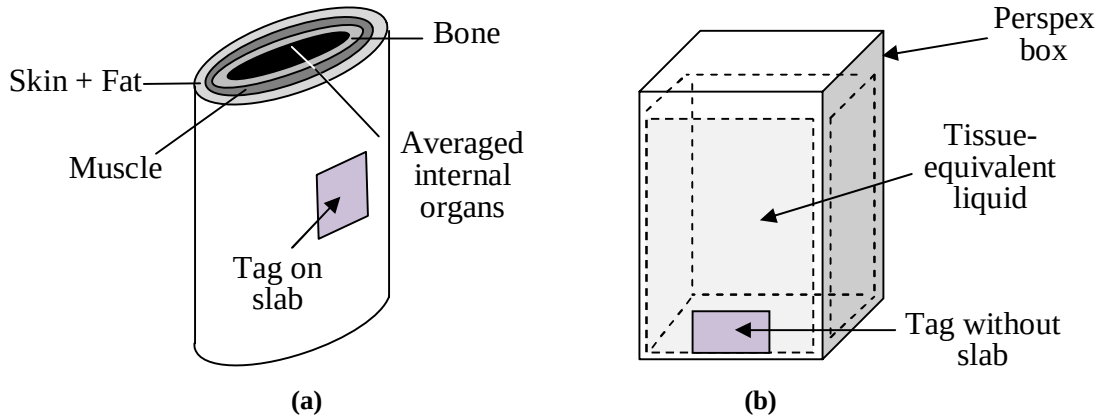

Fig. 3.2. **(a)** 4-layer elliptical cylinder used for representing the human torso in [21] and [31]. Tissue parameters attained from database. **(b)** Practical measurements conducted in [21] using 20^3 cm^3 liquid phantom with de-ionised water with saccharose and sodium chloride. It is stated that the solution concentration can be varied to represent trunk or even a human head.

When the liquid phantom contains muscle-like parameters of ε_r = 54.5 ± 5% and σ = 0.9 ± 5% S/m, close agreement in transmission coefficient between simulated model and measured tag on phantom is attained. Even when the solution concentration is changed, the agreement is good. The authors in [31] have chosen to conduct the impedance measurements on a volunteer subject using a balun approach according to Fig. 3.3. The measurements are conducted on the shirt, even though the simulation set-up in Fig. 3.2 does not include any clothing layers. However, agreements between measured and simulated results are found.

Fig. 3.3. Practical measurements of the tag antenna on human torso in [31].

In [25] the whole human body is simulated using a FEKO simulator homogeneous model with the permittivity value of 56 and conductivity of 0.94 S/m at 225–450 MHz. The selection of these values is not further explained. On phantom of unknown dimensions and composition an antenna realised gain of at least -10 dBi over the whole frequency band is achieved. In [34] a portion of a homogenous arm is considered with a permittivity value of 45.6 and loss tangent of 0.23 at 2.45 GHz. These values are assumed to represent human arm consisting of 85% muscle and 15% fat. Measurements are conducted on the human arm on top of clothing. A difference of several dB is noted between the simulated and measured S11.

In some applications it is enough to use a coarse human model. One application could be the selection of type of wearable antenna. In such case it is not interesting to simulate exact results for each antenna, but rather the difference in performance. In [40] the human is modelled as a box with the dimensions 300 x 300 x 51.5 mm^3 using three different layers, as depicted in Fig. 3.4. The electrical parameters for each layer are not mentioned.

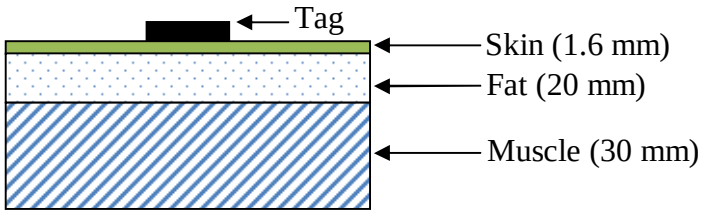

Fig. 3.4. Cross-section of simplified human model utilised in [40].

The above-mentioned human models estimate the antenna performance directly on the body. This is most probably not the set-up in the real application. Wearable antennas tend to be worn on either on top of clothing or integrated into it. In [26] the actual application in which the antenna is integrated into a sleeve worn on a human arm is simulated. As seen from Fig. 3.5, the model even includes a 0.5-mm thick ventilation layer because the sleeve does not fit tightly on the arm. The arm is modelled as a homogenous cylinder with permittivity of 42 and conductivity of 0.99 S/m. The value selection is not motivated.

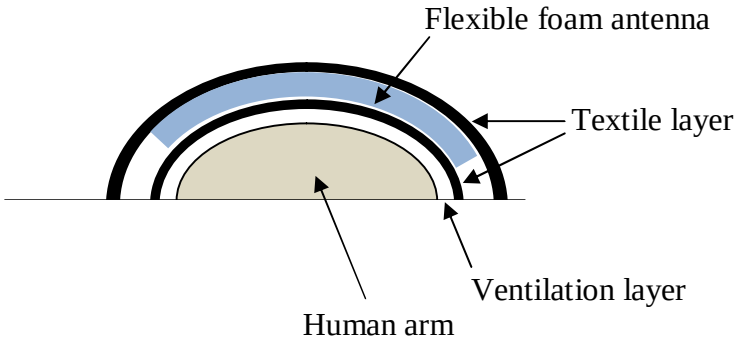

Fig. 3.5. Simulation model for antenna implemented in a worn sleeve on human arm utilised in [26].

The two 0.4-mm thick textile layers represent the inner lining of the sleeve and outer garment layer. The permittivity and loss tangent for these layers are 1.85 and 0.015, respectively. The flexible foam antenna includes the electro-textile ground plane and patch, and the foam substrate. Measurement and simulation results differ, but are assumed to be satisfactory.

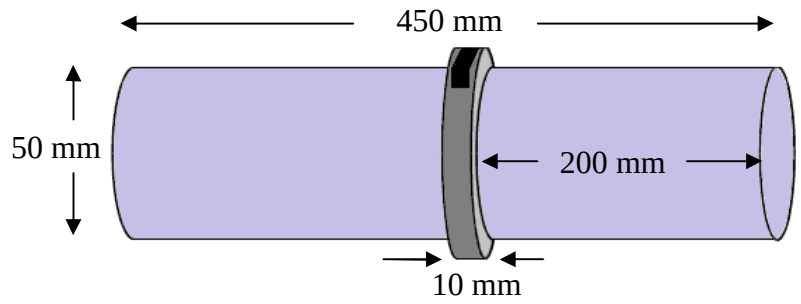

Fig. 3.6. Wristband with embedded dipole antenna and a reflector located at the inner lining of the wristband simulated on a homogenous human wrist model in [33].

In [33] a 3-mm thick silicon wristband with embedded folded dipole antenna and reflector is simulated on a human wrist model as shown in Fig. 3.6. The wrist is assumed to consist of 60% muscle with the permittivity and conductivity values of approximately 35 and 1.1 S/m, respectively. Measured and simulated S11 show a difference of 2.6 dB.

3.3 Materials and fabrication of wearable antennas

Several different materials for wearable antennas have been suggested in earlier research work. Substrate materials providing light-weight and flexibility are preferred. Typically, the substrate consists of fabrics [24, 28, 34, 36, 39], foam [26, 31], or polydimethylsiloxane (PDMS) [41−42]. The antenna conductor and possible ground plane include metals or metallic composites. Copper is typically used at the conductive antenna element due to its low loss and superior conductivity. However, in wearable applications, the lack of structural flexibility prevents it from effectively conform to the surface. Therefore, several so-called electro-textile technologies for wearable antenna applications have been suggested. Electro-textiles are conductive fabrics that are constructed by interpolating metal or polymer threads with conventional fabric thread or conductive threads [43]. These are believed to be a strong candidate for body-worn electronics thanks to their washability, durability and flexibility [43]. The construction of electro-textiles is illustrated in Fig. 3.7.

Conductive fibres can be fabricated by three different methods [43]: (1) by filling the fibres with carbon or metal particles, (2) by coating the fibres with conductive polymers or metal, or (3) by using fibres that are completely made of conductive material. Conductive threads are created from single or multiple strands of conductive and non-conductive fibres. Typically, the strand threads are multi-filament, formed by

twisting many thin fibres together. The strong non-conductive fibres can protect the thin fragile conductive fibres from external tension, providing thus mechanical robustness without removing the electrical functionality [43]. Most threads are metallised with an alloy of various metals, including silver, copper, tin and nickel. The core is normally cotton or polyester.

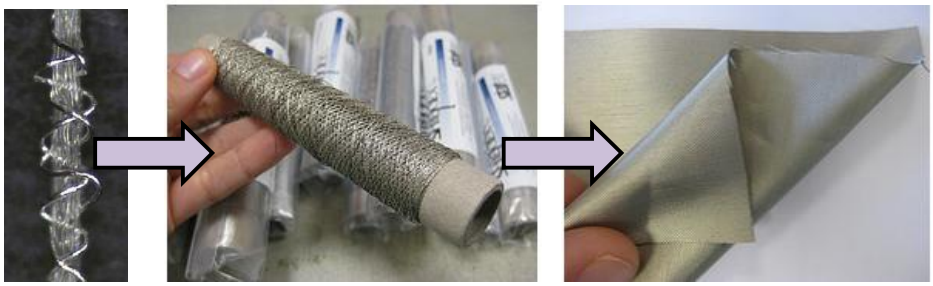

(a) **(b)** **(c)**

Fig. 3.7. Electro-textile construction, **(a)** Conductive sewing thread created from single or multiple strands of conductive and non-conductive fibres [43], **(b)** Conductive sewing thread for sewing, picture taken from www.kobakant.at/, **(c)** Conductive fabric ready to use for wearable antenna applications, picture taken from www.kobakant.at/.

Conductive fabrics are generally created by adding conductive threads into fabrics by means of weaving or knitting [43]. In knitted fabrics, the conductive threads create interlocking loops, while in woven the threads are straight in two orthogonal directions. Commercially conductive threads and fabrics are available from for example Shieldex and LessEMF. It is also possible to create a conductive fabric using an embroidery or sewing machine with conductive thread. The electrical properties of self-sewed conductive fabric are more challenging to define since the sewing pattern and density plays an important role in determining the properties [44]. Commercial fabrics are often homogenous and the electrical properties are provided within limited accuracy. However, the use of embroidery or sewing machine enables control over the sewing pattern and density, amount of material and most importantly, when the electrical properties are defined, control over the antenna performance parameters.

A simple and versatile laboratory-fabrication method of embroidered tag antennas is demonstrated in [45]. Free-space measurements of fully assembled embroidered tag verify that competitive tag performance is achieved with the presented fabrication method. In [46], the practical on-body read range of this embroidered tag is measured in real environment. A boresight peak read range of 1.30 metres is recorded.

The tag antenna is sewed on fabric substrate with conductive threads using Designer Rugby embroidery machine by Husqvarna. The machine requires both upper and bobbin thread. As demonstrated in [44] and [45], the conductive tag antenna pattern can be established using either conductive and conventional non-conductive sewing thread, or only conductive sewing thread.

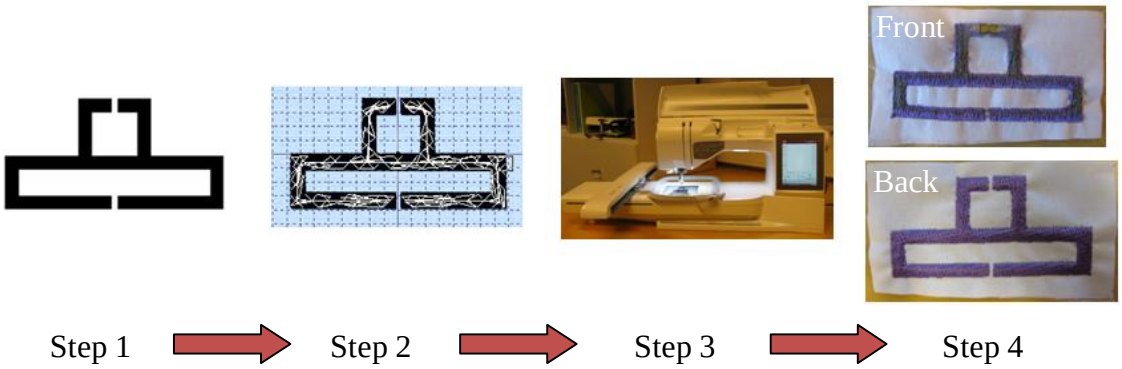

Fig. 3.8. The fabrication process of embroidered tags. The process starts with a .tiff-file exported from a conventional simulator and ends with an embroidered pattern according to the selected stitch pattern in step 2. The tag IC is attached using conductive epoxy.

The tag antenna is designed using any conventional simulator and exported as a .tiff-file to 5D™ Embroidery System software (step 1). The software allows modification of the sewing pattern, for example the stitch pattern and density (step 2). The Design Creator module transforms the ready .tiff-file to an embroidery file compatible with the embroidery machine (step 3). The machine creates the tag antenna pattern according to the selected stitch pattern automatically (step 4). The ready tag antenna will have conductive pattern on both sides of the substrate as shown in Fig. 3.8.

In [42] a conformal and light-weight antenna technology based on electro-textiles and polymer-ceramic composites is suggested. The electro-textiles are coated with carbon nanotubes and sputtered with silver particles for improved conductivity. The fabrication process of printing a planar electro-textile antenna on a polymer-ceramic composite is shown in Fig. 3.9.

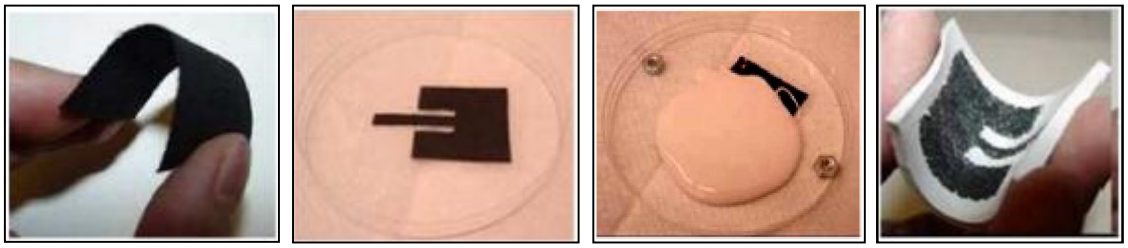

Fig. 3.9. Antenna technology based on electro-textile conductors printed on polymer-ceramic composite in [42]. **(a)** Electro-textile coated with carbon nanotubes and silver particles using dyeing and sputtering technique, respectively, resulting in a 2-Ω textile, **(b)** Electro-textile cut according to the patch antenna dimensions, **(c)** Electro-textile embedded on a polymer composite, **(d)** Ready antenna after curing. The electro-textile adheres strongly to the polymer-ceramic composite.

The electro-textile antenna exhibits a 6-dBi gain at 2 GHz, which is only 2 dB lower compared to a simulated ideal PEC patch. The resistance of the electro-textile patch plays a critical role for the achieved antenna gain. When the resistance is increased to 10 Ω, the gain drops to 0 dBi at 2 GHz.

3.4 Motivation of this project

The design process of wearable antennas demands proper modelling of the application environment, the human body, to efficiently optimise the UHF RFID tag antenna performance. In contrary to previous models, here the human body is not modelled by utilising available tissue databases. Instead, a novel method of using both practical on-body measurements on volunteer subject and simulations is demonstrated. The on-body measurements provide the true tag response on body, while the simulations provide a modelling tool to create a human body model that provides the same tag response as the true measured response. The complex and complicated structure of the human body makes it impossible to model it in detail in an RF point of view. As in many engineering fields, simplification is necessary to concentrate only on the essential things. Therefore, the human body is considered as a "black box", whose content cannot be seen. However, the response of this box can be measured. The received response can effectively be used to create a model providing the very same response as the black box. This methodology of simplification is illustrated in Fig. 3.10.

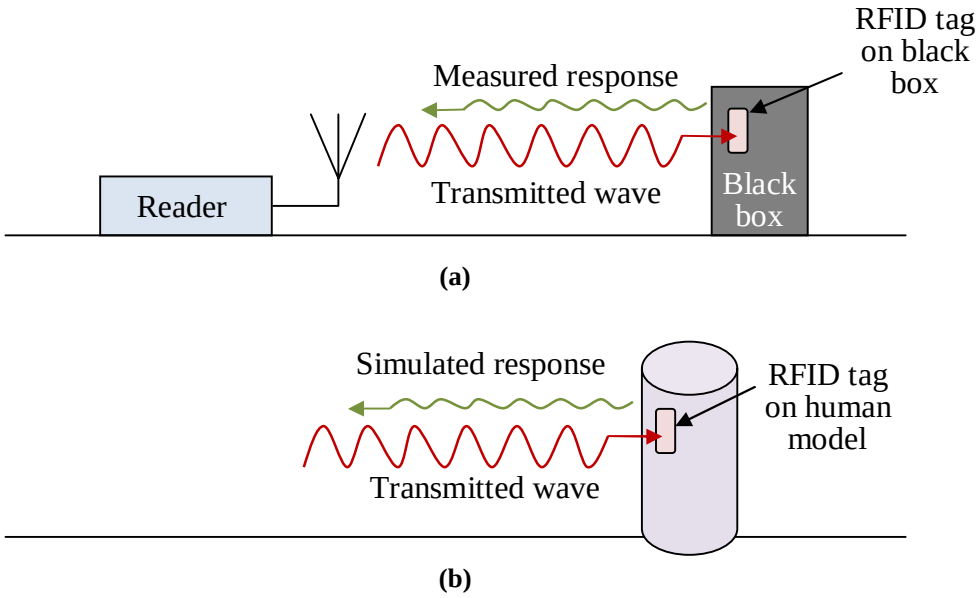

Fig. 3.10. The human body model is developed using practical on-body measurements and simulations. **(a)** The tag is measured on-body, which is considered as a black box. The received tag response includes the true effects of the environment. **(b)** The measured response from the black box is used to create a simulation model on which the tag provides the same response as on the black box.

Unlike in previous publications, the measurements are wirelessly conducted in the far-field. This removes the need for baluns or fixtures required for near-field measurements.

The response from on-body measurements includes not only the effect of high permittivity and lossy tissues, but also the effects of tag attachment, air between the tag and body, uneven body surface and shadowing. Such effects are easily weakened, or even removed, when too small and simplified phantoms are used. When the human model is developed based on the true on-body tag response, the model will include all the effects on tag performance caused by the real application environment.

4 DEVELOPMENT OF THE HUMAN ARM SIMULATION MODEL

The research method is covered in this Section. Necessary background theory is provided in Section 2. Section 3 summarised previous research on this topic. Here, a novel approach is presented to develop a simple human body model for wearable passive UHF RFID tag applications. The method is based on both simulations and practical measurements. It is shown that a model for 800–1000 MHz with ±2 dB accuracy is achievable.

4.1 The effective human arm model

As discussed in the previous Section, there are different approaches one can use to model the human body for wearable UHF RFID tag antenna applications. Instead of using a layered simulation model, a homogenous model of simple geometrical shape is chosen here. This way the precise knowledge about tissue parameters and their frequency dependence becomes less critical. Additionally, the unawareness of the tissue layer thicknesses can be avoided. In fact, it is less interesting to know the exact composition of the human body since it will vary from person to person. What is important is how the human body is seen electrically to the attached tag antenna. The tag antenna does not see the single tissues, but rather the effective human body. The electrical properties of such an effective human body are averages of all the single tissue electrical properties. When measurements are conducted with the wearable tag attached to a volunteer subject, which is the case here, it is the effective human body that is measured, not the electrical properties of single tissue layers. It is therefore convenient to have a model that is actually measured. Additionally, a detailed layered model would require more computation time compared to the simple effective model.

It is highly desirable to have a wearable tag that is able to provide acceptable performance characteristics independent of the tag location on body. However, this is extremely difficult to achieve. The tissue parameters change dramatically on different body locations and the tag might be shadowed by body parts. Many body locations are not flat, or are exposed to significant displacement during body movements. It is obviously important to select the wearable tag position carefully. Here the upper arm is chosen as the tag location. This location has appeared to be suitable [28, 46]. The location assures no shadowing of the tag during normal user movement and hence, the possible polarisation mismatch loss between the tag antenna and the reader antenna is minimised.

Many earlier publications show measurements of wearable tags attach to clothing [31, 34, 41]. The measurement results show therefore in addition to the body effects also the effects on tag performance resulted from the used clothing. That is, the measurements show the effects of an effective human body including the clothing and possible air gaps between the body and the clothing. It is therefore difficult, unless impossible, to separate the effects on tag performance resulted from the human body and the effects resulted from the clothing. To measure only the body effects on tag performance it is better to remove any additional layer that separates the tag from the body. In this project, all on-body measurements are conducted directly on body, that is, the tag is attached directly to the skin.

The electrical properties of the homogenous model are found through simulations and measurements. The tag performance characteristic that is simulated and measured is the realised gain. It is chosen based on several reasons: (a) it is not dependent on the transmitted power from the reader antenna, (b) it can be measured wirelessly, and (c) it is notably degraded near the human body. Performance degradation on the body is desired since the degradation compared to free-space comprises information about the body effects. The simulation model is characterised by the electrical parameters effective relative permittivity, $\varepsilon_{r,eff}$, and the loss tangent, tan δ. A tag antenna realised gain is measured on-body on the upper arm. The same tag antenna is simulated on the homogenous model. By adjusting the model electrical parameters properly, agreements between measurement and simulation results can be found.

4.1.1 Tag antenna for model testing

The measured tag antenna on body is a dipole. Wearable tags of dipole-type have been successfully measured on body [28, 29]. They are one-layered and low-profiled, which enables easy integration into clothing.

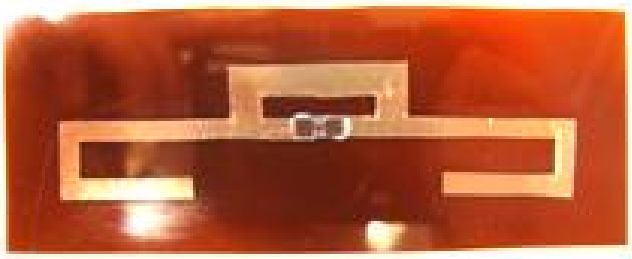

Fig. 4.1. The folded dipole copper tag on kapton substrate for on-body measurements. The tag is manufactured by hand using copper tape. The strap with the NXP tag IC is attached using conductive epoxy. The handmade fabrication is estimated to result in ±0.5-mm dimension accuracy.

The measured tag electrical parameters, or the tag performance, should be well-known in order to prevent errors in the human model parameters. With other words, the tag simulation model is assumed to predict the measured free-space tag performance perfectly. Therefore, the tag antenna conductor is chosen to copper and the substrate to kapton polyimide film. The electrical properties of kapton are sensitive to humidity, but

since all measurements are conducted in dry condition this can be discounted. It should be noted that this copper tag is not a tag antenna that fulfils the criteria for wearable antennas. However, the precise knowledge of its performance together with the relatively flexible kapton substrate makes it a suitable candidate for on-body measurements to extract the electrical parameters for the human model. The copper tag is shown in Fig. 4.1.

4.1.2 Tag integrated circuit equivalent circuit model

The NXP tag IC on strap is attached over a 2 mm gap *d*. The equivalent circuit model [47] consists of an RC parallel circuit, as depicted in Fig. 4.2, with the values $R_{eq,nxp}$ = 2.85 kΩ and $C_{eq,nxp}$ = 0.91 pF. The equivalent circuit is valid over the frequency range 800–1000 MHz and is associated with a 2 mm x 3 mm sized port simulation model. The NXP datasheet states that the IC sensitivity is typically -18 dBm.

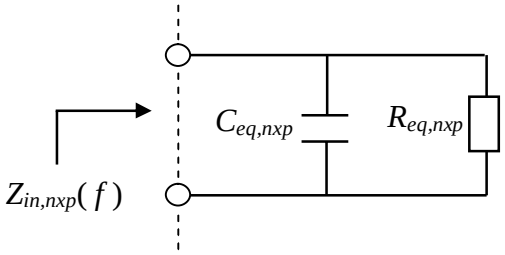

Fig. 4.2. Equivalent circuit model for the NXP tag IC on strap over a 2 mm gap. The model, or rather the equivalent component values, hold information about the chip and strap with conductive epoxy at tag IC threshold power [47].

The input impedance $Z_{in,nxp}(f)$ of the equivalent circuit model can be written as:

$$Z_{in,nxp}(f) = \frac{Z_{Ceq,nxp} Z_{Req,nxp}}{Z_{Ceq,nxp} + Z_{Req,nxp}} = \left(\frac{R_{eq,nxp} + j\left(-2\pi f C_{eq,nxp} R_{eq,nxp}^2\right)}{1 + \left(2\pi f C_{eq,nxp} R_{eq,nxp}\right)^2} \right). \tag{4.1}$$

The tag IC nominal input impedance depends on the applied antenna voltage, and therefore on tag IC input power, in a strongly non-linear way [12]. The non-linear behaviour is caused by the internal structure of the tag IC [12]. The values $R_{eq,nxp}$ and $C_{eq,nxp}$ are attained through measurements conducted at tag IC threshold power. The threshold power, or the sensitivity, is defined as the minimum tag IC power required to activate the tag IC. The measurements are also conducted at tag IC threshold power. Hence, the IC non-linear behaviour is not causing any problems and can be neglected.

4.1.3 Simulations

The effective human arm simulation model is created in the Ansoft's High Frequency Structure Simulator (HFSS). It is a numerical solver for electromagnetic wave equations based on the finite element technique. The used material parameters for the copper tag on kapton are collected in Table. 4.1.

Table 4.1. Copper tag material electrical parameters used in the simulations.

Material	Conductivity σ (MS/m)	Dielectric loss tangent δ	Thickness t (mm)	Relative permittivity ε_r
Air	0	0	-	1
Copper tape	58	-	0.045	1
Kapton HN	-	0.0026	0.126	3.5

The initial task is to design the copper tag antenna on kapton for model testing in free-space. Since the tag is measured directly on body, the tag should be designed in free-space in such a manner that it is still responding on the body even though severe performance degradation is encountered. This call for the following tag specifications: (1) relatively high resonance frequency of about 950 MHz to give room for a frequency shift towards lower frequencies on body, (2) as good impedance matching as possible to provide a reasonable realised gain on body, (3) a tag size that can be fitted on the upper arm.

The length, width and IC gap of the tag antenna are set to l = 90 mm, w = 3 mm and d = 2 mm, respectively. Due to the internal structure of the tag antenna IC, its input impedance is inherently strongly capacitive, which can be seen from Eq. (4.1). In order to achieve conjugate matching it is therefore necessary to add a matching network between the IC and the tag antenna. The T-matching network dimensions l_2, w_2 and h_2 are adjusted to provide the required inductance. The dipole is folded to increase the length of the radiating element in order to tune the resonance frequency. The height is set to h = 13 mm and the length l_3 is increased until a resonance frequency at 950 MHz is achieved. The copper tag on kapton simulation model and dimensions are presented in Fig. 4.3. The in free-space simulated and measured forward read range and realised gain are shown in Figs. 4.8 and 4.9.

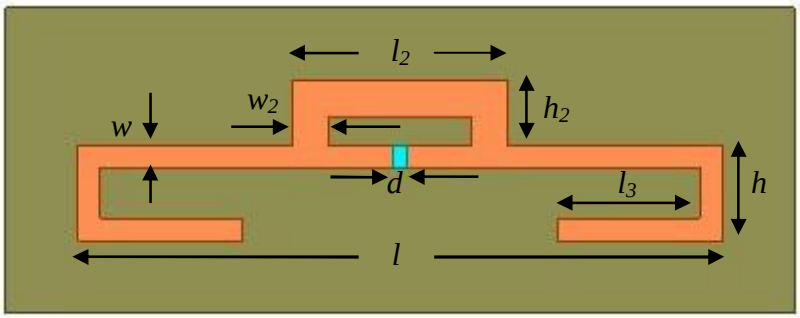

Fig. 4.3. The overall footprint of the copper tag on kapton is 110 x 42 mm^2. The tag dimensions in mm are: l = 90, l_2 = 30, l_3 = 20, w = 3, w_2 = 5, h = 13, and h_2 = 9. The chip marked with blue is 2 x 3mm^2 in size.

The second task is to simulate the free-space optimised copper tag on the effective human arm model. The realised gain is chosen as the studied tag antenna parameter. This parameter shows clearly the quality of the tag performance. Instead of modelling the whole human body, only the upper arm is modelled. The effective human arm

simulation model will hold information about the effects resulted from the rest of the body.

The upper arm is modelled as a homogenous cylinder with the electrical parameters $\varepsilon_{r,eff}$ and tan δ. The cylinder diameter d_c and length l_c are set to 10 cm and 20 cm, respectively, which corresponds to the arm size of a normal weight person. The cylinder is composed of 100 segments to keep the computation time reasonable. The upper arm is of course not a perfect cylinder, and hence it is inconvenient to model the arm with too many segments.

The simulations are conducted for two different cases: in case 1 the copper tag is simulated on the human arm model with the substrate against the skin, whereas in case 2 the tag antenna conductor is facing the skin. As demonstrated in [48], greater tag performance degradation is expected in case 2 due to the strong interaction between tag antenna conductor and the body. In case 1 the substrate is providing tag-to-body isolation.

The simulation set-ups for the two different cases are depicted in Fig. 4.4. In case 1 the tag is directly simulated on the arm model. In case 2 the arm model is immersed in an air cylinder to enable wrapping of the substrate in HFSS. As the figure shows, the simulation model is cut in the symmetry plane to reduce the simulation problem to half to reduce the computation time.

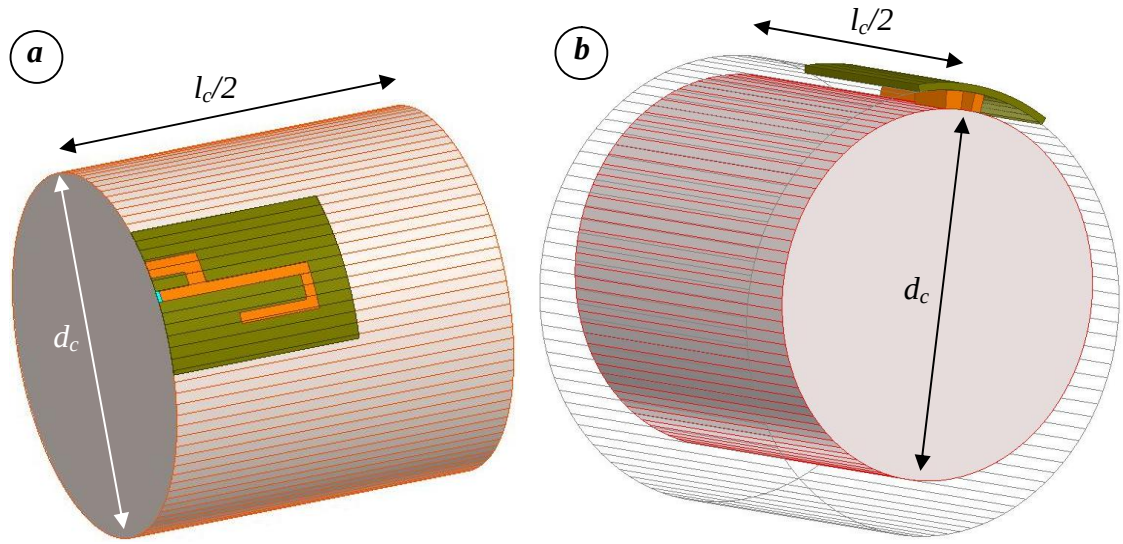

Fig. 4.4. Copper tag on kapton simulated on the effective human arm simulation model having the electrical properties $\varepsilon_{r,eff}$ and tan δ for **(a)**, case 1 and **(b)**, case 2. Case 2 requires an air cylinder for wrapping of the substrate. The dimensions for case 2 are deformed to highlight the simulation set-up.

The arm model and the simulation set-ups have some unavoidable uncertainty sources. The arm model can only represent one possible human arm. The arm size, shape and tissue layers between human individuals can vary significantly. The simulation set-ups cannot perfectly represent the real measured set-up. There will always be some unknown amount of air between the tag and the body and of course, the simulation set-up does not take into consideration body movement. However, the parameters $\varepsilon_{r,eff}$ and

tan δ can to some extend be adjusted to count for possible air layers between the tag and the body, as will be seen later.

The simulations are first conducted for case 1. Table 3.1 suggests that the effective relative permittivity is expected to be between 30–60 and the loss tangent between 0.30–0.50 for human upper arm. However, the simulated realised gain conducted for these permittivity values shows too low values compared to measured results. Eventually, the simulation set-up for case 1 is conducted for permittivity values as low as 5 to reach the same realised gain order of magnitude as the measured one. For case 2, the permittivity is swept for values 10–30 and the loss tangent is swept for values 0.30–0.50.

4.2 Measurements

The measurements are conducted in a shielded anechoic EMC chamber. Its walls are covered with metal layers to prevent external electric fields from disturbing the measurements. The nominal value of the wall attenuation is 120 dB. The internal walls including the floor and ceiling are coated with lossy ferrite that absorbs at least 16 dB power in the frequency range 30−1000 MHz. Additionally, the chamber walls include graphite absorbers to absorb power at 100−1000 MHz and to minimise reflections. The EMC chamber is shown in Fig. 4.5.

Fig. 4.5. The on-body measurements are conducted in an anechoic EMC chamber. The outer dimensions are 6.88 x 3.20 x 3.28 m^3. The electric field uniformity inside the chamber and the wall attenuation accord with the standards EN 61000-4-3 and EN 50147-2. The antenna shown in the right figure is not used during the measurements. Pictures taken from TUT Department of Electronics homepage.

The RFID measurement system itself is described in the next subsection. The system threshold measurement is the prime measurement in this project.

4.2.1 Tagformance measurement system

The Tagformance measurement system [49] consists of Tagformance lite reader unit, reader antenna and Tagformance software. The system is effectively a network analyser

optimised for RFID measurements in the far-field. Field regions are approximate and depend on the wavelength and dimension of the antenna as well as on the application [50]. According to [4] the far-field starts approximately at $r > 2D^2/\lambda$ from the reader antenna surface. The used reader antenna case largest dimension D is 28 cm. At 800−1000 MHz the tag should be placed at a distance of at least r = 52 cm for far-field measurements. The distance used in the free-space measurements is r = 45 cm. When taking into account that the reader antenna largest dimension is smaller than 28 cm and that measured and simulated free-space tag responses agree as seen later, 45 cm is enough to assure that the tag is located in the reader antenna far-field.

Tagformance lite [49] is a bistatic reader unit containing a radio frequency generator and an RF receiver with sensitivity of -80 dBm. The reader offers a measurement frequency range of 800−1000 MHz and transmitted output power of 3−27.8 dBm. The standard protocol supported by the Tagformance software is EPC Class 1 Gen 2 (ISO 1800-6C) [11]. The reader shall communicate with one or more tags by modulating an RF carrier using DSB-ASK with PIE encoding. The tag shall backscatter using ASK and/or PSK modulation with either FM0 baseband or Miller modulation of a subcarrier. Here the tag encodes the backscattered data as FM0.

Calibration of the measurement set-up is required before the actual measurements. A reference tag antenna provided by Voyantic is aligned for polarisation match with the reader antenna at the measurement plane in the far-field. The calibration provides the transmission coefficient τ_{fwd}, or the path loss, between the Tagformance output port TX and the measurement plane. The calibration include therefore information about reader antenna port matching, cable losses, reader antenna power gain G_t, and the free-space attenuation between the reader antenna and the measurement plane. Thus, after the calibration the measurement results are independent of the measurement set-up.

After calibration, different measurements can be conducted with Tagformance measurement system. Threshold measurement describes how much transmitted power $P_{t,th}$ from the Tagformance port TX is required to activate the tag IC as a function of frequency. From τ_{fwd} and $P_{t,th}$, the tag theoretical read range, the realised gain, and the normalised radiation patterns are calculated.

The theoretical threshold power on tag (that is, at the measurement plane) $P_{on\text{-}tag,th}$ can be calculated as follows:

$$P_{on-tag,th} = \tau_{fwd} P_{t,th}. \tag{4.2}$$

The tag IC sensitivity $P_{IC,th}$ is assumed to be -18 dBm. This is the IC minimum threshold power to activate and can be written as the product between the tag to IC transmission coefficient $\tau_{tag\text{-}IC}$ and the minimum required received tag antenna power $P_{r,th}$:

$$P_{IC,th} = \tau_{tag-IC} P_{r,th}. \tag{4.3}$$

According to Eqs. (4.2) and (4.3), the tag IC sensitivity can now be written such that:

$$P_{IC,th} = \tau_{tag-IC} P_{on-tag,th} G_r = \tau_{tag-IC} \tau_{fwd} P_{t,th} G_r, \tag{4.4}$$

where G_r is the tag antenna power gain. Substituting Eq. (4.4) into the Friis transformation Eq. (2.57), the maximum distance at which the tag IC still powers up, that is the maximum forward link read range r_{tag}, is attained in free-space as:

$$r_{tag} = \frac{\lambda}{4\pi} \sqrt{\frac{P_t G_t}{\tau_{fwd} P_{t,th}}}. \tag{4.5}$$

The product $P_t G_t$ = EIRP is in Europe restricted to 3.28 W. Typically, the forward link communication between the reader and the tag limits the read range of passive UHF RFID systems. Therefore, the tag read range is the same as the forward link read range. It is obvious from Eq. (4.5) that the maximum read range is obtained for minimum transmitted power $P_{t,th}$. The tag antenna realised gain $G_{r,real}$ is defined as:

$$G_{r,real} = \tau_{tag-IC} G_r. \tag{4.6}$$

When rearranging Eq. (4.4), the realised gain can be written as a function of the tag IC sensitivity $P_{IC,th}$, the calibration transmission coefficient τ_{fwd}, and the minimum transmitted power $P_{t,th}$, such that:

$$G_{r,real} = \frac{P_{IC,th}}{\tau_{fwd}} \frac{1}{P_{t,th}}. \tag{4.7}$$

In the above equation, the parameters $G_{r,real}$ and $P_{t,th}$ are functions of angle θ between the tag and the reader antenna, while the other two parameters are constants and can be denoted with the constant k. Thus the realised gain can be written as:

$$G_{r,real} = k \frac{1}{P_{t,th}}. \tag{4.8}$$

The Tagformance radiation pattern measurement is used to measure the *E*- and *H*-planes of the tag at a given frequency. The measurement is based on the threshold measurement. At every angle θ, the tag antenna realised gain is plotted. However, for ease of use, clarity, and versatility, radiation patterns are conventionally normalised. Here, the realised gain is normalised to the minimum transmitted power $P_{th,min}$, or equivalently maximum realised gain, attained at a given angle. At all other angles, the

transmitted power is greater, or equivalently the realised gain is smaller. Using Eq. (4.8), the normalised radiation pattern is attained as:

$$G_{r,real,norm} = \frac{G_{r,real}}{G_{r,real,\max}} = \frac{k / P_{t,th}}{k / P_{th,\min}} = \frac{P_{th,\min}}{P_{t,th}}, \tag{4.9}$$

$$G_{r,real,norm} = P_{th,\min}\ (\text{dBm}) - P_{t,th}\ (\text{dBm}) . \tag{4.10}$$

The normalised realised gain value that corresponds to $P_{th,min}$ is 0 dB. At all other angles the transmitted power is greater and the normalised realised gain value smaller.

4.2.2 Free-space measurements of the tag antenna for model testing

The Tagformance lite can be combined with a compact, shielded and anechoic test cabinet by Voyantic [51] for measuring RFID tags, as shown in Fig. 4.6. The RFID cabinet is a convenient solution when the measured target is relatively small and when the user has limited access to an anechoic EMC chamber.

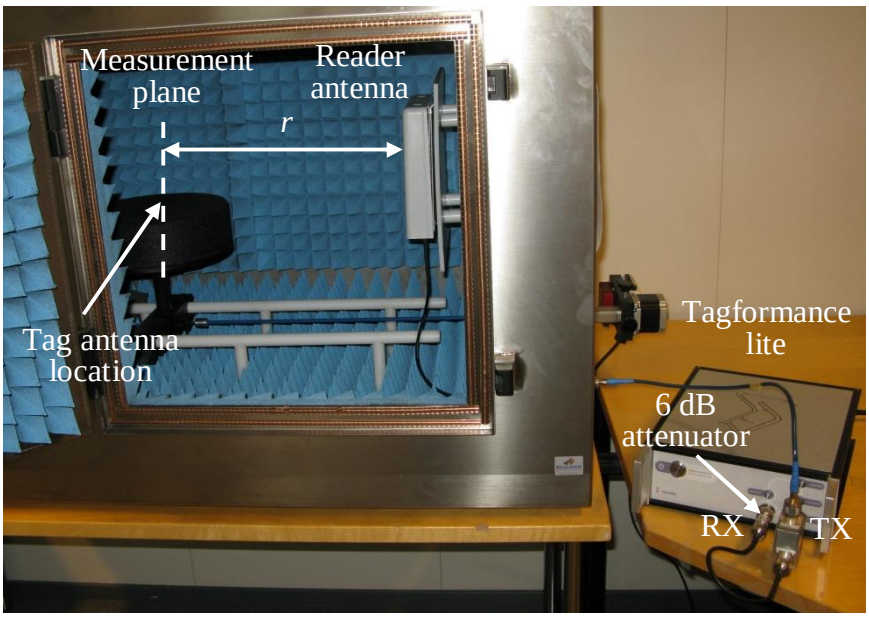

Fig. 4.6. Tagformance measurement system combined with a compact RFID cabinet. A 6-dB attenuator is connected to RX port to keep the receiver always in its linear dynamic range [49]. After calibration, the tag realised gain and read range can be obtained from the threshold measurement, while the radiation patterns are attained through the orientation measurement. Picture taken by Eveliina Koski.

The vertical polarised reader patch antenna [52] is connected to the externally located Tagformance lite measurement device. The Tagformance lite is computer-controlled via the Tagformance software. The tag is located at the measurement plane on the computer-controlled rotating table. The copper tag free-space performance is evaluated in the test cabinet. The measurement set-up is calibrated for tag (measurement plane) to reader distance r = 45 cm. The measurements are hence conducted in the far-field. The

measurement set-up inside the RFID cabinet is shown in Fig. 4.7. A frequency step of 0.5 MHz and transmitted output power step of 0.1 dB are used. For the radiation pattern measurement, an angle step of 5° is used.

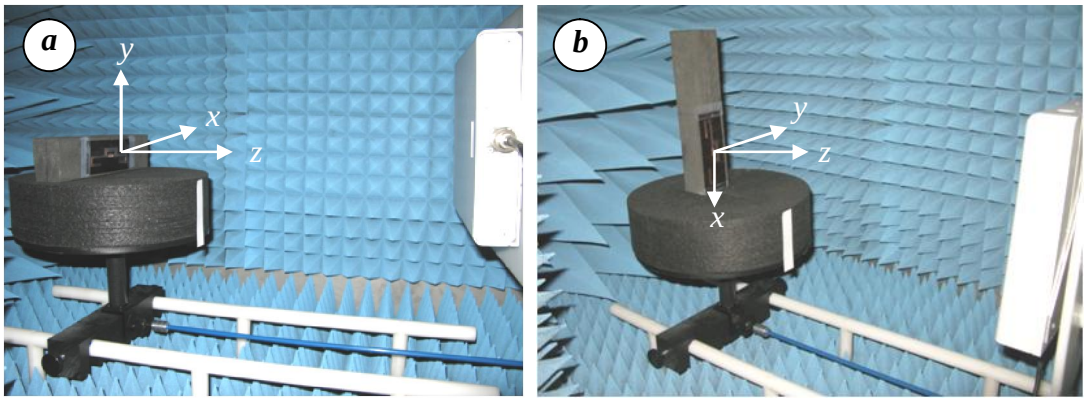

Fig. 4.7. Free-space measurements of the copper tag. The tag is aligned for polarisation match with respect to the vertical polarised reader antenna at measurement angle 0° at the measurement plane. Measurement set-up inside the RFID cabinet for **(a)**, threshold and *E*-plane (*zx*-plane) measurement and **(b)**, *H*-plane (*zy*-plane) measurement.

The tag is positioned at the measurement plane. At a measurement angle of 0°, the tag is facing the reader antenna. Threshold measurement is conducted for the *E*-plane measurement set-up, after which the tag maximum forward link read range and realised gain can be plotted according to Eqs. (4.5) and (4.7), respectively. The calculated theoretical maximum forward link read range is shown below in Fig. 4.8 together with the simulated response.

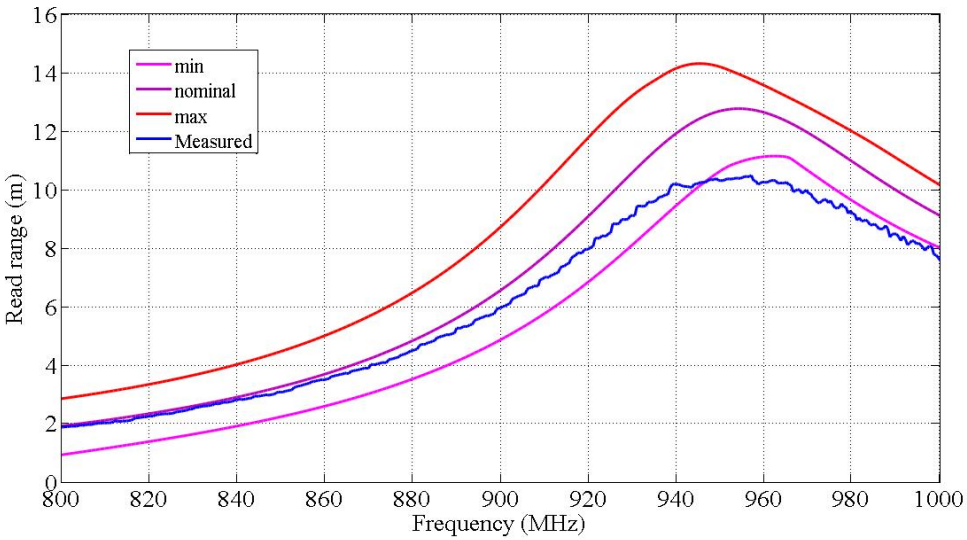

Fig. 4.8. Copper tag maximum forward link read range in free-space in +*z* direction. The tag is performing as expected; the measured and simulated responses agree. The responses show a peak read range at 950 MHz. A maximum difference of 3.0 metres is attained between the measured and nominal simulated responses. The measured response is within the simulated uncertainty limits based on the tag antenna and IC impedance uncertainties up to 940 MHz. However, in addition to the impedance uncertainties, there are other uncertainty factors that affect the results.

The tag has, as desired, its optimum performance at 950 MHz, at which the measured peak read range exceeds 10 metres. This read range is enough to ensure that the tag antenna will still respond when attached to the human arm even when significant tag performance degradation is encountered. Moreover, keeping the measurement frequency range in mind, the high 950-MHz optimum performance frequency gives room for a relatively large frequency shift when the tag is attached to arm.

The nominal optimum simulated response is 13 metres at 950 MHz. The 3-metres difference between the measured and simulated responses is mainly caused by three prominent factors: the used NXP IC and the tag antenna simulation models, the handmade tag antenna fabrication, and the Tagformance measurement system itself. All of these comprise uncertainties that contribute to errors. To highlight the simulated uncertainties, a method described in [47] is used. The IC impedance model uncertainty is $\pm(0.4 + j1.5)\ \Omega$, and the antenna impedance is assumed to be 5% around the simulated resistance and reactance [47]. In addition, 10% variation is considered for the simulated antenna gain. As seen from Fig. 4.8, the measured response is within the uncertainty limits up to 950 MHz. The simulator models the tag antenna materials by its electrical properties. These properties are most probably not identical to the real material properties, since these cannot be measured with infinite accuracy. The tag antenna dimensions suffer from poor accuracy due to the handmade fabrication. The accuracy is estimated to ±0.5 mm. With other words, the dimensions of the fabricated tag might not correspond to those used in the simulations. Finally, it is important to remember that no measurement equipment is ideal. Of course, the Tagformance measurement system has limited accuracy [49] that affects the measurement results. The tag antenna alignment in the measurement cabinet contributes likewise to errors. Strictly, the measurement planes might not exactly be the desired *zy*- and *zx*-planes.

The calculated tag antenna realised gain is depicted in Fig. 4.9. The maximum value is approximately -1 dBi at the optimum performance frequency, whereas the simulated maximum is over 1 dBi. The difference can be explained similarly as for the maximum read range. The measured maximum realised gain is high enough to guarantee a reasonable realised gain even when the tag is affected by the human body.

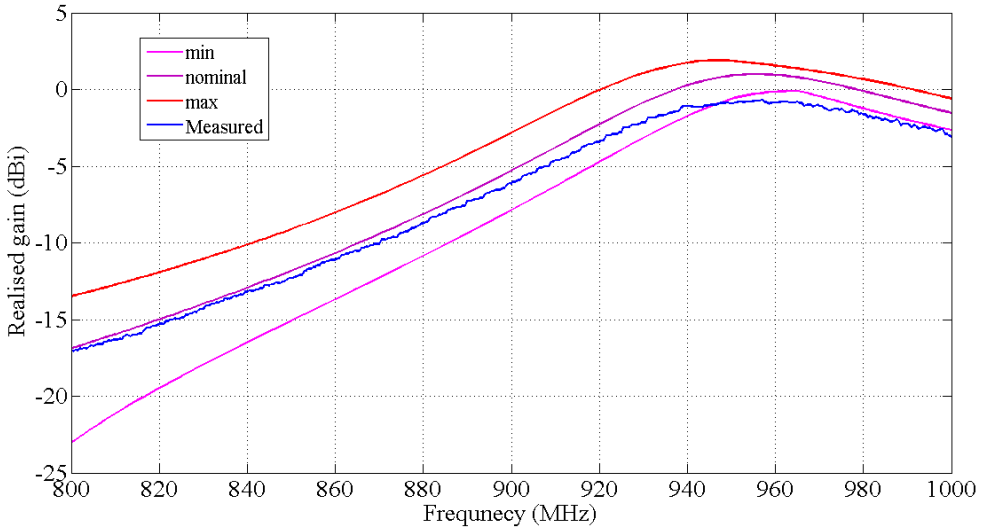

Fig. 4.9. Copper tag realised gain in free-space in +*z* direction. A maximum value of -1 dBi is measured at 950 MHz. Even though the measured response is lower that the simulated one, the measurement result is reasonable when taking into account the related uncertainties. The tag is providing a high enough realised gain in free-space to afford a severe degradation close to the human arm.

Radiation pattern measurement is conducted for the *H*-plane and *E*-plane measurement set-ups at the 950-MHz optimum performance frequency. Since this frequency comprises the maximum realised gain value, it is easy to notice how much the realised gain is degraded from its maximum value. The rotating table is rotating counter-clockwise. For each 5°-step the realised gain is plotted. The realised gain is normalised according to Eq. (4.10). The result is shown in Fig. 4.10.

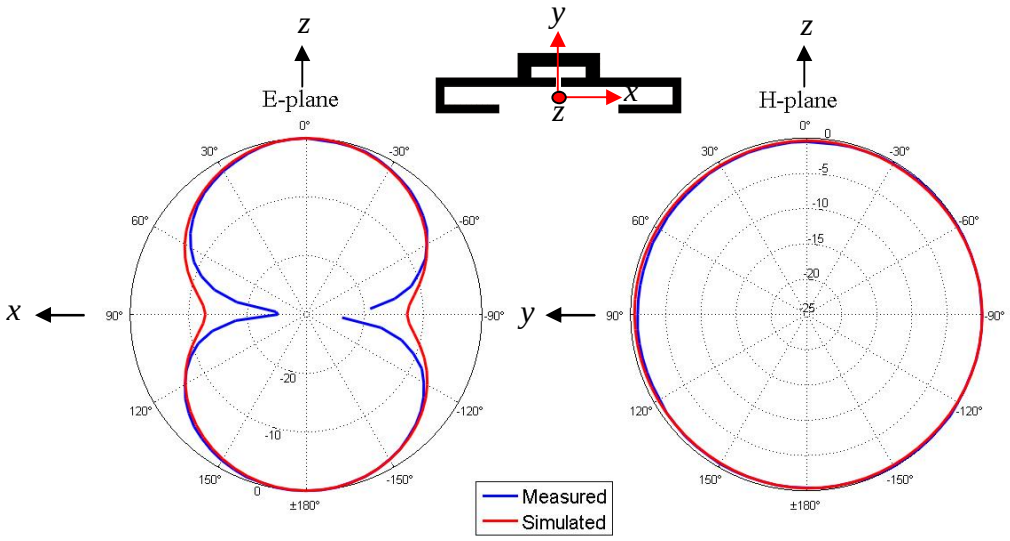

Fig. 4.10. Copper tag *E*- and *H*-plane radiation patterns at 950 MHz. The simulated and measured patterns agree well. The *E*-plane (*zx*-plane) indicates a typical dipole radiation pattern. The radiation pattern is omnidirectional.

The maximum realised gain is attained at angles 0°and ±180°. As expected, the tag is not radiating along the radiating element (*x*-axis) in the *E*-plane. The radiation patterns are typical for a dipole tag antenna.

In summary, the copper tag antenna fulfils the performance criteria required for on-body measurements. Next, the tag is measured on-body in the anechoic EMC chamber in order to indirectly extract the electrical properties of the human arm.

4.2.3 Measurement set-up

Measurements are conducted for the both simulated cases. The copper tag is attached directly to the right upper arm with conventional tape as tight to the skin as possible as shown in Fig. 4.11. The tag height above the floor is 114 cm.

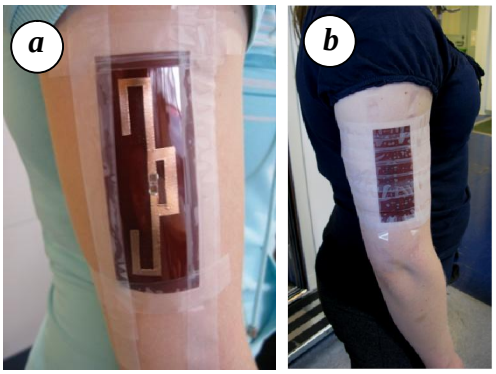

Fig. 4.11. Copper tag position on arm for **(a)**, case 1 and **(b)**, case 2. The position is selected for several reasons: (1) the upper arm provides a relatively flat area to attach the tag on, (2) the tag is not covered by other body parts, (3) the height above floor is suitable for wearable RFID tag applications, (4) the position enables tag antenna integration into clothing and (5), earlier publications suggest that this is a good selection for wearable tag antennas.

The measurements are conducted in the EMC chamber using the Tagformance measurement system. The used reader antenna [53] has linear vertical polarisation. The measurement set-up is calibrated for tag (measurement plane) to reader antenna distance r = 60 cm. The measurements are hence conducted in the far-field. The calibration set-up is given in Fig. 4.12.

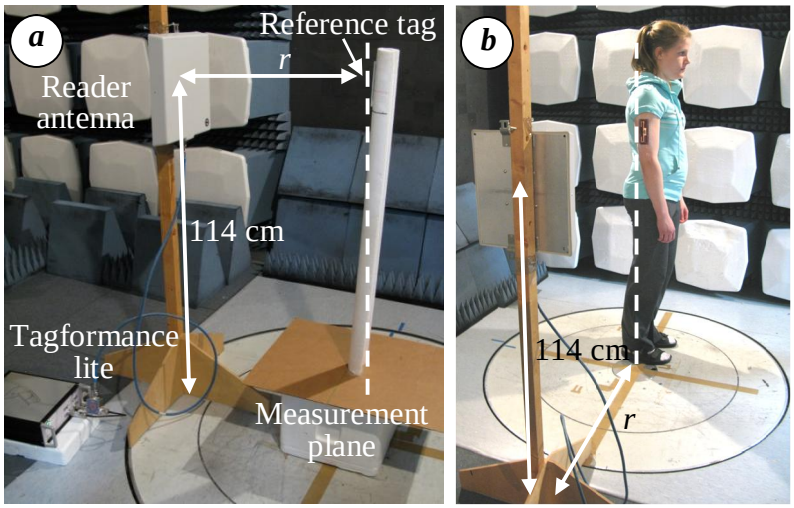

Fig. 4.12. **(a)** Measurement set-up for calibration for tag (measurement plane) to reader antenna distance r = 60 cm. The reference tag is mounted 114 cm above the floor. The calibration provides the desired transmission coefficient τ_{fwd} between the Tagformance output port TX and the measurement plane for later calculations. **(b)** Measurement set-up for actual copper tag on-body measurements for both cases. The copper tag is aligned at the measurement plane in the reader antenna direct line of sight. Threshold measurement is conducted for post-processing of realised gain.

After calibration, the reference tag is replaced by the copper tag attached on-body as shown in Fig. 4.12. The copper tag is positioned at the measurement plane to keep the same tag-to-reader antenna distance. Threshold measurement is repeated for both cases to attain a measure of the measurement repeatability.

4.2.4 Measurement results and discussion

The copper tag calculated realised gain for the both cases is given in Fig. 4.13. As expected, the gain drops notably near the human body. Within the global UHF RFID frequency band 860−960 MHz the degradation order of magnitude is 10−20 dB. At first glance, it seems that the human body does not expose the case 1 tag to any resonance frequency shift. However, it should be remembered the measurement frequency range is far too narrow to draw any conclusions involving the infinite frequency band. The measured resonance frequency at 950 MHz might not be of the same order of resonance as the one measured in free-space. In such case, there actually is a frequency shift of the free-space resonance towards lower frequencies but it is falling outside the measurement band. When considering case 2, the frequency shift is more obvious, even though the unconsciousness about resonance order is still present.

The realised gain measurement results show that the human body has greater impact on the tag performance in case 2 compared to case 1. Clearly, the tag antenna conductor against the body in case 2 reinforces the interaction between the tag antenna and the body, whereas in case 1 the substrate provides tag-to-body isolation. Additionally, the substrate is not flexible enough to assure permanent contact. This is primarily critical is case 2 since the tag antenna conductor is facing the skin. As a consequence, the repeatability of case 2 is poorer. Moreover, the responses attained in

case 2 are more prone to fluctuations. These fluctuations are a result of tag movement when the human is breathing.

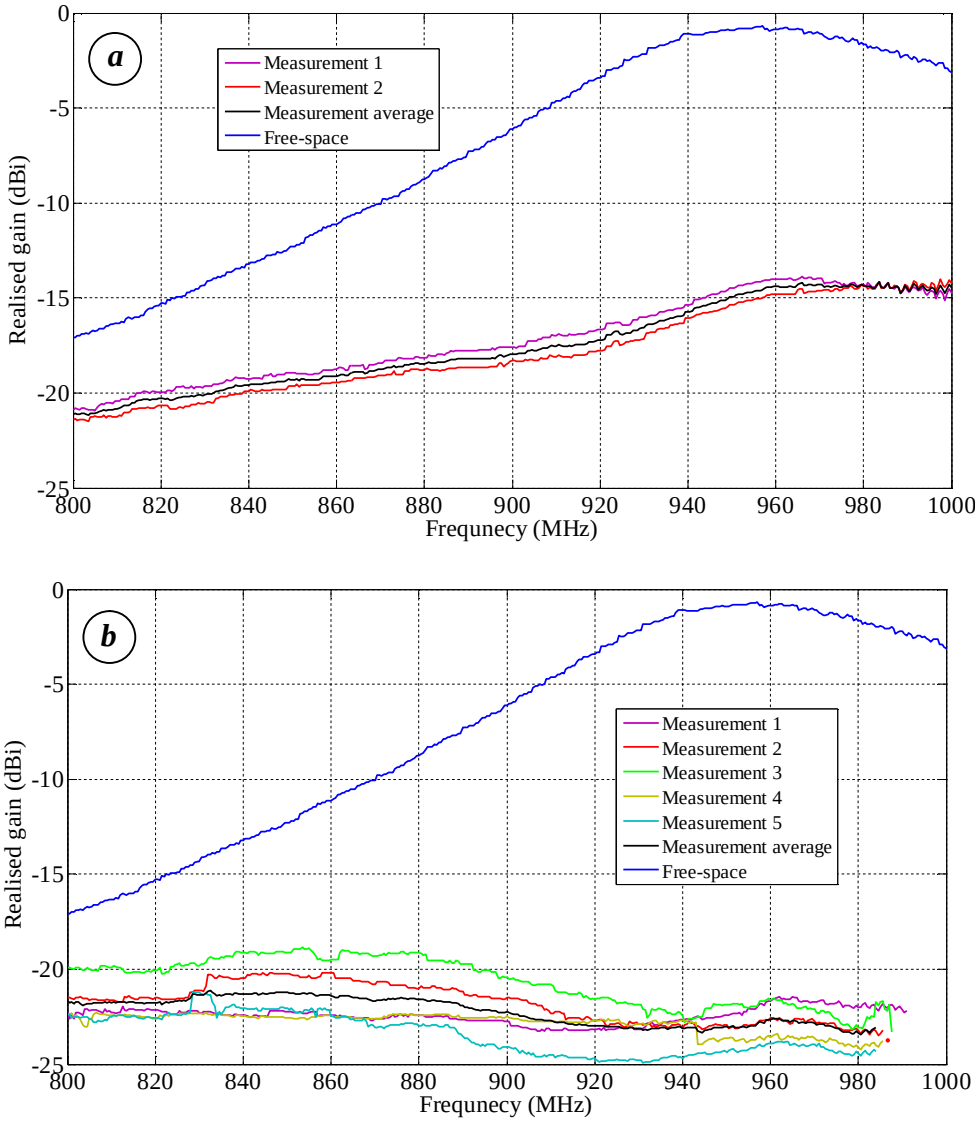

Fig. 4.13. Copper tag calculated realised gain on-body based on the calibration and threshold measurements for **(a)**, case 1 and **(b)**, case 2. Significant tag performance degradation is encountered. The tag-to-body interaction is more prominent in case 2 due to the direct contact between the tag antenna conductor and the body. In case 1 the substrate provides isolation between the tag and the body.

Unfortunately, it is extremely unlikely that a perfect relationship between the simulated and measured curves is observed. There are two reasons for this. The first is the accuracy of the human arm and tag antenna simulation models; the second is the measurement uncertainty. However, it is possible to find for each case the parameters $\varepsilon_{r,eff}$ and tan δ that provide best agreement between the measured and simulated data. The method of least squares [54–55] assumes that the best-fit curve is the one that has the minimum sum of the deviations, or residuals, squared between the measured data and the simulated data. Let the measured data be the measurement average in Fig. 4.13. The measured data $\boldsymbol{g}(f_i,G_i)$ consists of n data pairs, where $i = 1...n$. Here n equals to the

number of frequency points (11) in the simulations. The pair (f_i,G_i) consist of the independent frequency variable f_i and the dependent realised gain variable G_i. The simulated realised gain curves are the model functions, that is, the predicted values, and have the form $\boldsymbol{f}(f_i,\beta)$. Each model function holds a vector β with the unique parameter combination of $\varepsilon_{r,eff}$ and tan δ. The aim is to find the model function that best fits the measured data. The least squares method provides the sum of squared residuals between each model function and the measured data:

$$S = \sum_{i=1}^{n} r_i^2, \tag{4.11}$$

where the residual r_i is defined as the difference between the actual value of the dependent variable G_i and the value predicted by the model:

$$r_i = G_i - \boldsymbol{f}(f_i, \beta). \tag{4.12}$$

The sum of squared residuals S is plotted between each model function and the measured data, as shown in Fig. 4.14. In case 1 the $\varepsilon_{r,eff}$ and tan δ parameter values are simulated for values 5–10 with 1-step and 0.30–0.50 with 0.01-step, respectively. In case 2 the corresponding parameter values are 10–30 with 1-step and 0.30–0.50 with 0.05-step, respectively.

The graphs in Fig. 4.14 should be read the following way. The *x*-axis for case 1 is divided into 21 subsections, each with a fixed tan δ value beginning with 0.30 and increasing by 0.01-step to the next subsection so that the tan δ value is 0.50 in the last subsection. One subsection contains 6 data points. The first point in the subsection is associated with the $\varepsilon_{r,eff}$ value 5, the second point with the value 6 and so on. The last point is associated with the $\varepsilon_{r,eff}$ value 10. Case 2 has 5 subsections, each with a fixed tan δ value beginning with 0.30 and increasing by 0.05-step to the next subsection so that the tan δ value is 0.50 in the last subsection. One subsection contains 21 data points. The first data point represents the $\varepsilon_{r,eff}$ value 10 and the last point the value 30.

In case 1 the sum of squared residuals is minimized for the model function 122. The β vector of this function holds the parameter values $\varepsilon_{r,eff}$ = 6 and tan δ = 0.50. In case 2 the corresponding model function is 31 and the parameter values are $\varepsilon_{r,eff}$ = 19 and tan δ = 0.35.

For both cases the effective relative permittivity for the human arm simulation model is far smaller than the expected of 30−60. In fact, case 1 suggests that the human arm consists solely of fat tissue, whereas case 2 suggests that the human consists of bone tissue in addition to fat tissue, refer to Table 3.1. This is however not the case. When considering the measurement set-up in both cases, it is obvious that air will be trapped between the tag antenna and the skin. Air has a relative permittivity of 1 and loss tangent of 0. The trapped air will provide isolation between the tag and the human

arm. Hence, the measured realised gain will be higher compared to a fictional set-up where no air would be trapped between the tag and the skin. The simulation models for case 1 and 2 do not take the measured trapped air into account, but represent instead the fictional set-up with no trapped air. Therefore, low effective relative permittivity values for the human arm models are required to compensate for the trapped air and further, to have agreement between the simulated and measured realised gain responses.

As seen from Fig. 4.14, the $\varepsilon_{r,eff}$ value affects the sum of squared residuals S significantly more than the tan δ value. Having $\varepsilon_{r,eff}$ set to 6 and 19 in case 1 and 2, respectively, the value of tan δ will not have large impact on the achieved S.

The effective relative permittivity of the human arm model for case 2 is more than three times greater than for case 1. This is expected. Case 2 allows the tag antenna conductor to be closer attached to the arm. Hence, less air is trapped between the tag antenna and the skin compared to case 1. As a consequence, a higher effective relative permittivity value for the human arm model 2 is required to have agreements between the simulated and measured realised gain responses.

Fig. 4.14 implies that case 2 provides a human arm model with better agreement between simulated and measured responses. For case 2 the sum of least squared residuals is at minimum 2.4, whereas for case 1 the sum is 13.2. It should, however, be remembered that the simulated responses are compared to the averaged measurement average. The measurement repetition amount is not sufficient to conclude about the accuracy between case 1 and 2. In addition, the plots in Fig. 4.14 are not directly comparable since different $\varepsilon_{r,eff}$ and tan δ steps are used in simulations for the different cases.

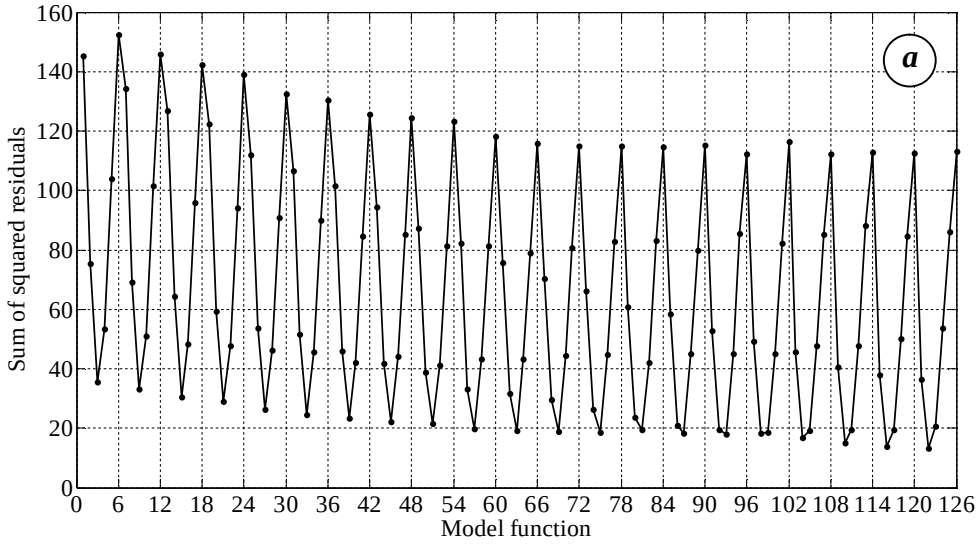

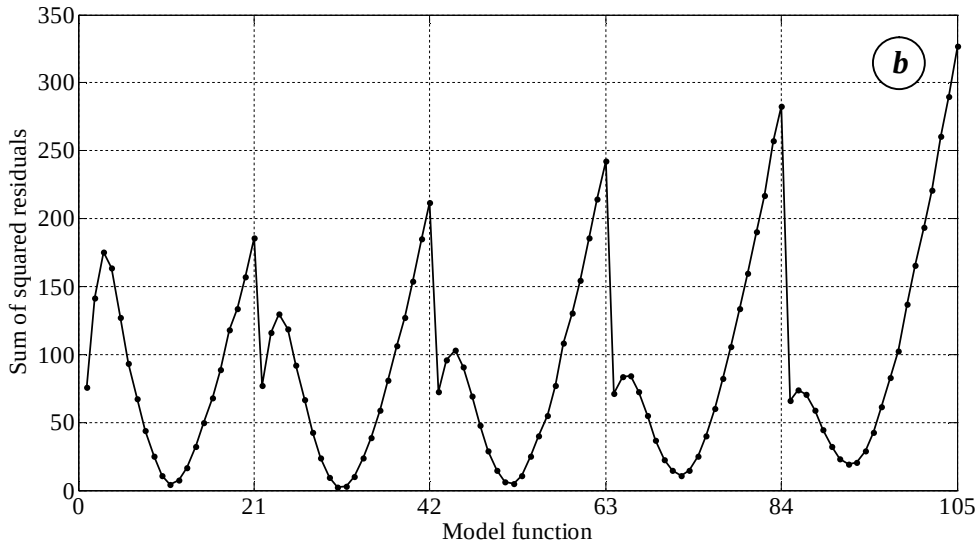

Fig. 4.14. Sum of squared residuals between the model functions (simulated realised gain curves) and the measured data (measurement average) for **(a)**, case 1 and **(b)**, case 2. Each model function is related to a unique parameter combination of $\varepsilon_{r,eff}$ and tan δ. For case 1 the β vectors of the model functions hold $\varepsilon_{r,eff}$ values 5–10 and tan δ values 0.30–0.50. The β vectors in case 2 include $\varepsilon_{r,eff}$ values 10–30 and tan δ values 0.30–0.50. For case 1 the sum of squared residuals finds its minimum for the model function 122, which corresponds to the parameter values $\varepsilon_{r,eff}$ = 6 and tan δ = 0.50. The corresponding model function for case 2 is 31 with the parameter values $\varepsilon_{r,eff}$ = 19 and tan δ = 0.35.

The measurement average is plotted in Fig. 4.15 together with the simulated realised gain attained for the human arm simulation model for which the sum of squared residuals is minimised. The simulation models predict the realised gain responses with ±2 dB and ±1 dB accuracy for case 1 and 2, respectively, when the measured response is the measurement average. The accuracy is relative good when taking into account the uncertainties caused by the simulation models themselves and the practical measurements.

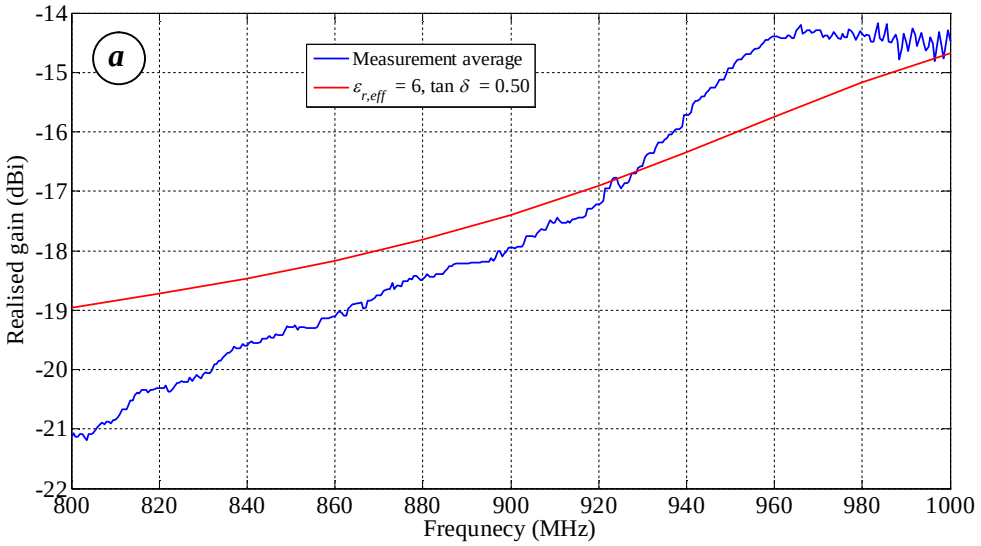

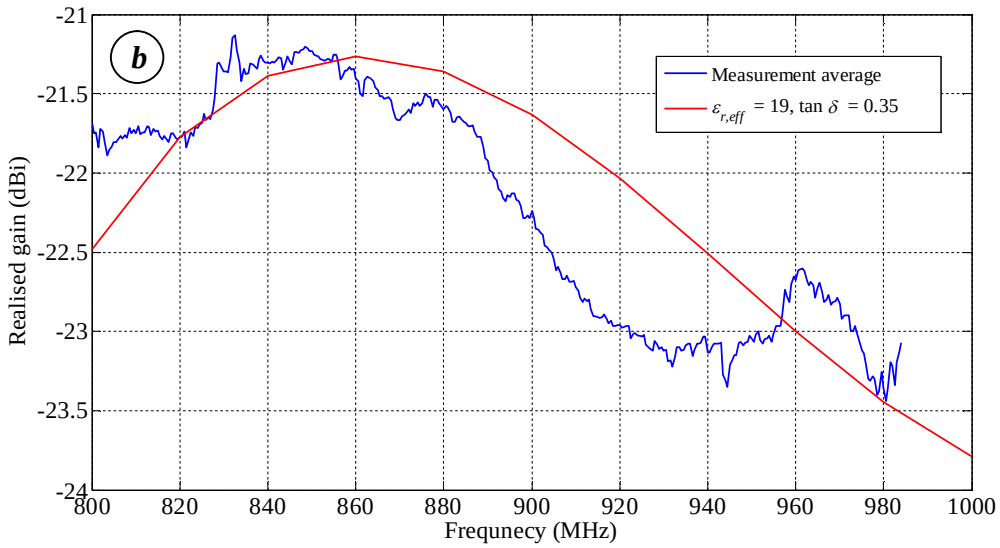

Fig. 4.15. Realised gain measurement average and simulated response for simulation model for which the sum of squared residuals is minimised, **(a)** case 1 and, **(b)** case 2. Within the measured frequency band, the simulated response maximum deviation from the measurement average response is ±2 dB for case 1 and ±1 dB for case 2. The tag does not respond at the supreme frequencies in case 2, whereas in case 1 the tag will most probably respond even beyond 1000 MHz. When taking into account the uncertainties involved in the measurements and the simulation models, the results suggest that the developed human arm simulation models predict accurately the tag antenna performance when attached on-body.

Both simulation models have advantages and disadvantages, making it challenging to decide which model should be used when optimising wearable passive UHF RFID tags on-body. Case 1 has relatively good repeatability and the response is stable, but the effects of the human body are not highlighted due to the isolation provided by the substrate. Case 2 suffer from poorer repeatability and response stability, but the human body effects on tag performance is clearly seen. Moreover, the human arm simulation models provide similar accuracies. On the basis of these advantages and disadvantages, it is worth verifying both simulation models using wearable RFID tags. This verification is conducted in the next Section.

5 HUMAN ARM MODEL VERIFICATION AND TAG OPTIMISATION

The developed human arm simulation models in Section 4 are verified in this Section using embroidered wearable passive UHF RFID tags. This verification is needed before optimisation of wearable tags on the human arm.

5.1 Simulated wearable RFID tags on human arm

In [44], a method for estimating the effective conductivity of the tag antenna embroidery pattern is presented. The effective conductivity depends on the tag antenna sewing pattern and stitch density. Three prototypes are selected from [44]; one prototype with low stitching zigzag density (E1) and two prototypes of different lengths with higher zigzag density (E2 and E3). Otherwise, the tags are identical. All three prototype sewing patterns consist of a horizontal line along the length of the dipole, and zigzags sewed vertically cross it. The prototypes are shown in Fig. 5.1. Shieldex 110f34 dtex 2-ply HC [56] conductive sewing thread is used to create the tag antenna pattern and cotton fabric is used as the substrate material. The thread is created from two strands of conductive fibres, each having a weight of 110 dtex. The unit dtex is the mass in grams per 10000 metres. The fibres are multi-filament, each consisting of 34 filaments. The filaments have a polyamide core plated with 99% silver. The metallised thread has a weight of 275 dtex. The thread is reported to have a DC resistivity of 500 Ω/m ± 100 Ω/m. The embroidered tag fabrication process is explained in Section 3.3. The prototype embroidered tags are designed for Alien Higgs-3 UHF RFID IC, which has a sensitivity of -18 dBm. The equivalent circuit model consists of an RC parallel circuit, as depicted in Fig. 4.2, but this IC has an equivalent input parallel resistance of 1500 Ω and an equivalent input parallel capacitance of 0.85 pF.

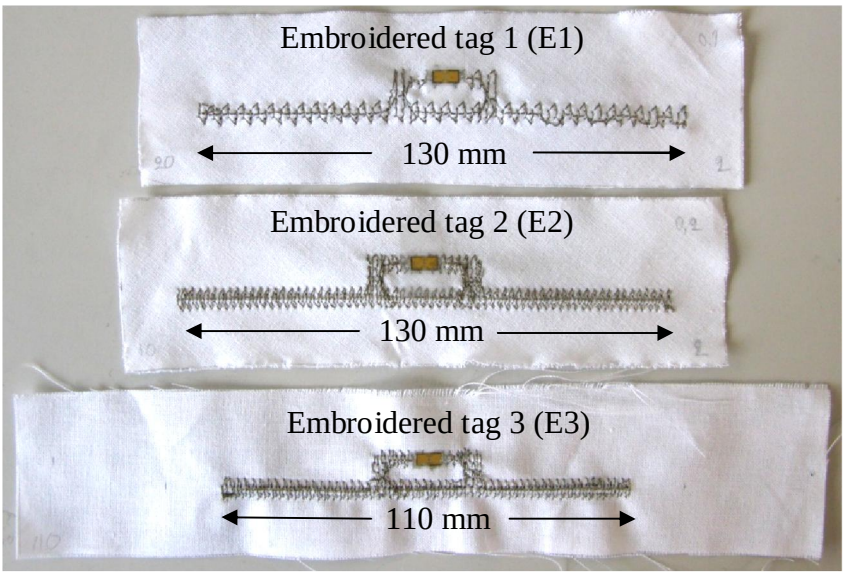

Fig. 5.1. Embroidered dipole tag antennas from [44] used to verify the human arm simulation model. The tag antenna pattern is created using conductive sewing thread. Cotton fabric is used as the substrate material and the Higgs-3 IC is attached over the 1 mm gap using conductive epoxy.

The thickness of the embroidered tag antennas depends on the stitching density. When the density is high enough, the tag antenna resembles a flat and solid structure with a uniform thickness. However, when the density is low, the tag antenna pattern is not flat and solid. It is therefore not convenient to define a thickness. Still, the tag antenna pattern, independent of the stitch density, can be modelled as a flat and solid pattern on one side of the substrate with a thickness t and effective conductivity σ_{eff} [44]. The measured upper face of each tag is defined as the thickness of the conductive tag antenna pattern. The effective conductivity for each tag is found by simulating the embroidered dipole with different conductivities until the tag response matches with the measured response [44]. The electrical properties of cotton are determined using the resonance method suggested in [57]. The material properties of the selected embroidered tags are collected in Table 5.1.

Table 5.1. Embroidered tag antenna material used in the HFSS simulations.

Material	Conductivity σ_{eff} (kS/m)			Loss tangent tan δ	Thickness t (mm)			Relative permittivity ε_r
Tag	E1	E2	E3		E1	E2	E3	
Thread [56]	8.0	4.0	4.0	0	0.1	0.2	0.2	1
Cotton fabric		-		0.018		0.25		1.8

According to the results obtained in [44], the effective conductivity of the sewed dipoles decreases with increasing stitch density and conductor thickness. The reason might be interactions between adjacent threads in the densely sewed antenna pattern that cause unexpected losses [44]. The free-space operation of these embroidered tags is found in [44].

The embroidered tags are simulated on the human arm model developed in the previous Section for both cases. The simulation set-ups are given in Fig. 5.2.

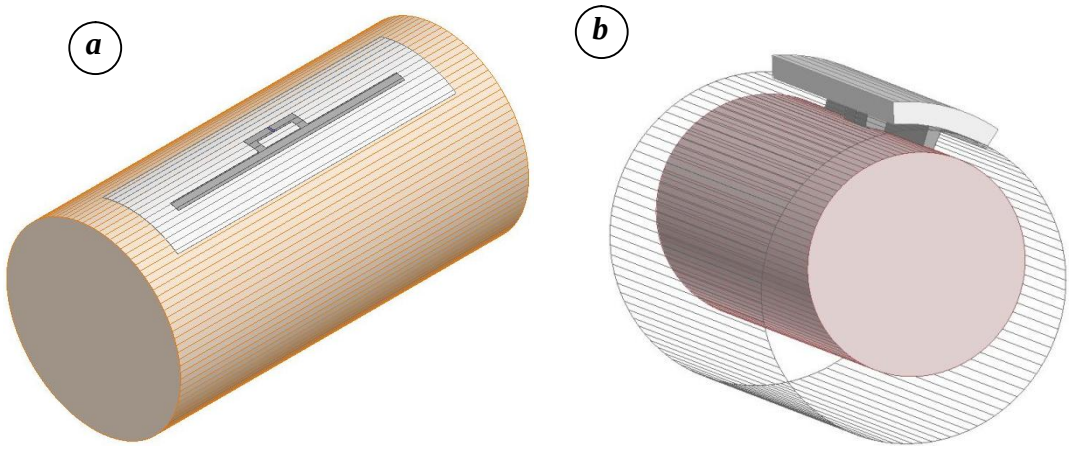

Fig. 5.2. Embroidered tag on cotton fabric simulated on the effective human arm simulation model having the electrical properties $\varepsilon_{r,eff}$ and tan δ for **(a)**, case 1 and **(b)**, case 2. Case 2 requires an air cylinder for wrapping of the substrate. The dimensions for case 2 are deformed to highlight the simulation set-up.

In case 1 the arm electrical properties are $\varepsilon_{r,eff}$ = 6 and tan δ = 0.50, whereas for case 2 they are $\varepsilon_{r,eff}$ = 19 and tan δ = 0.35. The simulation results are presented together with the measurement results in the next subsection.

5.2 Measurement results and discussion

Measurements are conducted for the both simulated cases similarly as for the copper tag on kapton. The measurement set-up is calibrated using the reference tag before actual measurements for tag (measurement plane) to reader antenna distance r = 60 cm. The embroidered tag antennas are attached directly to the right upper arm with conventional tape as tight to the skin as possible as shown in Fig. 5.3. The tag height above the floor is 114 cm and the tag (measurement plane) to reader antenna distance is r = 60 cm. Threshold measurement is conducted for both cases.

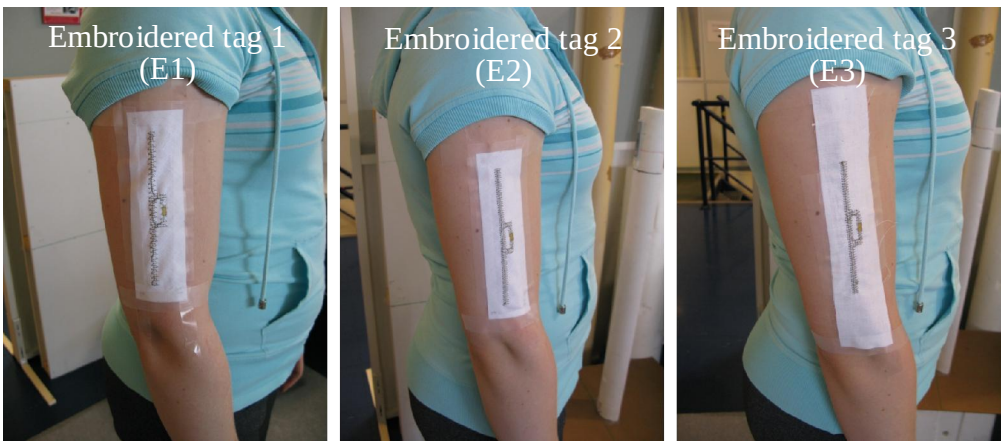

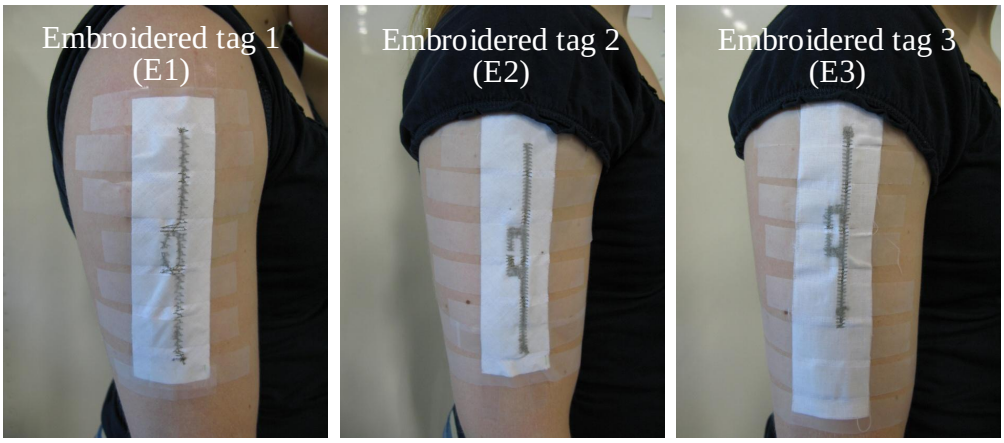

Fig. 5.3. Embroidered tag position on arm for case 1 (above) and case 2 (below). Compared to the copper tag on kapton, the embroidered tag has conductive tag antenna pattern on both side of the substrate.

The simulated and calculated realised gain according to Eq. (4.7) for the embroidered tags are shown below in Figs. 5.4–5.9. The measurement repeatability is good and therefore only the measurement average is plotted.

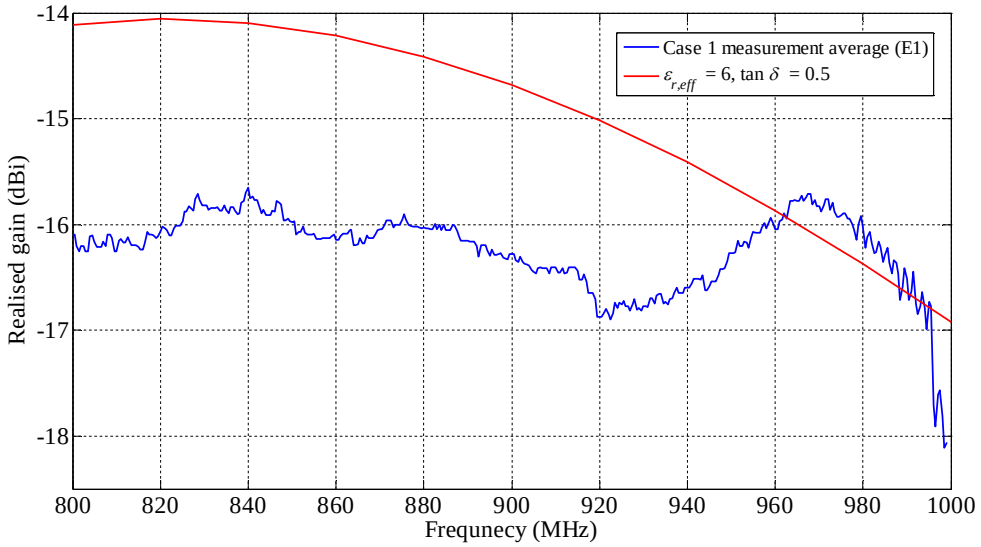

Fig. 5.4. Simulated and measured embroidered tag 1 realised gain on the human arm for case 1. The accuracy of the human arm model is ±2 dB over the whole measured band.

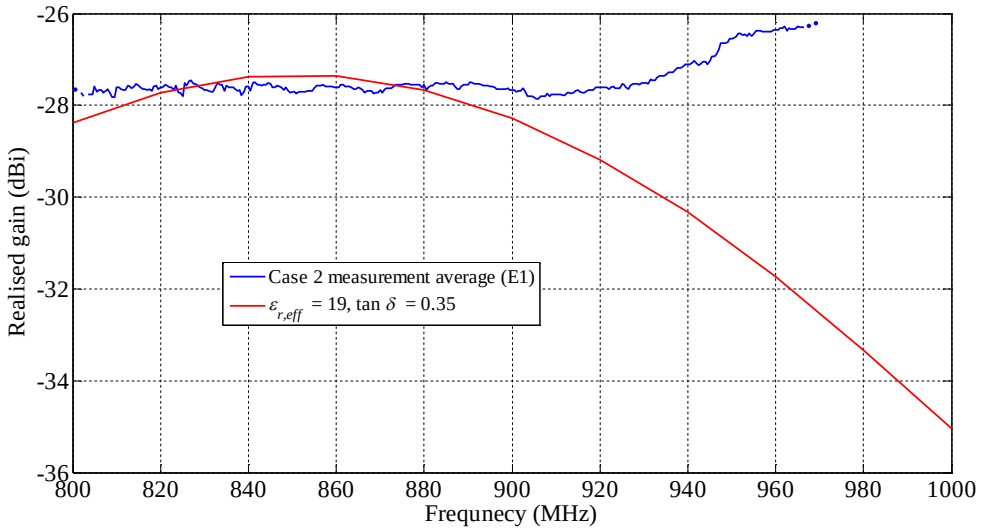

Fig. 5.5. Simulated and measured embroidered tag 1 realised gain on the human arm for case 2. The model estimates the tag performance with high accuracy up to 900 MHz. At higher frequencies the accuracy is poor. The tag is not responding at 960–1000 MHz.

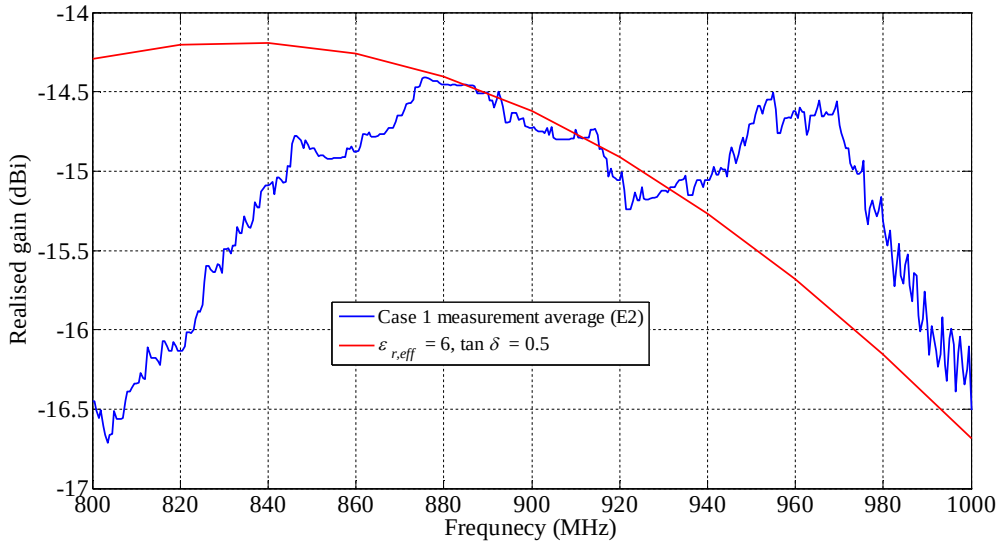

Fig. 5.6. Simulated and measured embroidered tag 2 realised gain on the human arm for case 1. In the range 875–940 MHz, the performance prediction is good. Within the UHF RFID band, the accuracy of the human arm model is ±1 dB.

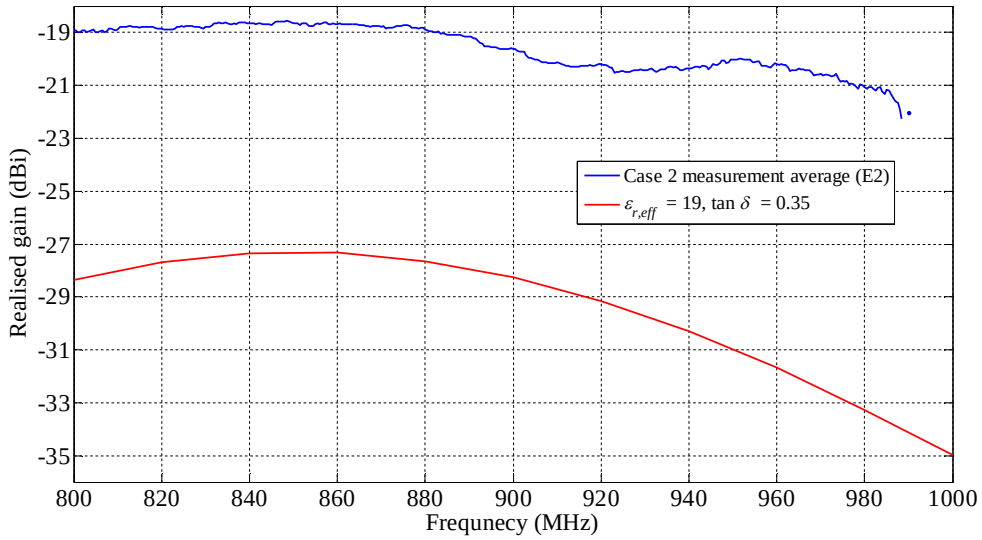

Fig. 5.7. Simulated and measured embroidered tag 2 realised gain on the human arm for case 2. The estimation is bad over the whole frequency band. The tag is not responding at 990–1000 MHz.

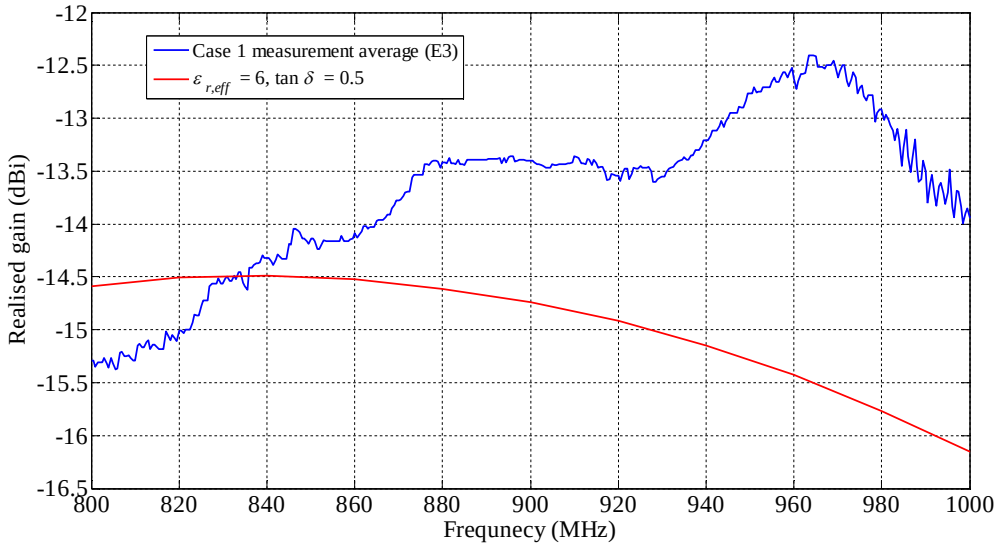

Fig. 5.8. Simulated and measured embroidered tag 3 realised gain on the human arm for case 1. Within the UHF RFID band, the accuracy of the human arm model is ±3 dB.

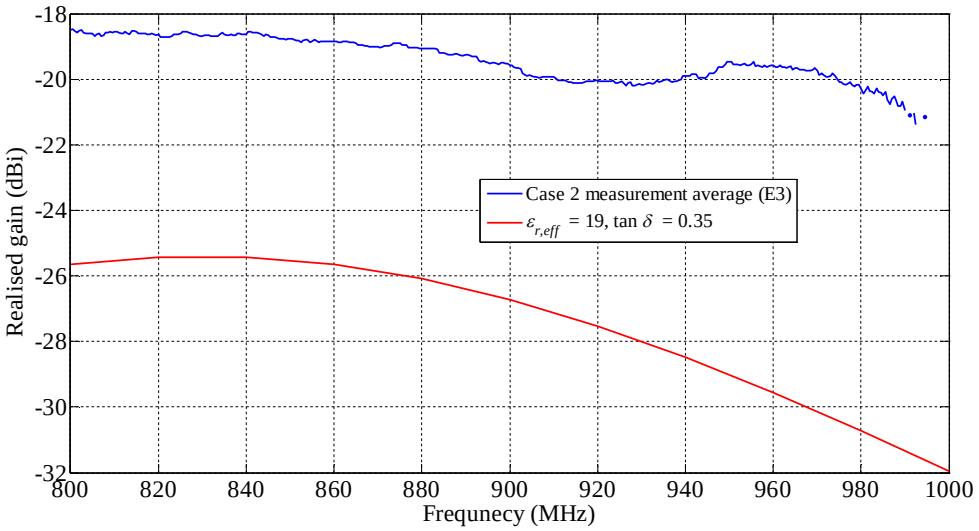

Fig. 5.9. Simulated and measured embroidered tag 2 realised gain on the human arm for case 2. The estimation is bad over the whole frequency band. The tag is not responding at 990–1000 MHz.

As expected, the body has greater impact in case 2 compared to case 1. For case 1, the simulation results are almost similar independent of the tag. However, the measurement results are different depending on the measured tag. Obviously, the human arm model together with the embroidered tag model is not predicting the shape of the response as good as for the copper tag. Regardless of this, the human arm simulation model is providing an accuracy of ±3 dB for case 1 over the whole frequency band.

The prediction in case 2 is poor: ±10 dB. At higher frequencies the tags stop to respond. This is probably due to the increased losses in the arm tissues. Interestingly, the measured results for embroidered tags 2 and 3 are notably better than the simulated responses. For the embroidered tag 1 the measured and simulated agreement is good up to approximately 900 MHz. Compared to the copper tag on kapton, the embroidered tags have conductor on both sides of the substrate. As Fig. 5.2 shows, the embroidered tags are simulated with conductor only on one side. The measurements represent hence a more favourable case for the tag compared to the simulations. In tags 2 and 3 the stitch density is significantly denser than for tag 1. Based on the measurements it seems that in case 2, where the IC is against the skin, the effect of body is greater for tags with lower stitch density.

As remembered from Section 4, the measurements include also the unavoidable air between the on-body attached tag antenna and the skin. The embroidered tags are more flexible than the copper tag on kapton. The amount of air is most probably different depending on the flexibility of the measured tag antenna. This adds an uncertainty source to the developed human arm model.

In summary, the developed human arm simulation model for case 1 together with the embroidered tag simulation model [44] can be used to optimise wearable tags on the human arm upper arm. Even though the simulation model is relatively simple, it gives valuable information about the tag performance with acceptable accuracy.

5.3 Investigation of the tag-to-body separation

An embroidered dipole tag is designed utilising the human arm model for case 1 and the embroidered tag model on t = 0.25 mm thick cotton fabric (ε_r = 1.8 and tan δ = 0.018) substrate using conductive sewing thread [56] and NXP IC. Tag antenna conductor effective conductivity and thickness of 4000 S/m and 0.2 mm, respectively, are used in the simulations. These are the same values as used for the embroidered tag 2 (E2). Therefore, the tag is manufactured using the same stitch pattern and density as for E2. The manufacturing is conducted according to the sewing process demonstrated in [45]. On-body measurements are conducted in anechoic EMC chamber using the Tagformance measurement system similarly as for the embroidered tags in the previous Section.

The embroidered tag is optimised on the human arm by increasing the tag antenna input inductance required for the impedance conjugate matching at around 900 MHz. The fabricated and measured tag on body is shown in Fig. 5.10.

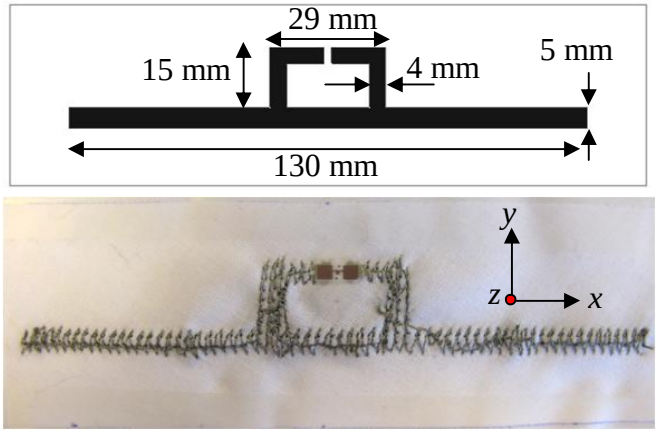

Fig. 5.10. Designed and optimised embroidered tag. The NXP IC is attached over the 2-mm wide gap with conductive epoxy.

The simulated tag antenna input impedance for different substrate thicknesses t is provided in Fig. 5.11. Even though the required amount of inductance is achieved within the global UHF RFID band, the tag antenna input resistance is far larger than the IC input resistance. This is probably because the sewing thread losses are inherently relatively large, which contributes to a large input loss resistance R_{ohmic}.

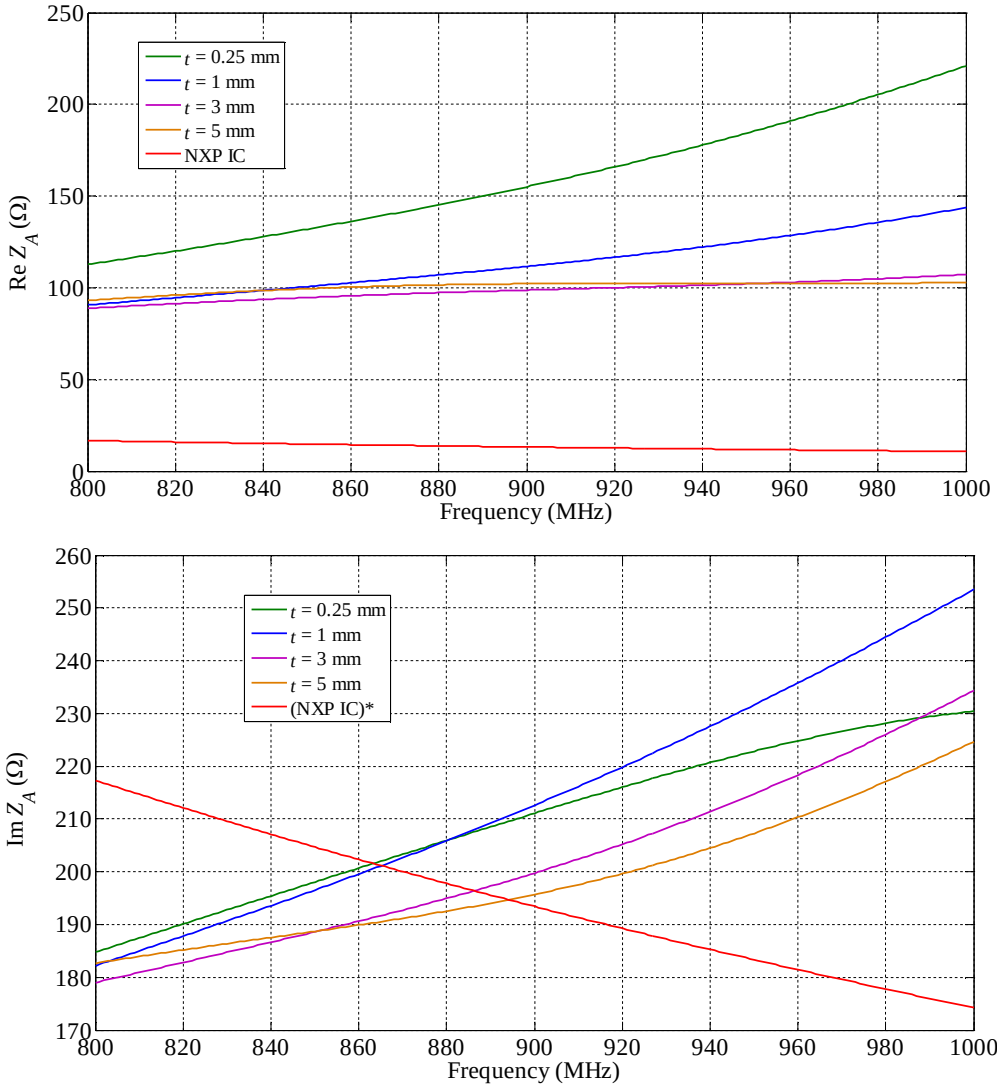

Fig. 5.11. Simulated embroidered tag antenna input impedance for different substrate thicknesses *t*. The tag antenna input resistance shows considerably higher value than the chip input resistance.

The optimised tag in Fig. 5.10 is also simulated and measured in free-space with no additional cotton fabric layers to assure that the embroidered tag model is valid. The free-space measurements are conducted in the Tagformance test cabinet. After calibration and threshold measurement the tag maximum forward link read range is obtained from Eq. (4.5). The free-space results are given in Fig. 5.12. The tag model predicts the tag performance good. The tag model shows an accuracy of ±1 m over the whole measured band. The tag model is hereby valid.

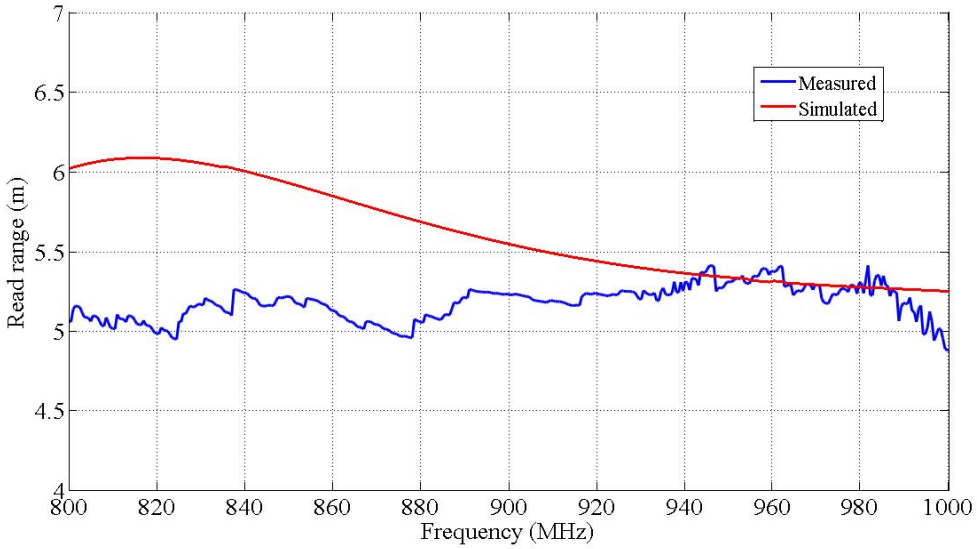

Fig. 5.12. Simulated and measured free-space forward link read range in the +*z* direction for the on-body optimised embroidered tag. The embroidered tag model is valid.

After optimisation, the effect of tag-to-body separation is investigated by adding 0.25-mm thick cotton fabric layers between the tag and the body. In simulations this means increasing the tag substrate thickness by 0.25 mm for each added cotton layer. In practise, separate cotton fabric layers are added beneath the embroidered tag for the on-body measurements. Possible air layers between cotton fabric layers are neglected in the simulation model. Fig. 5.13 shows the tag position on arm and the simulation model.

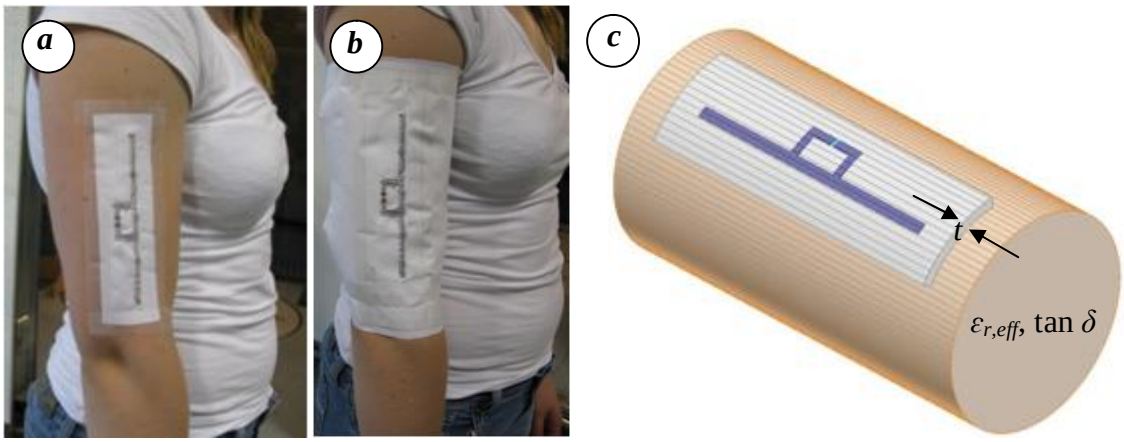

Fig. 5.13. On-body measurements and simulations: **(a)** tag position on arm with no additional cotton fabric layers, **(b)** tag-to-body separation successively increased with additional 3, 11 and 19 cotton fabric layers, **(c)** embroidered tag model with varying cotton fabric thickness *t* on the human arm model with the electrical effective parameters $\varepsilon_{r,eff}$ = 6 and tan δ = 0.50.

The simulated and measured average read ranges on body are presented in Fig. 5.14. Within the 860–960 MHz band, the simulation model is able to predict the performance with ±0.5 m accuracy. As expected, the read range increases with increased tag-to-body separation. A 5-mm separation is required to achieve at least 3 m read range. Interestingly, as the separation exceeds *t* = 1 mm, the measured responses become more

wavy. The reason is that when the tag is close (t < 1 mm) to the body, the introduced losses from the body are more prominent compared to the case where additional fabric layers are used. As a consequence, the performance is more broad-banded when the tag-to-body isolation is small. Obviously, the simulation model is not able to predict this phenomenon.

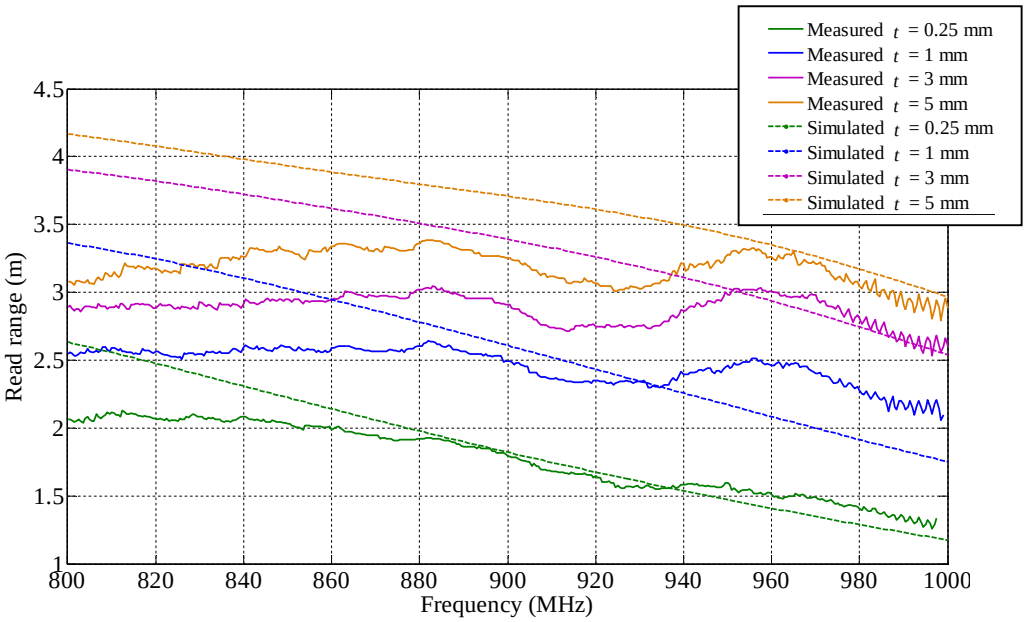

Fig. 5.14. Simulated and measured forward link read range in the +z direction for the on-body optimised embroidered tag with different tag-to-body separation t. The prediction of the simulation model is good. The read range is rapidly increased with a small separation distance.

The results demonstrate that single-layered embroidered tags achieve at least 1.5 m bore-sight read range on the human arm, which is enough for most wearable tag applications. Most common garment fabrics have a thickness of around 1 mm. Thus, embroidered tags integrated onto garments are able to provide 2.5-m read ranges. The simple simulation model can be used as a powerful tool for wearable antenna design and optimisation.

6 CONCLUSIONS

In this project a human arm model is developed for the UHF frequencies. The model provides an important step in the design and optimisation of wearable tags. A simple and homogeneous cylinder is able to predict the tag performance well when the tag is attached to the human arm. Two different cases are considered; in case 1 the tag substrate is attached to the arm, whereas in case 2 the tag IC is facing the arm. A simulation model for case 1 having the electrical parameters $\varepsilon_{r,eff}$ and tan δ values of 6 and 0.50, respectively, is able to predict the wearable tag realised gain with ±3 dB accuracy over the frequency band 800–1000 MHz. A simulation model for case 2 having the electrical parameters $\varepsilon_{r,eff}$ and tan δ values of 19 and 0.35, respectively, is able to predict the wearable tag realised gain with ±10 dB accuracy over the frequency band. Obviously, the simulation model for case 2 requires further development. Herewith the case1 simulation model should be chosen for future use.

The human arm model does not rely on any information about the electrical properties of a particular tissue type. Instead, the model is based on true measured tag response from a reference tag attached directly to the human arm. The measured response serves as a reference response. The electrical parameters of the human arm model are adjusted so that the simulated tag response from the human arm model agrees with that of the reference response. The least squares method provides an efficient tool for determining the quality of agreement. Even though this project concentrates on the human arm, the same procedure can be used to develop UHF models representing other human body parts or other application environments.

The human arm models have some unavoidable drawbacks that should be considered. Since the model is derived based on a reference response from a tag attached to the arm, this response will in addition to the tag response include all the unidealities associated with the practical on-body measurements. The uncertainties and errors caused by the measurement unidealities are to great extent random errors. For example, the human arm model is derived for a certain unknown air layer between the to-skin attached reference tag and the skin. Any other tag attached to the arm will certainly hold different amount of air and will not be attached exactly to the same arm location. Obviously, the elimination of the random errors is challenging, unless impossible. These errors are particularly prominent in measurement scenarios where the tag IC is against the skin and the tag-to-body interaction is reinforced. As a consequence, the human arm model for such scenarios suffers from significantly poorer accuracy than the human arm model for measurement scenarios where the tag substrate is against the skin and provides tag-to-body isolation.

Even though the simple human arm simulation model for case 1 has some accuracy limitations, it can still be used as a powerful tool for wearable antenna design and optimisation. Future work include wearable tag antenna design and optimisation with help of the developed human arm model. Tag design and analysis is extended to include other types of wearable tag antennas, for example patch- and slot-type antennas. Of course, for each design the specifications for wearable antennas should be met. Much of the future research will concentrate on new techniques to decouple the tag antenna from the dissipative and dielectric human body. Conductive sewing thread and conductive fabrics together with new low-loss and high-permittivity materials, EBG and Substrate Integrated Waveguide (SIW) structures are all possible candidates for the design and development of new miniaturised wearable tag antennas that operate reliably and efficiently in the vicinity of the challenging human body. New antenna structures and materials require proper modelling before they can efficiently be used in antenna design. However, once the materials are determined, the near future will bring new and powerful solutions for wearable tag antennas.

REFERENCES

[1] D. M. Pozar, “Microwave Engineering,” 3rd ed. John Wiley & Sons Inc., United States of America, 2005.

[2] R. Sorrentino, and G. Bianchi, “Microwave and RF Engineering.” John Wiley & Sons, Ltd., United States of America, 2010.

[3] D. K. Cheng, “Field and Wave Electromagnetics,” 2nd ed. Addison-Wesley Publishing Company, Inc., United States of America, 1992.

[4] C. A. Balanis, “Antenna Theory, Analysis and Design,” 3rd ed. John Wiley & Sons Inc., United States of America, 2005.

[5] W. L. Stutzman, and G. A. Thiele, “Antenna Theory and Design,” 2nd ed. John Wiley & Sons Inc., United States of America, 1998.

[6] A. Lehto, A. Räisänen, “Radiotekniikan Perusteet,” 12th ed. Hakapaino Oy, Finland, 2007.

[7] D. M. Dobkin, “The RF in RFID – Passive UHF RFID in Practise.” Elsevier Inc., United States of America, 2008.

[8] K. Kurokawa, “Power Waves and the Scattering Matrix,” *IEEE Transactions on Microwave Theory Techniques*, vol. MTT-13, no. 3, pp. 194–202, March 1965.

[9] H. Stockman, “Communication by Means of Reflected Power,” *Proceedings of the Institute of Radio Engineers*, vol. 36, no. 10, pp. 1196–1204, October 1948.

[10] P. V. Nikitin, and K. V. S. Rao, “Theory and Measurement of Backscattering from RFID Tags,” *IEEE Antennas and Propagation Magazine*, vol. 48, no. 6, pp. 212–218, December 2006.

[11] EPC™ Radio-Frequency Identity Protocols, Class-1 Generation-2 UHF RFID, Version 1.1.0 (2005). http://www.gs1.org/gsmp/kc/epcglobal/uhfc1g2/uhfc1g2_1_1_0-standard-20071017.pdf. Accessed 20 May 2012.

[12] T. Bauernfeind, K. Preis, G. Koczka, S. Maier, and O. Biro, “Influence of the Non-Linear UHF-RFID IC Impedance on the Backscatter Abilities of a T-Match Tag Antenna Design,” *IEEE Transactions on Magnetics*, vol. 48, no. 2, pp. 755–758, February 2012.

[13] Tang Z, He Y, Hou Z, and Li B, “The Effects of Antenna Properties on Read Range Distance in Passive Backscatter RFID Systems,” International Conference on Networks Security, Wireless Communications and Trusted Computing, China, vol. 1, pp. 120–123, 25–26 April 2009, Wuhan, Hubei, China.

[14] G. Marrocco, “The Art of UHF RFID Antenna Design: Impedance-Matching and Size-Reduction Techniques,” *IEEE Antennas and Propagation Magazine*, vol. 50, no. 1, pp. 66–79, February 2008.

[15] P. S. Hall, and Y. Hao Y, "Antennas and Propagation for Body Centric Communications," Proceedings of the 1st European Conference on Antennas and Propagation, pp. 1–7, 6–10 November 2006, Nice, France.

[16] S. Manzari, C. Occhiuzzi, and G. Marrocco, "Experimental Characterization of Bodycentric Passive RFID Systems," IEEE International Symposium on Antennas and Propagation, pp. 1000–1003, 3–8 July 2011, Spokane, Washington, USA.

[17] C. Occhiuzzi, and G. Marrocco, "Experimental Characterization of the RFID STENtag for Passive Vascular Monitoring," Proceedings of the 6th European Conference on Antennas and Propagation, pp. 3669–3671, 26–30 March 2012, Prague, Czech Republic.

[18] J. Kim, and Y. Rahmat-Samii, "Implanted Antennas Inside a Human Body: Simulations, Designs, and Characterizations," *IEEE Transactions on Microwave Theory and Techniques*, vol. 52, no. 8, pp. 1934–1943, August 2004.

[19] H. Rajagopalan, and Y. Rahmat-Samii, "Novel Ingestible Capsule Antenna Designs for Medical Monitoring and Diagnostics," Proceedings of the 4th European Conference on Antennas and Propagation, pp. 1–5, 12–16 April 2010, Barcelona, Spain.

[20] C. Occhiuzzi, S. Cippitelli, and G. Marrocco, "Modeling, Design and Experimental of Wearable RFID Sensor Tag," *IEEE Transactions on Antennas and Propagation*, vol. 58, no. 8, pp. 2490–2498, August 2010.

[21] G. Marrocco, "RFID Antennas for the UHF Remote Monitoring of Human Subjects," *IEEE Transactions on Antennas and Propagation*, vol. 55, no. 6, pp. 1862–1870, June 2007.

[22] C. Occhiuzzi, and G. Marrocco, "RFID Detection of Human Body Movements," European Microwave Conference, pp. 017–020, 29 September–1 October 2009, Rome, Italy.

[23] T. Kellomäki, and L. Ukkonen, "Design Approaches for Bodyworn RFID Tags," 3rd International Symposium on Applied Science in Biomedical Communication, pp. 1–5, 7–10 November 2012, Rome, Italy.

[24] L. Zhang, Z. Wang, D. Psychoudakis, and J. L. Volakis, "E-fiber Electronics for Body-Worn Devices," Proceedings of the 6th European Conference on Antennas and Propagation, pp. 760–761, 26–30 March 2012, Prague, Czech Republic.

[25] D. Psychoudakis, G. Y. Lee, C. C. Chen, and J. L. Volakis, "Military UHF Body-Worn Antennas for Armored Vests," Proceedings of the 4th European Conference on Antennas and Propagation, pp. 1–4, 12–16 April 2010, Barcelona, Spain.

[26] C. Hertleer, H. Rogier, L. Vallozzi, and L. Van Langenhove, "A Textile Antenna for Off-Body Communication Integrated Into Protective Clothing for Firefighters," *IEEE Transactions on Antennas and Propagation*, vol. 57, no. 4, part 1, pp. 919–925, April 2009.

[27] Dielectric Properties of Body Tissues (2012). http://niremf.ifac.cnr.it/tissprop/htmlclie/htmlclie.htm. Accessed 29 August 2012.

[28] T. Kellomäki, T. Björninen, L. Ukkonen, and L. Sydänheimo, “Shirt Collar tag for Wearable UHF RFID Systems,” Proceedings of the 4th European Conference on Antennas and Propagation, pp. 1–5, 12–16 April 2010, Barcelona, Spain.

[29] T. Kellomäki, J. Heikkinen, and M. Kivikoski, “One-Layer GPS Antennas Perform Well near a Human Body,” Proceedings of the 2nd European Conference on Antennas and Propagation, pp. 1–6, 11–16 November 2007, Edinburgh, UK.

[30] L. Ukkonen, L. Sydänheimo, M. Kivikoski, “Effects of Metallic Plate Size on the Performance of Microstrip Patch-Type Tag Antennas for Passive RFID,” *IEEE Antennas and Wireless Propagation Letters*, vol. 4, pp. 410–413, December 2005.

[31] H. Rajagopalan, and Y. Rahmat-Samii, “Conformal RFID Antenna Design Suitable for Human Monitoring and Metallic Platforms,” Proceedings of the 4th Conference on Antennas and Propagation, pp. 1–5, 12–16 April 2010, Barcelona, Spain.

[32] M. Svanda, and M. Polivka, “Dualband Wearable UHF RFID Antenna,” Proceedings of the 2nd European Conference on Antennas and Propagation, pp. 1–5, 11–16 November 2007, Edinburgh, UK.

[33] M. Takahashi, T. Nakajima, K. Saito, and K. Ito, “Characteristics of Wristband Type RFID Antenna,” Proceedings of the 4th Conference on Antennas and Propagation, pp. 1–4, 12–16 April 2010, Barcelona, Spain.

[34] J. Vicente, and A. A. Moreira, “Electro-Textile Printed Slot Antennas over Finite EBG Structure,” International Workshop on Antenna Technology, pp. 1–4, 1–3 March 2010, Lisbon, Portugal.

[35] G. Kim, J. Lee, K. H. Lee, Y. C. Chung, J. Yeo, B. H. Moon, J. Yang, and H. C. Kim, “Design of a UHF RFID Fiber Tag Antenna with Electric-thread using a Sewing Machine,” Asia-Pacific Microwave Conference, pp. 1–4, 16–20 December 2008, Macau, Japan.

[36] J. S. Roh, Y. S. Chi, J. H. Lee, Y. Tak, S. Nam, and T. J. Kang, “Embroidered Wearable Multiresonant Folded Dipole Antenna for FM Reception,” *IEEE Antennas and Wireless Propagation Letter*, vol. 9, pp. 803–806, August 2010.

[37] J. H. Choi, Y. Kim, K. Lee, and Y. C. Chung, “Various Wearable Embroidery RFID Tag Antenna Using Electro-Thread,” IEEE International Symposium on Antennas and Propagation Society, pp. 1–4, 5–11 July 2008, San Diego, California, USA.

[38] Y. Kim, K. Lee, Y. Kim, and Y. C. Chung, “Wearable UHF RFID Tag Antenna Using Flexible Electro-Thread and Textile,” IEEE International Symposium on Antennas and Propagation Society, pp. 5487–5490, 9–15 June 2007, Honolulu, Hawaii, USA.

[39] S. Manzari, C. Occiuzzi, and G. Marrocco, “Reading Range of Wearable Textile RFID Tags in Real Configurations,” Proceedings of the 5th European Conference on Antennas and Propagation, pp. 433–436, 11–15 April 2011, Rome, Italy.

[40] M. H. Lin, and C. W. Chiu, “Human-body Effects on the Design of Card-type UHF RFID Tag Antennas,” IEEE International Symposium on Antennas and Propagation Society, pp. 521–524, 3–8 July 2011, Spokane, Washington, USA.

[41] J. L. Volakis, Z. Lanlin, W. Zheyu, and Y. Bayram, “Embroidered Flexible RF Electronics,” IEEE International Workshop on Antenna Technology, pp. 8–11, 5–7 March 2012, Tucson, Arizona, USA.

[42] Y. Bayram, Z. Yijun, S. S. Bong, X. Shimei, Z. Jian, N. A. Kotov, and J. L. Volakis, “E-Textile Conductors and Polymer Composites for Conformal Lightweight Antennas,” *IEEE Transactions on Antennas and Propagation*, vol. 58, no. 8, pp. 2732–2736, August 2010.

[43] Y. Ouyang, and W. J. Chappell, “High Frequency Properties of Electro-Textiles for Wearable Antenna Applications,” *IEEE Transactions on Antennas and Propagation*, vol. 56, no. 2, pp. 381–389, February 2008.

[44] E. Moradi, T. Björninen, L. Ukkonen, and Y. Rahmat-Samii, “Characterization of Embroidered Dipole-Type RFID Tag Antennas,” IEEE International Conference on RFID-Technology and Applications, 6 p., 5–8 November 2012, Nice, France.

[45] E. Koski, K. Koski, T. Björninen, A. A. Babar, L. Sydänheimo, and L. Ukkonen, “Fabrication of Embroidered UHF RFID Tags,” IEEE International Symposium on Antennas and Propagation, 2 p., 8–14 July 2012, Chicago, Illinois, USA.

[46] K. Koski, E. Koski, T. Björninen, A. A. Babar, L. Ukkonen , and L. Sydänheimo, “Practical Read Range Evaluation of Wearable Embroidered UHF RFID Tag,” IEEE International Symposium on Antennas and Propagation, 2 p., 8–14 July 2012, Chicago, Illinois, USA.

[47] T. Björninen, L. Sydänheimo, and L. Ukkonen, “Development and Validation of an Equivalent Circuit Model for UHF RFID IC Based on Wireless Tag Measurements,” Proceedings of the Antenna Measurements Techniques Association Symposium, 6 p., 21–26 October 2012, Bellevue, Washington, USA.

[48] L. Ukkonen, L. Sydänheimo, and Y. Rahmat-Samii, “Sewed Textile RFID Tag and Sensor Antennas for On-Body Use,” Proceedings of the 6th European Conference on Antennas and Propagation, pp. 3450–3454, 26–30 March 2012, Prague, Czech Republic.

[49] Tagformance Lite Measurement System, User Guide, Rev 3.8.x (2011). http://voyantic.com/Tagformance%20Manual.pdf. Accessed 20 May 2012.

[50] C. Capps, EDN Network: Near field or far field (2001). http://www.edn.com/design/communications-networking/4340588/Near-field-or-far-field-. Accessed 30 August 2012.

[51] Voyantic, RFID Measurement Cabinet (2012). http://www.voyantic.com/index.php?trg=browse&id=140. Accessed 19 May 2012.

[52] Huber+Suhner Antenna, Product 1399.17.0028 Overview (2011). http://www.hubersuhner.com/. Accessed 19 May 2012.

[53] Huber+Suhner Antenna, Product 1309.17.0003 Overview (2010). http://www.hubersuhner.com/. Accessed 30 May 2012

[54] S. J. Miller, The Method of Least Squares. http://web.williams.edu/go/math/sjmiller/public_html/BrownClasses/54/handouts/MethodLeastSquares.pdf. Accessed 30 August 2012.

[55] H. Abdi, Least Squares (2003). http://www.utdallas.edu/~herve/Abdi-LeastSquares-pretty.pdf. Accessed 30 August 2012.

[56] Shieldex, USA, Yarns and fillers (2012). http://www.shieldextrading.net/yarn_and_filler.html. Accessed 30 August 2012.

[57] S. Sankaralingam, and B. Gupta, "Determination of Dielectric Constant of Fabric Materials and their Use as Substrates for Design and Development of Antennas for Wearable Applications," *IEEE Transactions on Instrumentation and Measurement*, vol. 59, no. 12, pp. 3122–3130, December 2010.